DETECTING AND MONITORING THE FORMATION OF BIOLOGICAL NANOASSEMBLIES WITH RESISTIVE-PULSE SENSING

by

Jeffrey Daniel Uram

A dissertation submitted in partial fulfillment
of the requirements for the degree of
Doctor of Philosophy
(Biomedical Engineering)
in The University of Michigan
2007

Doctoral Committee:

Assistant Professor Michael Mayer, Chair
Professor Kensall D. Wise
Associate Professor Alan J. Hunt
Associate Professor Nicholas Kotov

DEDICATION

To my parents and siblings for listening

To the friends I met along the way for many reasons

ACKNOWLEDGEMENTS

The research described in this dissertation was funded by IMRA America, AISIN USA, a National Science Foundation CAREER award granted to Michael Mayer (grant No. 0449088), and seed funds from the College of Engineering, University of Michigan.

Special thanks are extended to:

My research advisor Michael Mayer who gave me the opportunity to perform these studies and provided support in many forms along the way. He always made time to talk with me about the research, and he put up with my tendency towards vigorous discussions. The knowledge that I have learned while being in his laboratory will be priceless in the coming years.

The other members of my doctoral committee, which was the same as my qualifying exam committee. Professor Hunt and his research group provided many of the pore structures that I used for my research, and he provided excellent feedback on the manuscripts published in *Angewandte Chemie International Edition* and *Small*. Professor Kotov allowed me to use the instruments in his laboratory, and the class I took with him on nanotechnology as well as his research provides motivation for my work. Professor Wise taught two classes that I took while here at U of M; both were very enjoyable and I learned many new things. His stories on the early days of the semiconductor industry were particularly interesting and greatly appreciated.

My friend and colleague Daniel J. Estes for providing assistance in all of my scientific endeavors as well as many entertaining evenings. I am uncertain I would have completed this thesis without his help and friendship.

Sheereen Majd, Dr. Ricardo F. Capone, and all of the other current and former members of the Biomembrane Laboratory. They listened to talks on my research and me talking in general, and they always provided valuable feedback. They also provided numerous opportunities for me to learn new things through scientific discussions.

Kevin Ke for fabricating many of the pores that I used for my research as well as scientific discussions.

Professor Matthew O'Donnell, former Chair of the Department of Biomedical Engineering, for support in my endeavor to obtain a PhD, willingness to negotiate, and advice.

Professor Daryl Kipke for the opportunity to work in the Neural Engineering Laboratory.

Kip A. Ludwig, Dr. Matthew D. Johnson, Nick Langhals, Dr. Mohammad R. Abidian, Dr. Elizabeth A. Nunamaker, and the other current and former members of the Neural Engineering Laboratory for their help and scientific discussions.

Dr. John F. Mansfield, Dr. Haiping Sun, Dr. Kai Sun, and the other staff members of the Electron Microbeam Analysis Laboratory for assistance with and training on the scanning electron microscopes that I used for my research.

Aaron Glatzer, Katharine T. Beach, and the other staff members of the Michigan Nanofabrication Facility for providing help and training on the equipment I needed to use for my research.

Dotty Sorenson and the other staff members of the Cell and Developmental Biology Microscopy and Image Analysis Laboratory for assistance with and training on the transmission electron microscope that I used for my research.

Tonya Y. Brown, Maria E. Steele, and the other staff members of the department of biomedical engineering for their assistance with paperwork and purchasing.

My parents and siblings for many reasons, but most importantly, they were always willing to listen. Thanks again for the food mom.

TABLE OF CONTENTS

LIST OF TABLES

Table **Page**

LIST OF FIGURES

ABSTRACT

DETECTING AND MONITORING THE FORMATION OF BIOLOGICAL NANOASSEMBLIES WITH RESISTIVE-PULSE SENSING

by

Jeffrey Daniel Uram

Chair: Michael Mayer

This thesis describes innovative applications for resistive-pulse sensing with submicrometer pores and discusses the noise and bandwidth characteristics of the experimental setup.

In the initial study, resistive-pulse sensing was used to monitor the formation of antibody-antigen complexes (immune complexes or biological nanoassemblies). The developed technique was rapid (detection in ≤ 15 minutes), label-free, could be performed in small volumes (≤ 40 μL), and required no immobilization of the antibody or antigen. This assay was able to detect purified antigens at concentrations as low as 30 nM, and to detect antigens in complex media such as serum. It also enabled the characterization of the time course of immune complex formation and growth with a precision that made it possible to detect single complexes.

In the second study, resistive-pulse sensing was used to characterize and quantify antibody-virus interactions. These experiments demonstrated that resistive-pulse sensing can be used to detect a specific virus or a virus-specific antibody in solution, probe the ability of an antibody to immunoprecipitate the virus, determine the average number of antibodies bound to virus particles, and monitor the time course of the assembly of antibodies onto viruses *in situ*.

The third study developed theory for extracting thermodynamic parameters of antibody-antigen interactions from resistive-pulse data. A model system presented in the literature, antibodies binding to spherical nanoparticles that expose antigens, was used to validate the theory; the calculated solid phase affinity constant of the antibody ($2.6 \cdot 10^8 \pm 0.8 \cdot 10^8$ M^{-1}) was in agreement with the specifications of the supplier of the antibody.

The fourth and final study examined in detail the theoretical and experimental noise and bandwidth of current recordings from resistive-pulse sensing experiments. The theory presented in this study combined with its experimental validation enables the development of resistive-pulse sensing systems optimized for low-noise (high sensitivity) and high-bandwidth (high accuracy).

The experiments presented here demonstrate that resistive-pulse sensing is a simple, yet powerful technique for examining the formation of biological nanoassemblies. Based on these findings, resistive-pulse sensing holds great promise as a tool for nanotechnology and for use in portable or high-throughput assays.

Table X.1. Publications and patent that resulted from the work presented in this thesis:

Source	Type	Description
Chapter 2	Publication	J. D. Uram, K. Ke, A. J. Hunt, and M. Mayer. "Label-free affinity assays by rapid detection of immune complexes in submicrometer pores." *Angew. Chem. Int. Ed.* 2006. 45:2281-2285.
Chapter 3	Publication	J. D. Uram, K. Ke, A. J. Hunt, and M. Mayer. "Submicrometer pore-based characterization and quantification of antibody-virus interactions." *Small.* 2006. 2:967-972.
Chapter 4	Publication	J. D. Uram and M. Mayer. "Estimation of solid phase affinity constants using resistive-pulses from functionalized nanoparticles." *Biosens. Bioelectron.* 2007. 22:1556-1560.
Chapters 2, 3, and 4	Patent Application	M. Mayer, J. D. Uram, K. Ke, and A. J. Hunt "Use of resistive-pulse sensing with submicrometer pores or nanopores for the detection of the assembly of submicrometer or nanometer sized objects" U.S. Application Number: 11671171
Chapter 5	Publication	J. D. Uram, K. Ke, and M. Mayer. "Noise and bandwidth of current recordings from submicrometer pores and nanopores." *Small.* 2007. Submitted

Table X.2. Presentations and posters that resulted from the work presented in this thesis:

Source	Type	Description
Chapter 2	Poster	J. D. Uram, K. Ke, A. J. Hunt, and M. Mayer. "Rapid, label-free detection of immune complexes using nanopores" Biomedical Engineering Society Annual Meeting, Baltimore, MD, Sept. 28 – Oct. 1, 2005
Chapter 2	Oral Pres.	J. D. Uram, K. Ke, A. J. Hunt, and M. Mayer. "Label-free affinity assays by rapid detection of immune complexes using nanopores" Pacifichem, Honolulu, HI, Dec. 15 – 20, 2005

Chapters 2 and 3	Poster	J. D. Uram, K. Ke, A. J. Hunt, and M. Mayer. “Nanopore-based detection of immune complexes and viruses” Biophysical Society Annual Meeting, Salt Lake City, UT, Feb. 18 – 22, 2006
Chapters 2, 3, and 4	Invited Oral Pres.	M. Mayer and J. D. Uram. “Nanopore-based assays of biospecific assemblies” Third Focused Workshop on Electronic Recognition of Bio-Molecules, Liège, Belgium, Sept. 6 – 8, 2006
Chapters 2, 3, and 4	Poster	J. D. Uram, K. Ke, A. J. Hunt, and M. Mayer. “Nanopore-based detection of antibody-antigen interactions” Biomedical Engineering Society Annual Meeting, Chicago, IL, Oct. 11 – 14, 2006
Chapter 5	Poster	J. D. Uram and M. Mayer “Theoretical and experimental examination of the noise and bandwidth of current recordings from sub-micrometer pores and nanopores” Biophysical Society Annual Meeting, Baltimore, MD, March 3 – 7, 2007
Chapters 2, 3, and 4	Oral Pres.	J. D. Uram and M. Mayer “Nanopore-based detection of immune complexes and viruses” Annual Meeting of the Institute of Biological Engineering, MO, March 30 – April 1, 2007
Chapters 2, 3, and 4	Oral Pres.	J. D. Uram, K. Ke, A. J. Hunt, and M. Mayer. “Nanopore-based detection of immune complexes and viruses” Materials Research Society Spring Meeting, San Francisco, CA, April 9 – 13, 2007
Chapters 2, 3, and 4	Oral Pres.	J. D. Uram, K. Ke, A. J. Hunt, and M. Mayer. “Nanopore-based detection of immune complexes and viruses” American Chemical Society National Meeting, Boston, MA, August 19 – 23, 2007
Chapters 2, 3, and 4	Oral Pres.	J. D. Uram, K. Ke, A. J. Hunt, and M. Mayer. “Nanopore-based detection of antibody-antigen and antibody-virus interactions” Biomedical Engineering Society Annual Meeting, Los Angeles, CA, Sept. 27 – 29, 2007
Chapter 5	Poster	J. D. Uram and M. Mayer. “Noise and bandwidth of current recordings from submicrometer pores and nanopores” Biomedical Engineering Society Annual Meeting, Los Angeles, CA, Sept. 27 – 29, 2007

CHAPTER 1

INTRODUCTION

The solution-based assembly of nanometer-sized objects into larger structures is a common and fundamental process in all living cells and organisms. The size of the assembled structure can range from a few nanometers to microns or more; examples of these structures include proteins, nucleic acids (DNA, RNA, etc…), viruses and antibody-antigen complexes (Figure 1.1). Science has recently begun catching up with biology and the blossoming field of nanotechnology is shifting its focus from making nanometer-sized objects to assembling them into useful devices (Figure 1.1) (1-13). Monitoring in detail and in real time the solution-based assembly process and the resulting biological or synthetic structures is critical for gaining a complete understanding of the construction process as well as the driving forces behind the assembly.

Currently, most of the techniques used for monitoring the solution-based assembly process of nanometer-sized objects are based on measuring the interaction of the assembly with electromagnetic radiation (techniques such as transmission electron microscopy and scanning electron microscopy are also commonly used to study nanoassemblies; however, these techniques require that the sample be dried out and placed in high vacuum which may modify properties of the sample compared to its

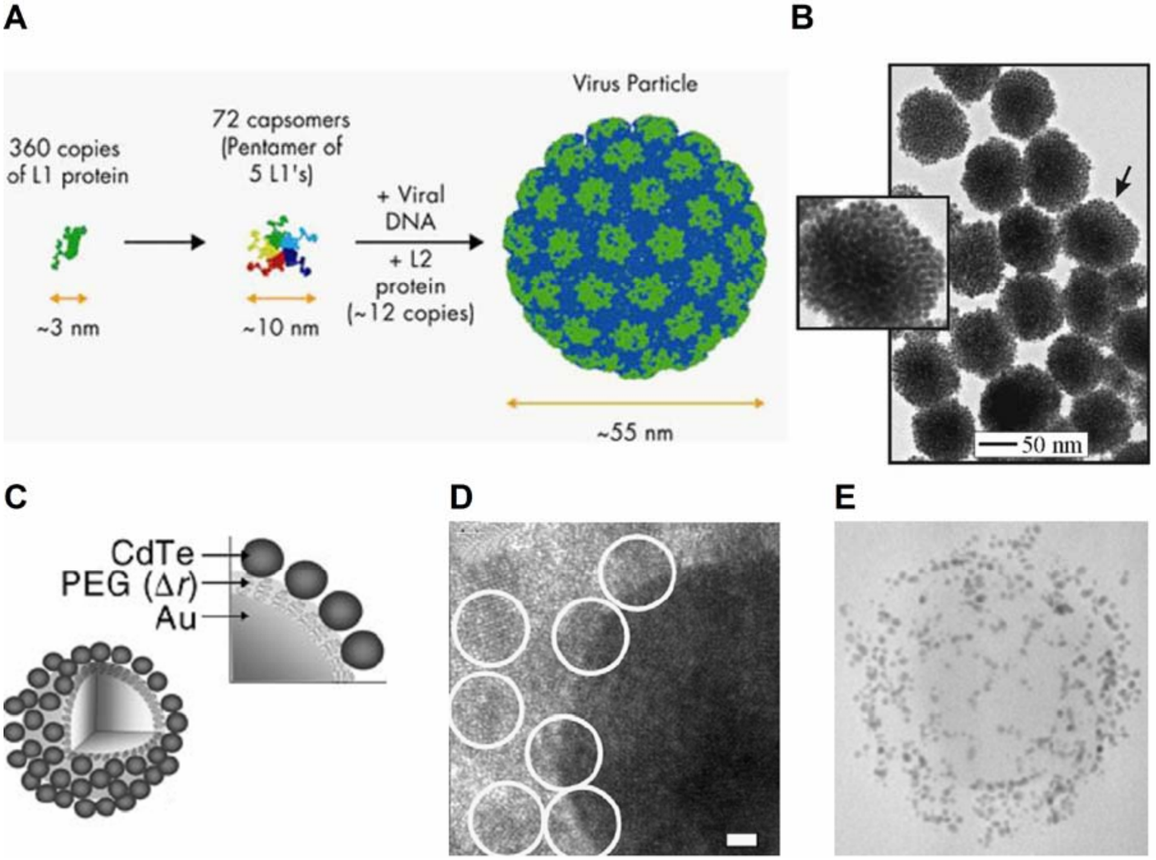

Figure 1.1. Examples of various nanoassemblies. A) Cartoon illustrating the formation of a human papillomavirus (HPV) capsid from its component proteins (adapted from Merck & Co, Inc. (19)). B) Transmission electron microscope (TEM) image of a nanoassembly created from gold nanoparticles with diameters of ~5.5 nm (adapted from Maye *et al.* (13)) C) Cartoon of a synthetic nanoassembly which consists of 3.7 nm CdTe nanoparticles bound to a 20 nm Au core nanoparticle via a poly(ethyleneglycol) (PEG) linker. This device can operate as a nanoscale thermometer since the length of the PEG linker is dependent on temperature and the optical properties of the nanoassembly are influenced by the distance between the CdTe nanoparticles and the core AU particle (adapted from Lee *et al.* (1)). D) TEM image of the assembly from panel C. The scale bar is 5 nm (adapted from Lee *et al.* (1)). E) TEM image of a Chilo iridescent virus (CIV), diameter ~140 nm, coated in gold nanoparticles. These gold nanoparticles can be used as nucleation sites for further deposition of gold creating a metallodielectric nanoshell from the biological template; such nanoshells have applications in surface-enhanced Raman spectroscopy and cancer treatment (adapted from Radloff *et al.* (12))

solution-based state). Techniques such as optical spectroscopy (UV, Vis, and IR) (1-3,5,7,11), static and dynamic light scattering (SLS and DLS) (4,12-16), and turbidmetry (14,17,18), are widely used and have produced excellent results; however, these techniques have some limitations. Due to the nature of the measurement, which involves passing a beam of light through the solution-based sample, the data obtained from these techniques is a global measure of the system. That is, these optical techniques do not probe individual assemblies and therefore have difficulties providing an accurate characterization of the polydisperse structures that may form from the assembly of the nanometer-sized objects. The ideal measurement technique would be able to examine each assembly individually yet maintain a high throughput so that characterizing many assemblies (as would be required for obtaining a true measure of the system) would be rapid and accurate.

In this thesis, a new method for detecting and quantitatively monitoring the solution-based formation of biological nanoassemblies (which may be extendable to other nanoassemblies) is developed based on the well-established technique of resistive-pulse sensing; this method is able to examine individual assemblies and can examine hundreds of assemblies within minutes. The development of this technique is divided into four research chapters, each of which is closely based on a published, peer-reviewed journal article or article that is currently in review (Chapters 2, 3, and 4 are published, Chapter 5 is being reviewed, see Table X.1). The first three research chapters are devoted to examining the capabilities of resistive-pulse sensing for detecting and characterizing biological nanoassemblies; the last research chapter is devoted to examining in detail the noise and bandwidth of the experimental system so that these two parameters may be predicted (which enables simulations of resistive-pulse sensing experiments) and optimized (which increases sensitivity and enables data with a high information content). Before presenting this research, we will examine the history of resistive-pulse sensing as well as other applications for this simple, yet powerful technique.

1.1. Invention of Resistive-Pulse Sensing

Resistive-pulse sensing, which is also known as Coulter counting, was developed by Wallace H. Coulter in the 1950s for use in an automated blood cell counter (20). His invention revolutionized the process of counting cells by reducing the assay time by a factor of 120 and the error by almost a factor of 10 (21). Yet the concept is amazingly simple. Two liquid compartments containing an electrolyte are separated by a small pore, and a constant voltage (typically 0.01 – 4.00 V) is applied between the liquid compartments as shown in Fig. 1.2A. The pore constitutes the largest electrical resistance in the system and determines the magnitude of the current flow. When a particle (living cell, nanoassembly, etc…) passes through the pore, it displaces a volume of conducting electrolyte, increasing the resistance of the pore (20,22-25). This transient increase in resistance (resistive-pulse) can be observed as a drop in current with a peak amplitude related to the volume of the particle, the diameter and length of the pore, and the applied voltage (Fig. 1.2B) (20,22-25).

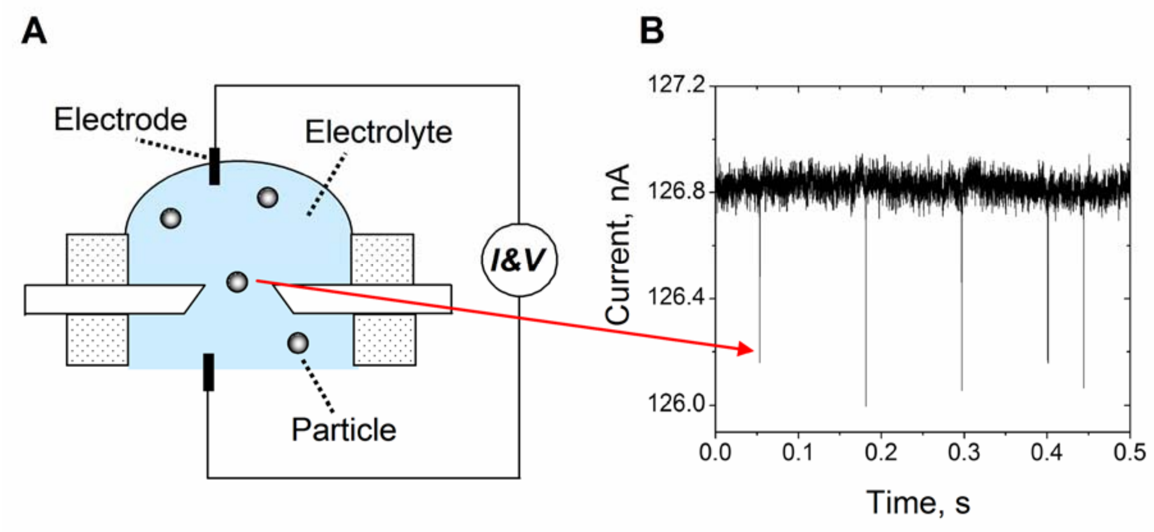

Figure 1.2. Illustration of the principle of Coulter counting. A) A small pore separates two liquid compartments that contain an electrolyte. A constant potential is applied between the liquid compartments, and the current flowing through the pore is monitored. When a particle passes through the pore, it displaces a volume of electrolyte, which transiently increases the resistance of the pore. The transient increase in resistance causes a transient decrease in the current flowing through the pore. B) Current recording showing the transient decrease in current (resistive-pulse) that results from a 60 nm particle passing through a pore with a diameter of 190 nm under an applied potential of 0.2 V.

1.2. Resistive-Pulse Sensing Work Until 1996

The sensitivity of a resistive-pulse sensor (*i.e.* the smallest particle volume that can be detected) is largely dependent on the diameter of the pore (the length of the pore, the applied voltage, and the noise of the current trace also have an effect) (24,26-28), as a consequence, the development of this technique follows the development of fabrication methods for micrometer-, submicrometer-, and nanometer-sized pores. During the 1950s and 60s, resistive-pulse sensing was mainly used for examining bacteria and cells (20,22,23) since the commercial instrument sold by Coulter could only detect particles larger than ~500 nm due to the pore sizes that were available (24).

In 1970, Deblois et al. were able to fabricate pores with diameters of ~500 nm in plastic sheets (Lexan polycarbonate) that were ~3 μm thick using a track etch technique (24); the plastic sheet was irradiated with many ions from an accelerator, the ion tracks were chemically etched until pores formed in the membrane (the ion tracks etch faster than the bulk plastic), and a membrane with a single pore was created by sealing all but one pore with epoxy. With these devices, the authors were able to detect particles with diameters as small as 90 nm (24). Building on this research, a few groups published papers in the 1970s, 80s, and early 90s on using resistive-pulse sensing to quantitatively study nanoparticles (25,26), viruses (29-31), and the aggregation of nanoparticles (diameters ≥ 235 nm) by cross-linking with antibodies (32-35). In all of this work, however, the diameter of the pore was never less than ~450 nm and the length of the pore was never less than ~3 μm, which limited the minimum detectable particle diameter to ~60 nm. In order to break past this limit, pores with reduced dimensions were needed.

During the late 1980s and early 1990s, a considerable amount of work examined the interaction of polymers with biological ion channels in lipid bilayers (36). From this research, the idea of using ion channels with their "incredibly" small dimensions (Figure 1.3) as resistive-pulse sensors was born. The first demonstration of this concept appeared in a report published by Bezrukov *et al.* in *Nature* in 1994 (37). While this publication was significant, it was in the end a precursor to the landmark publication by Kasianowicz *et al.* in the *Proceedings of the National Academy of Sciences* in 1996 (38). The report by Kasianowicz *et al.* showed that it was possible to detect single stranded polynucleotide molecules passing through an ion channel protein, α-hemolysin which is

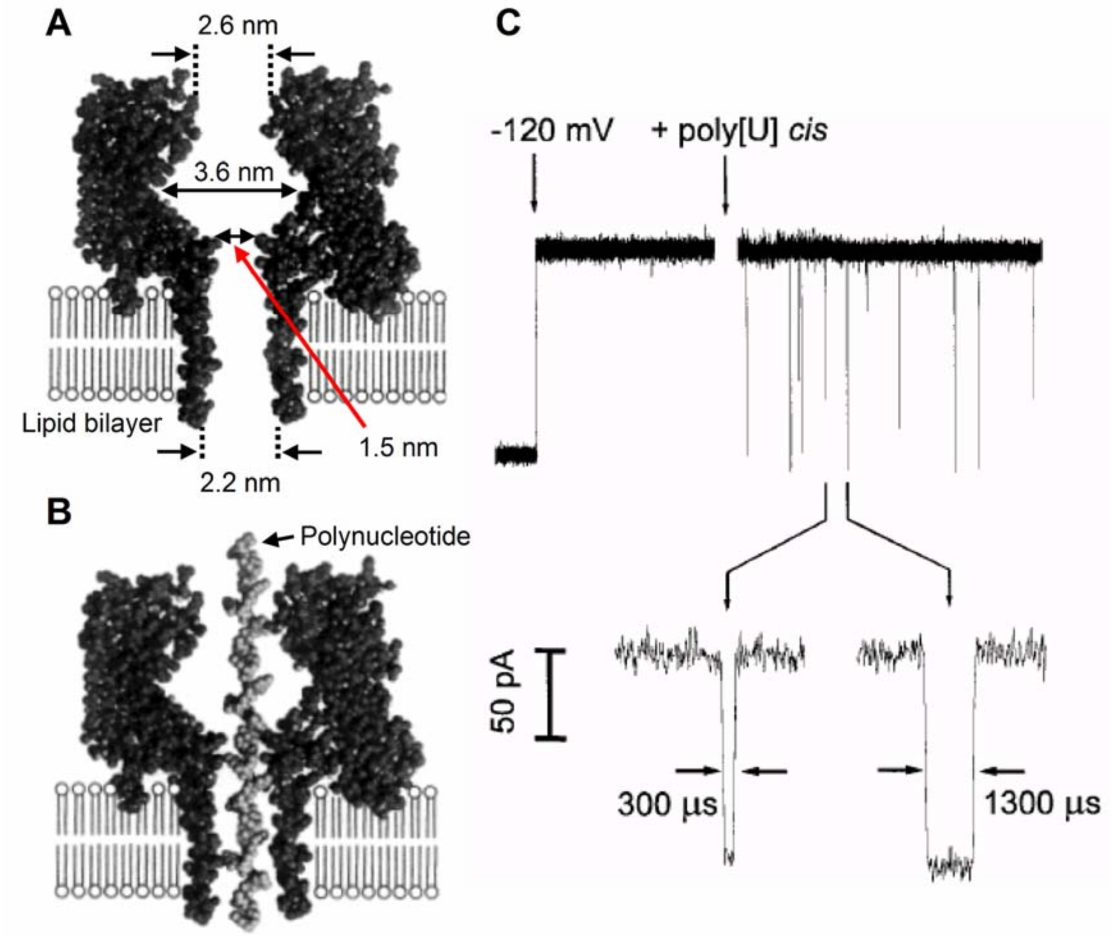

Figure 1.3. Ion channels as resistive-pulse sensors. A) Dimensions of the α-hemolysin ion channel as determined by X-ray crystallography (adapted from Deamer *et al.* (39)). B) Cartoon of a polynucleotide molecule inside a α-hemolysin ion channel (adapted from adapted from Deamer et al. (39)). C) Current passing through the ion channel before and after the addition of polyuridylic acid (poly[U]) to one side of the pore. Note the resistive-pulses that are caused by passage of poly[U] through the pore (adapted from Kasianowicz *et al.* (38)).

secreted by the bacterium *Staphylococcus aureus*, in a planar lipid bilayer with the resistive-pulse technique as shown in Figure 1.3. The demonstration of using resistive-pulse sensing to detect single macromolecules sparked the imaginations of scientists all over the world, and it has lead to a steady increase in the number of publications related to this field ever since (based on a simple search at ISI Web of Knowledge and the Endnote library of the author).

1.3. Resistive-Pulse Sensing After 1996

In the last ten years, a considerable number of studies focused on using ion channels as resistive-pulse sensors for detection and characterization of DNA or RNA(39-56), proteins or small molecules (57-60), bio-affinity interactions (61), chemical reactions (62-65), and changes in protein conformation (66). While these ion-channel sensors have yielded promising results, there are two main drawbacks to using them. First, ion channels have diameters of ~1-3 nm, and are thus limited to analyzing objects below this size. Second, a single ion channel protein must be incorporated into a lipid bilayer; this process itself can be difficult, and the bilayers can be fragile (~4 nm thick and usually micrometers in diameter), sensitive to vibrations and chemical attack, sometimes difficult to form, and not easily integrated into fluidic systems for portable or high throughput applications.

These problems have lead researchers to develop a number of methods for fabricating *synthetic* membranes with single submicrometer pores or nanopores such as i) developing improved track etch techniques (67-72), ii) creating epoxy membranes with single carbon nanotubes (27,73), iii) pulling pipettes with nanometer sized openings (74-76), iv) using cleanroom fabrication techniques alone (28,77,78) or in combination with focused ion beam milling/tuning (79-81), transmission electron microscopy milling/tuning (82-87), or scanning electron microscopy milling/tuning (88,89), v) soft lithography techniques (90,91), and vi) laser-based machining of glass (described in this thesis, see appendix 2.G) (92,93) or polymers (94).

These pores have been combined with the resistive-pulse technique to detect and characterize DNA (75,78,79,83-85,91,95-106), nanoparticles (27,28,73,107-110), binding of antibodies to functionalized nanoparticles (90,111), capture of nanoparticles at the mouth of a pore (112), small molecules (113), and binding of proteins to the mouth of a pore (114). Recent studies combined resistive-pulse sensing with optical tweezers to measure the force on DNA inside a nanopore (115,116). Finally, current recordings from these synthetic nanopores have also been used to study the fundamental aspects of ion transport through the pore (*e.g.* nanopore-based fluidic diodes) (68,117-123), the tomography of a laser focus (124), and the effect of surface properties of the pore on the generation of 1/f noise (85,125,126).

1.4. Dissertation Outline

Up until 1996, four reports explored the use of resistive-pulse sensing to monitor the formation of assemblies from nanoparticles with diameters ≥ 235 nm (32-35). Since then, two additional reports on monitoring the binding of antibodies to nanoparticles with a diameter of 510 nm (90,111) appeared. These six reports, to the knowledge of this author, are the sum total of the work on using resistive-pulse sensing for monitoring the formation of assemblies (nano or otherwise). Even though the scientific community seems to have so far overlooked this application, as we demonstrate in this thesis, it may be one of the most promising and powerful applications.

In Chapter 2, we discuss experiments that use resistive-pulse sensing for detecting and characterizing the formation of biological nanoassemblies made of antibodies and antigens (these assemblies are also known as immune complexes). These experiments are the first demonstration of using resistive-pulse sensing for detecting immune complexes. This method enabled the rapid detection (within tens of minutes) of purified proteins at concentrations as low as 30 nM without the use of labels or immobilization of the antibody or antigen; we also demonstrated the detection of proteins in samples containing complex media such as serum. With this technique, we also were able to monitor the time-course of the formation and growth of the immune complexes. Since resistive-pulse sensing detects and characterizes individual assemblies, we obtained true histograms of the volumes of the immune complexes, which allowed for an examination of the change of the polydispersity of the immune complexes with time.

In Chapter 3, we discuss experiments that use resistive-pulse sensing for detecting and characterizing the formation of biological nanoassemblies consisting of antibodies and viruses. These experiments are the first demonstration of using resistive-pulse sensing for detecting antibody-virus interactions. With this technique, we were able to monitor quantitatively the time-course of the binding of serum-based antibodies to virus particles in their native, assembled state. By examining different ratios of the concentration of virus to antibody, we estimated that the maximum number of antibodies able to bind to the virus was 4200 ± 450. This technique was label free, required no immobilization of the antibody or virus, and can also be used to detect a specific virus or a virus-specific antibody in solution and probe the ability of an antibody to immunoprecipitate the virus.

In Chapter 4, we developed theory for extracting the solid-phase affinity constant of an antibody for binding to its antigen from resistive-pulse sensing experiments. This work is the first demonstration of using resistive-pulse sensing for determining the solid-phase affinity constant of an antibody. We validated this theory by analyzing resistive-pulse sensing data from published experiments (90) that detected the binding of antibodies to colloids (diameter of 510 nm) functionalized with antigen; we calculated an affinity constant of $2.6 \cdot 10^{8} \pm 0.8 \cdot 10^{8}$ M^{-1} which was in agreement with the specifications of the supplier of the antibody.

In Chapter 5, we describe in detail the signal bandwidth and noise of current recordings from glass and polyethylene terephthalate (PET) membranes that contain a single submicrometer pore or nanopore. This work is the first detailed examination of the noise and signal bandwidth of current recordings from synthetic membranes that contain a single submicrometer pore or nanopore. These two parameters are critical for pore-based sensing since the signal bandwidth determines the accuracy with which a change in the current flowing through the pore is detected while the noise directly influences the sensitivity (*i.e.* the signal to noise ratio) of a given pore. We examined the signal bandwidth of each experimental element (*i.e.* amplifier, pore, digitizer, etc…) that was used in recording the current, as well as the overall signal bandwidth of the current recordings. We then examined the individual sources of noise that were expected to contribute to the overall noise of the recordings, and we present theoretical equations describing these noise sources. By combining theory with experiments, we were able to predict the total noise of recorded current traces with a maximum error of 12% when no voltage was applied. Application of a voltage generated in some, but not all cases, an extra noise component that appeared to be of a 1/f origin; predictions of the noise were typically still accurate within 35% error. Based on the detailed discussion presented in this chapter, we provided suggestions for minimizing the noise of current recordings thereby enabling recordings at high signal bandwidths (> 10 kHz) and for obtaining current recordings from resistive-pulse sensing experiments with adequate signal bandwidth to resolve fully resistive pulses.

In Chapter 6, we summarize the major results of this work and provide suggestions for future research.

CHAPTER 2

LABEL FREE AFFINITY ASSAYS BY RAPID DETECTION OF IMMUNE COMPLEXES IN SUBMICROMETER PORES

2.1. Introduction

We present a method based on a submicron pore for detecting and characterizing immune complexes consisting of proteins such as staphylococcal enterotoxin B (an agent with bioterrorism potential) and polyclonal antibodies. The assay is rapid, label-free, requires no immobilization or modification of the antibody or antigen, and achieves single aggregate sensitivity by monitoring changes in electrical resistance when immune complexes pass through a submicron pore. Adopting a recently developed nanofabrication technique based on a femtosecond-pulsed laser made it possible to fabricate pores with conical geometry with diameters as small as 575 nm. These pores allowed sensing immune complexes which consisted of 610 – 17,300 proteins and detecting proteins at concentrations as low as 30 nM. Monitoring the passage of individual immune complexes enabled determining the size-distribution and following the growth of these complexes. This method senses immune complexes (and potentially other molecules or nanoparticles that can be induced to form specific assemblies) in solution, and the antibody or antigen can be present in complex media such as serum. Due to the small footprint and simple detection scheme, submicron pore-based sensing of specific complexes may enable portable or high throughput immunoassays for diagnostics and biodefense.

Coulter counting (resistive-pulse sensing), which monitors the transient change in resistance (resistive-pulse) that occurs when a particle passes through a small pore filled with electrolyte, is a technique for detecting and analyzing micro-, and increasingly, nanoscale objects. Since the sensitivity of a Coulter counter increases with decreasing pore diameter and length,(24) numerous techniques have been developed for fabricating single nanopore (67,70,79,82-85,97,127) or nanotube membranes (24,27,90,91). Pore-forming proteins in planar lipid bilayers (PLBs) have been used elegantly as versatile nanopore sensors (38,51,53,59-61,128); fabricated structures, in comparison, can offer a high degree of robustness and withstand environmental stress such as vibration, pressure, extreme pH, and elevated temperature. Fabricated nanopores and nanotubes have been used for resistive-pulse sensing to detect viruses (30), the aggregation of colloids (33), DNA (79,83-85,91,97), nanoparticles (24,27,28,109), and proteins (90,114). The two reports on protein detection relied on immobilized molecular recognition agents on the walls of the nanopore (114), or on functionalized colloids (90). We hypothesized that a specific protein could be detected rapidly without the need for immobilization or labeling by combining a submicron pore with Coulter counting to monitor the formation of immune complexes in solution.

2.2. Pore Fabrication and Characterization

We adopted and optimized a recently developed nanomachining technique that employs femtosecond-pulsed lasers (129-131) to fabricate submicron pore structures in borosilicate glass coverslides (Figure 2.1) (see Appendix 2.G for a more detailed description of the laser nanomachining). This technique has the advantage that it does not require masks, etching, or high vacuum and that it can fabricate in glass. Glass is an excellent substrate material due to its low-noise properties (132), its chemical and mechanical robustness, and its amenability to surface functionalization. In addition, laser nanomaching is able to fabricate complicated 3-D structures in optically transparent substrates (133) which enabled us to machine pores with conical geometry and diameters of 575, 650 (Figure 2.1b,c), and 900 nm (see Appendix 2.C for SEM images of the 575 and 900 nm pore). The conical shape makes it possible to produce low-resistance pores in thick (> 1 μm) membranes that have low electrical capacitance (134). Reducing the resistance increases the amplitude of resistive pulses as well as the transport rate through the pore for a given pore diameter (85,109). Lowering the capacitance can reduce electrical current noise (134,135), which permits recording at high bandwidth (134) and increases the sensitivity of the Coulter counter (27).

We mounted the glass slides with the pores onto a fluidic setup (Figure 2.2) made of poly(dimethylsiloxane) (PDMS) to characterize their electrical properties and to perform the affinity assays. The composition of the recording buffer, the resulting electrical resistances, and the noise values of the pores are listed in Appendix 2.A. Before studying immune complexes, we characterized the response of the nano-Coulter

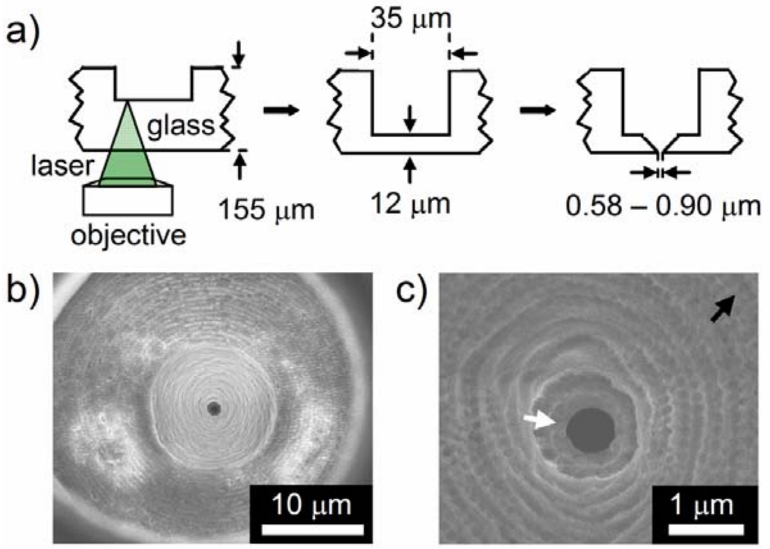

Figure 2.1. Laser-based fabrication of submicron pores with conical geometry. a) Femtosecond-pulsed lasers enabled nanomaching of conical pores with diameters as small as 575 nm in glass. b) Scanning electron microscope (SEM) image looking into the 35 µm cylinder of a pore (see a). c) SEM image focused on the narrowest part of the pore (diameter: 650 nm). The conical shape of the pores was confirmed by observing different focal planes while using the SEM (white arrow: in focus; black arrow: out of focus).

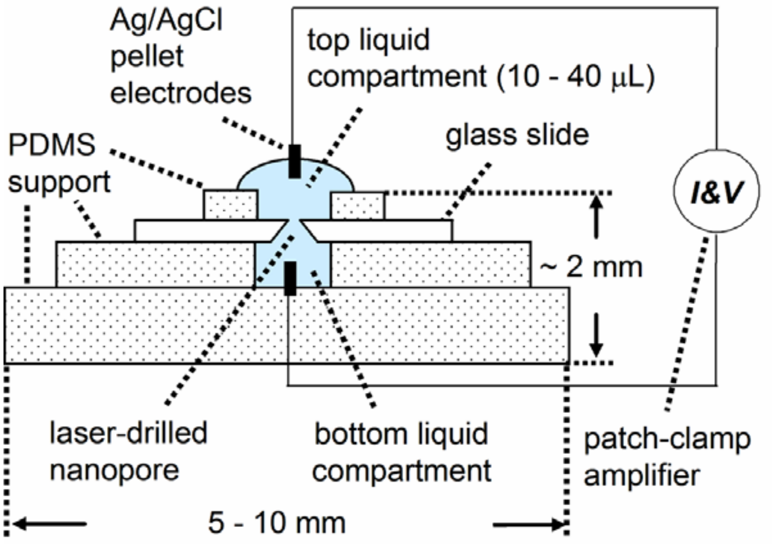

Figure 2.2. Sideview of the experimental setup. A patch-clamp amplifier applies a constant voltage and detects small changes in current (pA-range) with fast time-resolution (~50 kHz). A poly(dimethylsiloxane) (PDMS) fluidic setup allows for replacement of solution on either side of the submicron pore.

counter using synthetic nanoparticles. In a *cylindrical* pore the resistive-pulse from a spherical particle is proportional to the volume of the particle (as long as the particle diameter is less than ~0.4 of the diameter of the pore) (24). When we passed particles with diameters of 100, 130, and 160 nm through a *conical* pore, we also observed a linear relationship between the amplitude of the current peak and the particle volume (see Appendix 2.C). This linear relationship, in conjunction with evidence that particles of the same volume but varying shape give rise to resistive pulses with similar amplitudes (136), made it possible to estimate the volume of the immune complexes and consequently the number of proteins in a complex (see Appendix 2.B for a detailed discussion on the bandwidth and time resolution required for quantitative analysis of Coulter counting data).

2.3. Detection of Immune Complex Formation in Well-Defined Media

To use the submicron pores for detecting and characterizing immune complexes, we monitored the resistive pulses that occurred when these complexes passed through the pore. The antibody-antigen model system investigated here consisted of a goat anti-mouse antibody and a monoclonal anti-baculovirus antibody from mouse as the antigen (see Appendix 2.D for optical micrographs of immunoprecipitates of this antibody-antigen pair). We examined three different equimolar concentrations, 15, 30, 151 nM, of the antigen and anti-mouse antibody using a pore with a diameter of 650 nm. The pore-based assay was able to detect immune complexes at a concentration of 151 nM and 30 nM as shown by the resistive pulses in Figure 2.3b,c; we did not detect immune

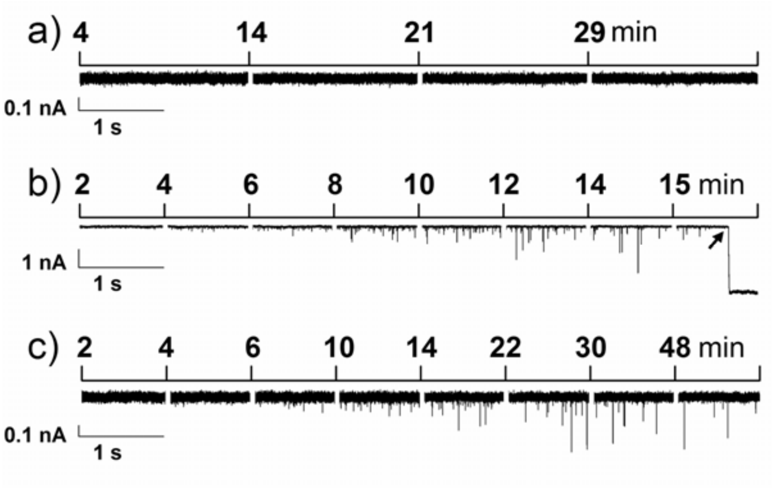

Figure 2.3. Time-courses of the formation of immune complexes in solution. a) Control experiment with the antigen (*mouse* monoclonal antibody against baculovirus) and a non-specific anti-*rabbit* antibody, both at a final concentration of 151 nM. b) At a final concentration of 151 nM of antigen and the specific anti-*mouse* antibody, detectable immune complexes formed rapidly and eventually blocked the pore (arrow). Note the y-scale of b) is ten times larger than the scale of the other traces due to the large size of the immune complexes. c) At a lower antibody-antigen concentration (30 nM), detectable immune complexes formed, but they were smaller and never blocked the pore. Each current trace is composed of multiple short recordings (length 1 – 2 s) that were taken from data files recorded during the course of the experiment; a small gap separates each of these short recordings. The time in minutes after addition of anti-mouse or anti-rabbit antibody to the recording buffer that contained the antigen is indicated above the beginning of each short recording. These recordings therefore represent short "snapshots" of the current activity throughout the entire experiment of several minutes duration. A pore with a diameter of 650 nm (Figure 2.1b,c) was used for these experiments.

complexes at a concentration of 15 nM of antibody and antigen.

Figure 2.3b,c shows that the amplitudes of many resistive pulses caused by the immune complexes formed at a concentration of 151 nM were considerably larger than those formed at 30 nM. This result indicates that immune complexes grew larger at 151 nM compared to 30 nM and may explain why no immune complexes could be detected at a concentration of 15 nM. Indeed, the immune complexes that formed at a concentration of 151 nM grew so large that they eventually blocked the pore (Figure 2.3b, arrow indicates the onset of pore blockage; see Appendix 2.E for a prolonged current trace).

We performed a control experiment using the same antigen and a non-specific goat anti-rabbit antibody at a concentration of 151 nM. We did not detect any immune complexes or pore blockage in the presence of this control antibody (Figure 2.3a). Subsequent addition of the anti-mouse antibody at a concentration of 151 nM produced detectable immune complexes within 3 minutes, and blockage of the pore due to large immune complexes ("immunospecific" blockage) occurred after approximately 9 minutes. This blockage provided a dramatic response (significant and permanent change in the resistance of the submicron pore) that could be sensed using simple electronics with low time resolution; it may potentially be useful for disposable, ultra small, and portable low-power sensors for detection of biowarfare agents such as staphylococcal enterotoxin B (SEB) (see Figure 2.4), botolinum toxin or ricin in the field (114).

2.4. Detection of Immune Complex Formation in Media Containing Serum

To test the ability of the pore-based sensor to detect proteins on a relevant system in complex media, we detected staphylococcal enterotoxin B (SEB) using sheep anti-SEB serum. SEB is a causative agent of food poisoning and has potential for bioterrorism according to the National Institute of Allergy and Infectious Disease of the U.S.A. (137). Addition of the anti-SEB serum to a solution containing SEB caused a strong increase in the size and number of detectable aggregates when compared to the anti-SEB serum alone (Figure 2.4). We obtained similar results with a second system that employed antiserum

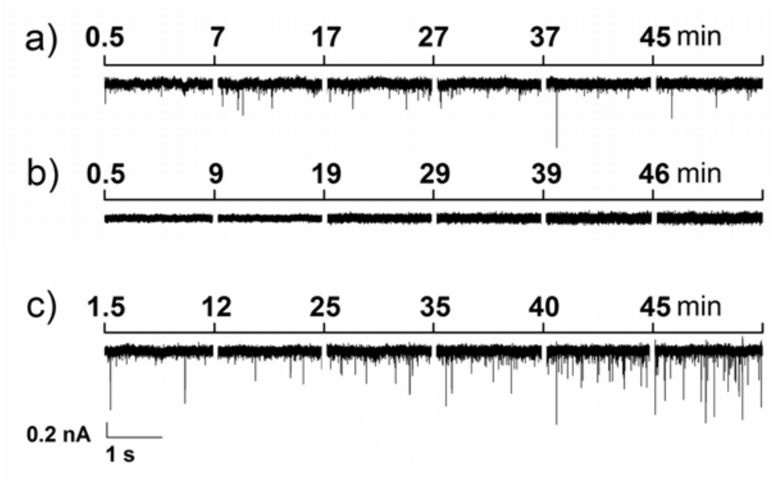

Figure 2.4. Detection of staphylococcal enterotoxin B (SEB) by sensing the formation of immune complexes in media containing a complex sample matrix. a) Current traces of anti-SEB serum only: one microliter of anti-SEB serum was added to 29 μL of recording buffer. The non-specific events were caused by serum components that were not removed by a membrane filter with pores of 0.1 μm. b) Current traces of SEB only (final concentration: 200 nM). c) Current traces of SEB and anti-SEB serum: SEB at a final concentration of 200 nM and 1 μL of anti-SEB serum in a total volume of 32 μL. The addition of anti-SEB serum caused a significant increase in the number and size of events compared to a). Each current trace is composed of multiple short duration (length 2 s) current recordings that were taken from data files recorded at different times during an experiment; a small gap separates each recording. The time in minutes after addition of anti-SEB serum, or SEB, to the recording buffer is indicated above the beginning of each short recording.

from rabbit to detect a monoclonal antibody (see Appendix 2.F). These results demonstrate that submicron pore-based sensors can detect immune complexes in media which contain complex samples such as blood serum.

2.5. Quantitative Characterization of Immune Complexes

In addition to detecting immune complexes and hence antigens or antibodies, submicron pore-based Coulter counting offers the possibility to evaluate specific properties of these complexes such as their volume and growth rate. These properties are important since the size of an immune complex influences its physiological properties, for instance its clearance from circulation and its adherence to phagocytes (16). Studying polydisperse immune complexes is difficult due to their large heterogeneity. Light scattering techniques have been used (16,17); however, since they measure multiple particles at once, these techniques can be problematic for characterizing polydisperse samples (138). In contrast, Coulter counting measures each particle individually and therefore can provide information on the volume, polydispersity, and growth of the immune complexes with single aggregate sensitivity.

To demonstrate these capabilities, we monitored the increase in volume of immune complexes over time (Figure 2.5a,d). The general trend of the average peak amplitudes compares well with data obtained by light scattering (17). The sigmoidal shape in Figure 2.5d may be a consequence of a thermodynamically stable size of the immune complexes (139,140). Figure 2.5a,d shows that the standard deviation of the amplitude of the current peaks increased strongly during the growth of the immune complexes, indicating a strong increase in the polydispersity of the complexes. Interestingly, the majority of immune complexes sensed shortly after addition of antibody (Figure 2.5b,e) had volumes that were comparable to complexes sensed later, 8 min (Figure 2.5c) or 40 min (Figure 2.5f). With increasing time, however, a fraction of complexes reached volumes that were approximately two times larger than the predominant volumes (Figure 2.5f). This result suggests that the later stage of growth may have been caused by collisions between slowly diffusing complexes (17), and may

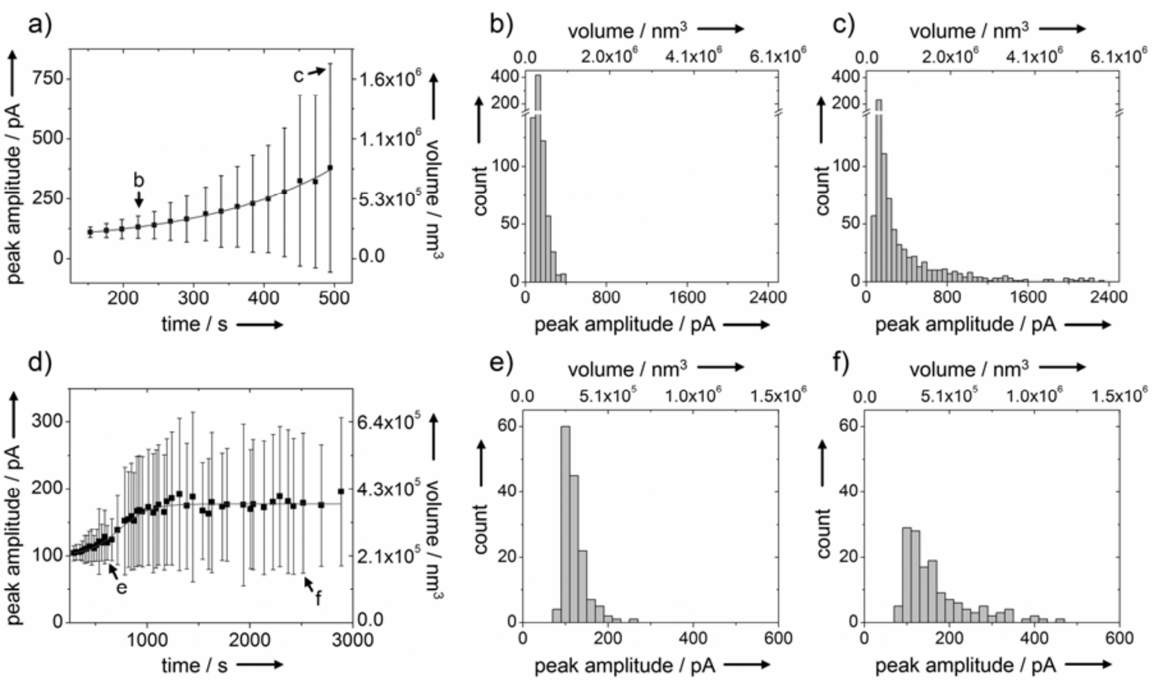

Figure 2.5. Time course of the current peak amplitudes and volumes of immune complexes. a) Growth of immune complexes at a concentration of 151 nM of both antigen (monoclonal antibody from mouse against baculovirus) and anti-mouse antibody. A first order exponential function was fitted to the data (17). The small letters in the graph correspond to the time points from which the histograms shown in b), c) were extracted. b) Peak amplitudes and volumes recorded 240 s after addition of anti-mouse antibody. c) Peak amplitudes and volumes recorded 490 s after addition of anti-mouse antibody. Note that 74% of the complexes maintained their volumes compared to b), however a small fraction of complexes reached volumes that were up to 10 times larger than in b). d) Growth of immune complexes at a concentration of 30 nM. A sigmoidal function was fitted to the data (17). The small letters in graph d) correspond to the time points from which the histograms shown in e) and f) were extracted. e) Peak amplitudes and volumes recorded 610 s after the addition of anti-mouse antibody. f) Peak amplitudes and volumes recorded 2400 s after the addition of anti-mouse antibody. Note the occurrence of peak amplitudes with approximately two-, three-, and four-times the change in current (~200, 300, 400 pA) of those shown in e). Each point in a), d) reflects the average amplitude and aggregate volume obtained from peaks over a period of 20 seconds.

explain the relatively rare formation of complexes that are significantly larger than the majority.

Due to the linear relationship between peak amplitude and volume of immune complexes, we were able to estimate the number of proteins in an aggregate by assuming a molecular volume of 347 nm^3 for an immunoglobulin G antibody (141). The volumes of the immune complexes sensed by the pore with a diameter of 650 nm and an antibody antigen concentration of 151 nM ranged from $2.1 \cdot 10^5 - 6.0 \cdot 10^6$ nm^3, corresponding to aggregates of 610 – 17,300 proteins.

2.6. Conclusion

Submicron pore-based detection of immune complexes offers a general, rapid, label-free, and solution-based method for the detection of any protein or particle that can be triggered to form a detectable assembly, while providing information on the volume, growth, and polydispersity of individual aggregates. The detection limit of 30 nM for antigens compares favorably to other label-free detection techniques such as affinity capillary electrophoresis (ACE), gel-based immunoprecipitation, and direct immunoaggregation assays based on light-scattering which have detection limits between 10 and 1000 nM depending on the technique (142-144). In addition to its benefits for affinity assays with small footprints and reagent requirements, the technique presented here may be particularly useful for *in situ* monitoring of controlled assemblies of nanoparticles (5,6,145), thereby addressing an urgent need in nanotechnology (9).

2.7. Acknowledgements

This work was supported by a research grant from IMRA America, AISIN U.S.A. and seed funds from the College of Engineering, University of Michigan. The authors thank Daniel J. Estes, Amy P. Wong, Irina Gitlin, and Paul Bina for valuable discussions.

CHAPTER 2 APPENDICES

2.A. Electrical Current Noise of Submicron Pores with Conical Geometry

The noise values reported in Table 1 are considerably higher than reported values for planar lipid bilayer (PLB) experiments (*e.g.* PLB experiments report a current noise of < 1 pA RMS at a bandwidth of 3 kHz) (134,146). This discrepancy is due to the large difference in resistance between the submicron pores used (1-2 MΩ) and PLBs (> 10 GΩ). The large resistance of PLBs leads to currents in the pA range, and under these low-current conditions the noise of the recordings is dominated by two sources: 1) the thermal voltage noise of the access resistance i_{rc} and 2) the noise resulting from the interaction of the headstage noise with the input capacitance i_{vc}. In the present work, a planar lipid bilayer was not formed over the submicrometer pores and consequently the resistance values were significantly lower than pores that have a bilayer on them. Under these conditions, the thermal noise, i_{th}, dominates. Thermal noise is defined as (147):

$$i_{th} = \sqrt{\frac{4kTB}{R}} \tag{2.A.1}$$

where k is the Boltzmann's constant, $1.38 \cdot 10^{-23}$ m^2 kg s^{-2} K^{-1}, T is the temperature in kelvin, R is the resistance of the pore, and B is the bandwidth. With the experimental values of $R = 1.4 \cdot 10^6$ Ω, $T = 294$ kelvin, and $B \approx 10{,}650$ Hz, the theoretically expected RMS noise was ~11 pA, which is somewhat lower than the value that is reported in Table 2.A.1. The noise recorded was most likely somewhat higher than the theoretical expectation due to other sources of noise such as amplifier noise and dielectric noise. In any event, the experimentally recorded RMS noise value of 16 pA was low when considering the "large" current of 140 nA during the recordings in the present work. This low noise value confirms that the design of the pores and the material properties of the glass substrate are well-suited for Coulter counting of nanoscale objects.

Table 2.A.1. Electrical resistance and current noise of submicron pores with conical geometry

Diameter of pore (nm)	Resistance MΩ	Noise at 10 kHz[a] (pA RMS)	Noise at 1 kHz[a] (pA RMS)
900	1.1	17.1	10.1
650	1.4	16.0	8.9
575	1.8	14.1	7.5

[a] A digital Gaussian low-pass filter with the specified cutoff frequency was used. All noise values were obtained at an applied potential of 0.2 V in recording buffer (150 mM KCl; 50 mM tris(hydroxymethyl)aminomethane (TRIS), pH 7.8; 0.1 mg mL^{-1} bovine serum albumin; 0.1% w/v Tween 20).

2.B. Determination of the Time Resolution Required for Accurate Extraction of Quantitative Information from Coulter Counting Analysis

Extracting quantitative data from Coulter counting experiments requires careful design of the recording system and the pore since these two entities determine the bandwidth of the measurement. The bandwidth is one of the most important aspects of the recorded data because it determines the time resolution. The time resolution of the measurement sets the upper bound of the "speed" at which changes in current can be recorded. That is, if a change in current occurs faster than the time resolution of the recording, then the recorded current "jumps" from one value to the next and the intervening information on how the current arrived at this value is lost. In the context of a Coulter counting experiment, the time resolution of the measurement determines the maximum resolution with which the resistive pulse of a particle can be observed while it passes though the pore. If it moves faster than the time resolution, then the peak amplitude of the resistive-pulse will be clipped. This clipping can cause inaccuracies in calculations that use the peak amplitude. Another important aspect of recording data accurately is the sampling frequency. According to the Nyquist theorem, the sampling frequency should always be at least 4 times the bandwidth of the recording.

In the absence of both filtering and series resistance compensation, the maximum possible bandwidth that is obtainable in a Coulter counting experiment is determined by the access resistance of the pore and the capacitance of the substrate (135). The resistance of the pore in parallel with the capacitance of the substrate that supports the pore forms a one-pole low-pass RC filter (135). The maximum bandwidth of this filter can be estimated by the following equation (135):

$$B \leq \frac{1}{2\pi RC} \qquad (2.B.1)$$

where R is the resistance leading to the pore and C is the capacitance of the substrate. Since we used glass (a very good dielectric) and since the geometry of the pores that we used in this work was conical (and did not include a thin, insulating membrane), the capacitance of the substrate was extremely low (~ 10 pF). Assuming a resistance of 1200

Ω (the maximum resistance leading to the pores we fabricated), the theoretical bandwidth of the recording was 13 MHz (see Chapter 5 for a more detailed discussion). According to the manufacturer, the maximum bandwidth that was available from our recording system in the configuration that we used was approximately 50 kHz (β = 0.1, whole-cell mode); therefore the overall bandwidth of our measurement was not limited by the recording chip but by the amplifier. It was, however, considerably higher than the bandwidth of 8 – 9 kHz that was required for reliable analysis of the data recorded in this work (see below).

In order to determine the bandwidth required to measure accurately the amplitude of the current peaks, we examined the power spectra of current traces with and without events as shown in Figure 2.B.1. These two power spectra show that an accurate detection of the events required a bandwidth of approximately 8 – 9 kHz. This result allowed us to reduce the RMS noise of the current traces by filtering with a digital low-pass filter (Gaussian) with a cutoff frequency of 10 kHz. Since the events only required a bandwidth of 8 – 9 kHz, the amplitude of the peaks was not reduced by the 10 kHz filter as illustrated in Figure 2.B.2c. In fact, Figure 2.B.2e shows that filtering with a cutoff frequency as low as 5 kHz would have reduced the amplitude of the signal only marginally. Significant reduction in amplitude was observed when using a cutoff frequency of 1 kHz (Figure 2.B.2f). After filtering all recorded data with a 10 kHz low-pass filter, we decimated the data to a sampling frequency of 50 kHz. As predicted by the Nyquist sampling theorem, this decimation also had no effect on the peak amplitude (Figure 2.B.2c,d).

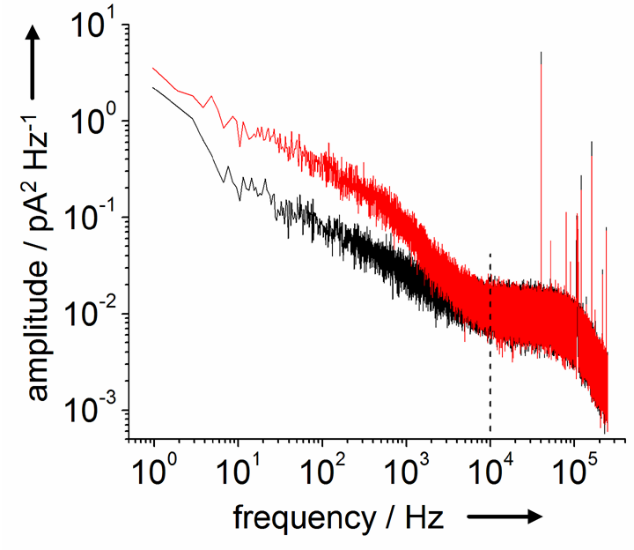

Figure 2.B.1. Power spectra of original current traces with and without events (here immune complexes). Both current traces were recorded at maximum bandwidth of the recording setup (~50 kHz). The power spectrum of the current trace with events (red) contained significantly more low frequency content than the power spectrum of the current trace without events (black). As determined from the plot, the maximum frequency component of the events was approximately 8 – 9 kHz. Therefore the current trace could be processed by low-pass filters with cutoff frequencies of 10 kHz (dotted line) without causing significant signal distortion. The average peak amplitude of the events in the current trace was 123 ± 40 pA. The current traces were obtained from a pore with a diameter of 650 nm.

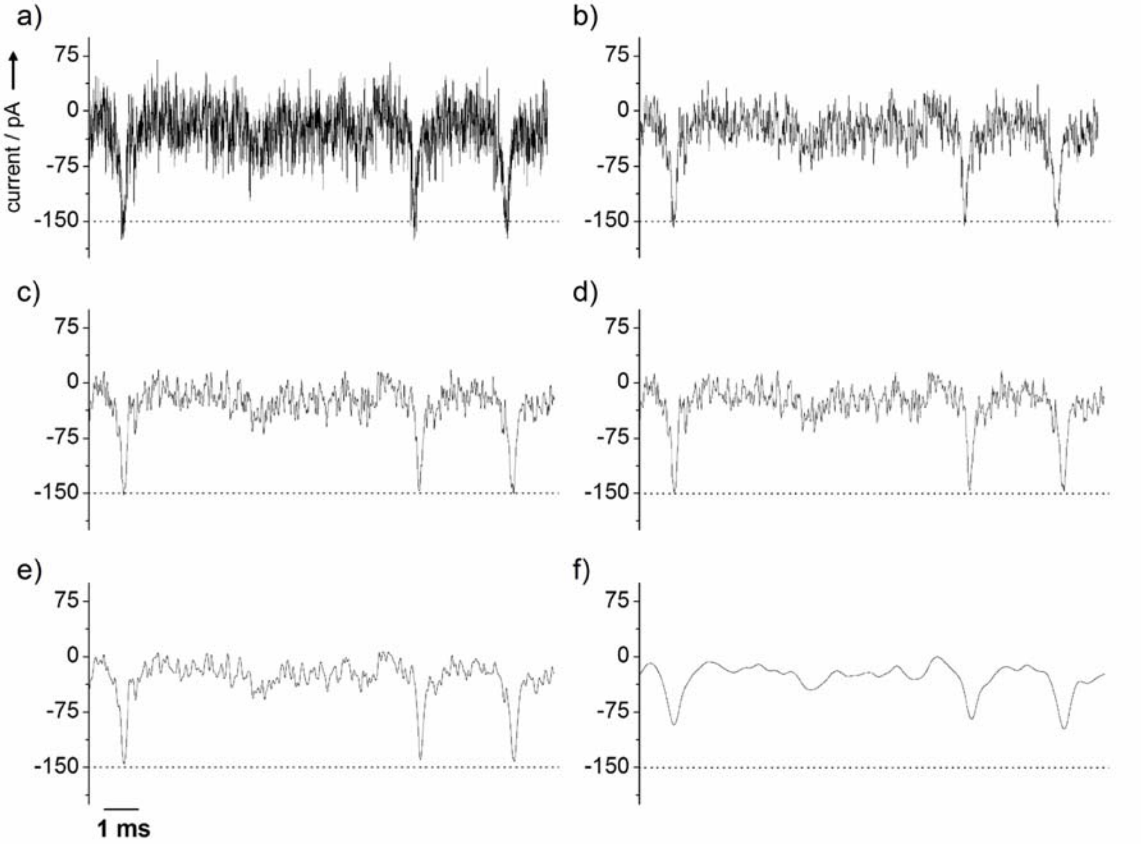

Figure 2.B.2. Effect of the cutoff frequency used for low-pass filtering on the peak amplitudes of current events during passage of immune complexes through a submicron pore. a) Current trace with three events after filtering with a digital (Gaussian) low-pass filter with a cutoff frequency of 50 kHz. b) Same current trace after filtering with a cutoff frequency of 20 kHz. The difference in the peak amplitude of the events between trace a) and b) was due to the reduction in current noise (from 26 to 17 pA RMS) and not due to clipping of the peak as a result of the reduced filter cutoff frequency. c) Same current trace after filtering with a cutoff frequency of 10 kHz. d) Same current trace as in c) but decimated to a sampling frequency of 50 kHz, instead of 500 kHz as in a)-c). As predicted by the Nyquist sampling theorem, the amplitude of the signal did not change significantly. e) Same current trace after filtering with a cutoff frequency of 5 kHz. The peak amplitude of the events decreased slightly since the cutoff frequency of the filter was below the maximum frequency component of the events (8 – 9 kHz, see Figure 2.B.1) f) Same current trace after filtering with a cutoff frequency of 1 kHz. Since the cutoff frequency of the filter was significantly below the maximum frequency component of the events, the events are distorted and the peak amplitude has decreased by a factor of approximately 0.5. The digital filters were always applied to the original, high-bandwidth current trace. The resistive-pulses were caused by immune complexes passing through a pore with a diameter of 650 nm.

2.C. Peak Amplitude is Proportional to the Volume of Spherical Particles in Submicron Pores with Conical Geometry

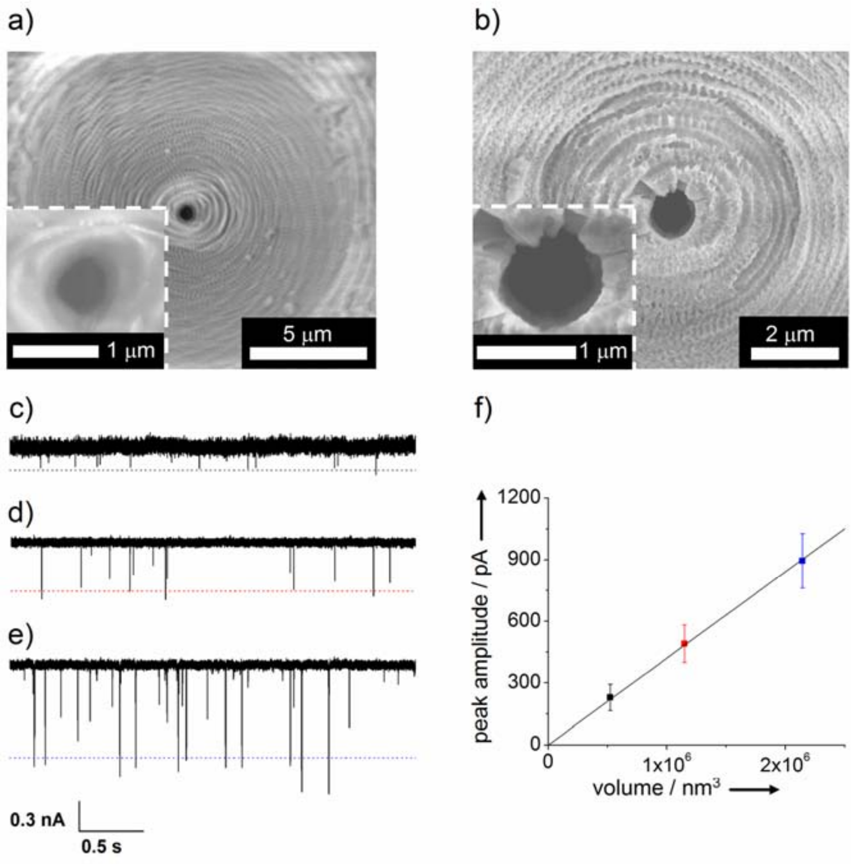

Figure 2.C.1. SEM images of conical pores with diameters of 575 and 900 nm and determination of the relationship between peak amplitude and particle volume in conical pores with submicron diameter. a) SEM image looking into the 35 μm cylinder of the pore with a diameter of 575 nm. The inset shows a close-up of the narrowest part of the pore. b) SEM image looking into the 35 μm cylinder of the pore with a diameter of 900 nm. The inset shows a close-up of the narrowest part of the pore. c) Current versus time trace of particles with a diameter of 100 nm passing through the pore shown in a). The dotted line represents the mean current amplitude of the peaks. d) Current versus time trace of particles with a diameter of 100 and 130 nm (mean current amplitude from the 130 nm particles in red) passing through the pore shown in a). e) Current versus time trace of particles with a diameter of 100, 130, and 160 nm (mean current amplitude from the 160 nm particles in blue) passing through the pore shown in a). f) Plot of the average peak amplitude of the resistive-pulses caused by particles with a diameter of 100, 130, and 160 nm passing through the pore shown in a) versus particle volume. The data were fitted using a linear regression algorithm that required the line to pass through the origin; the slope of the line was $4.2 \cdot 10^{-4}$ pA nm^{-3}. We obtained a slope of $3.9 \cdot 10^{-4}$ pA nm^{-3} for the pore with a diameter of 650 nm (Figure 2.1b,c).

2.D. Confirmation of Formation of Immune Complexes by Phase Contrast and Fluorescence Microscopy

We performed immunoprecipitation experiments in 0.5 mL vials in order to verify that the anti-mouse antibody formed immune complexes with the monoclonal antibody from mouse against baculovirus (here used as the antigen). The antibody and antigen were added to recording buffer at the concentrations listed in Table 2.D.1. The vials, each containing 20 μl of solution, were initially vortexed and then left at room temperature for ≥ 2 hours without agitation. The total volume was carefully removed from the vial, placed on a clean microscope slide, and covered with a clean cover glass.

Table 2.D.1. Antibody and antigen concentration used to verify the formation of immune complexes by microscopy

Vial	Polyclonal antibody (μM)	Antigen (μM)	Total protein (μM)
1	1.33	0	1.33
2	0	1.33	1.33
3	0.667	0.667	1.33

We examined these slides using a Nikon Eclipse TE 2000-U inverted microscope with a 20× objective in phase-contrast mode. We did not see any complexes when only the antibody (Figure 2.D.1b,c) or the antigen (Figure 2.D.1a) was present at a concentration of 1.33 μM. In contrast, when both the antigen and antibody were present at a concentration of 0.667 μM (total protein concentration = 1.33 μM), immune complexes could be detected as shown in Figure 2.D.1d,e.

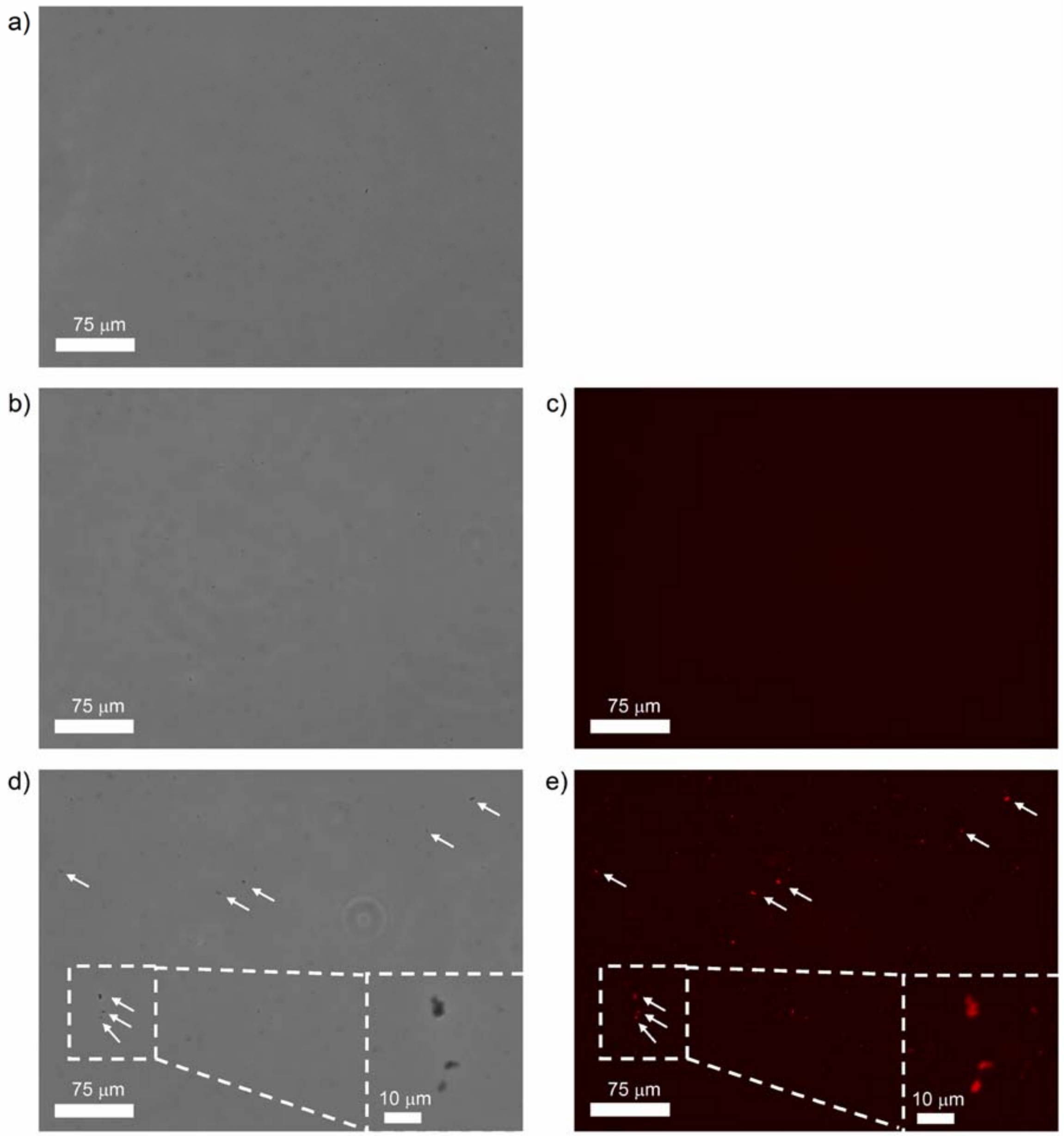

Figure 2.D.1. Microscope images to verify the specific formation of immune complexes. a) Control experiment with the monoclonal antibody from mouse against baculovirus (antigen) at a concentration of 1.33 μM. No protein aggregates were seen on the slide by phase contrast microscopy. b) Control experiment with the anti-mouse antibody from goat that was labeled with tetramethylrhodamine isothiocyanate (TRITC) at a concentration of 1.33 μM. No protein aggregates were seen on the slide by phase contrast microscopy. c) False colored fluorescence image of the same field of view as in b). No protein aggregates of the fluorescently-labeled antibody were visible. d) Immunoprecipitation experiment with the antigen and anti-mouse antibody each at a concentration of 0.67 μM. The phase contrast image shows at least eight micron-sized immune complexes (indicated with white arrows). e) False colored fluorescence image

of the same field of view as in d). We used a typical fluorescent filter set for rhodamine, an exposure time of 1 s, and the maximum intensity of excitation of the lamp (Exfo X-Cite 120, Photonic Solutions, Mississauga, Ontario) to capture this image. All of the images were captured with a CCD camera (Photometrics CoolSnap HQ, Roper Scientific, Trenton, NJ) and processed using image analysis software (Metamorph, Universal Imaging, Downington, PA).

2.E. Blockage of Submicron Pores by Biospecific Formation of Large Immune Complexes

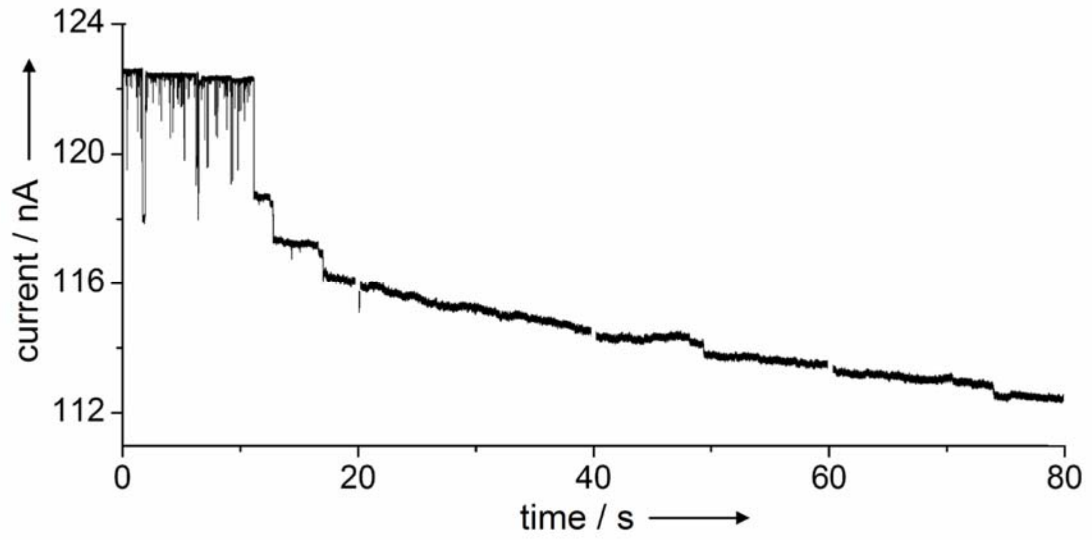

Figure 2.E.1. Blockage of the submicron pore with a diameter of 650 nm by large immune complexes. At a concentration of 151 nM monoclonal antibody from mouse against baculovirus (here used as the antigen) and 151 nM anti-mouse antibody, the resulting immune complexes grew large enough that they clogged the pore as indicated by step-wise increases in electrical resistance (blockage started approximately 15 minutes after addition of anti-mouse antibody). This "immunospecific blockage" may be useful for simple detection of antibody-antigen interactions. The graph is composed of several concatenated data files; a small gap separates each file.

2.F. Sensing the Formation of Immune Complexes in the Presence of Serum

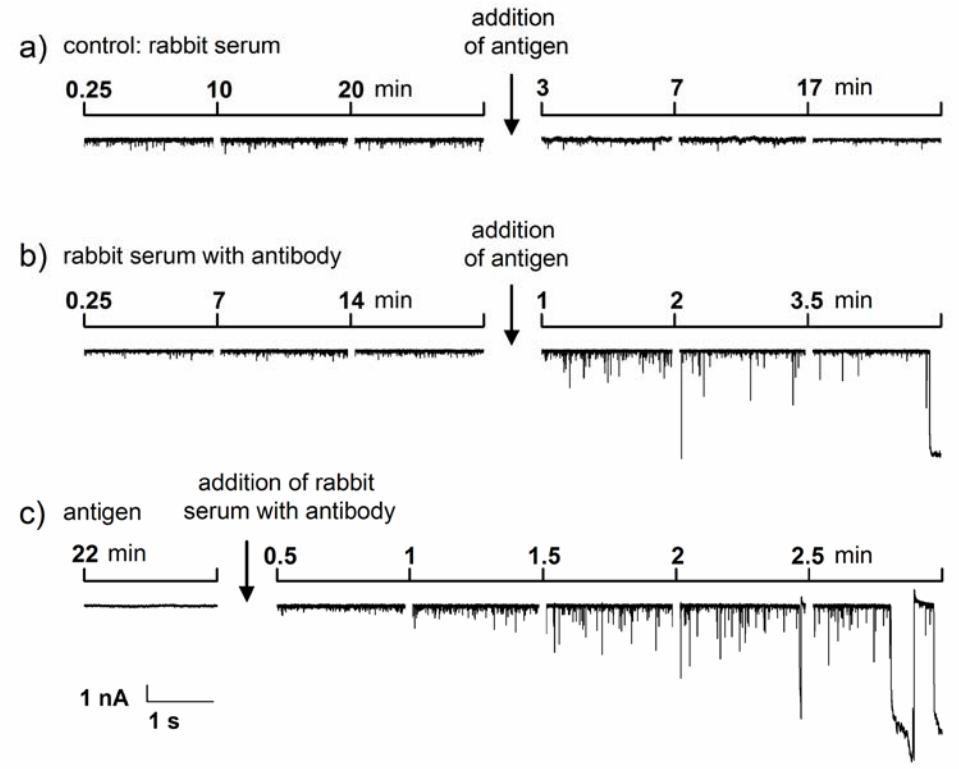

Figure 2.F.1. Time courses of the formation of immune complexes in a solution containing serum. a) Control experiment with 2 µL serum from a rabbit that was not immunized (filtered through a membrane with pores of 0.1 µm) added to 40 µL of recording buffer. Note the presence of small peaks that were caused by serum components not removed by the filter. Addition of the antigen (here *mouse* monoclonal antibody against baculovirus) to a final concentration of 151 nM did not cause any change in the signal. b) Anti-mouse antibody was dissolved in unfiltered rabbit serum and then this mixture was filtered using a membrane filter with 0.1 µm pores. A volume of 2 µL of rabbit serum containing anti-mouse antibody was added to 40 µL of recording buffer; the final concentration of antibody was 151 nM. Addition of the antigen to a final concentration of 355 nM caused a significant increase in the number of events and the size of the events. c) Antigen was added to a final concentration of 151 nM. As expected from Figure 3a, no events resulted from passage of antigen alone through the pore. Addition of 2 µL of rabbit serum containing anti-mouse antibody to 42 µL of recording buffer initiated the formation of immune complexes; the final concentration of antibody was 151 nM. As seen in b), immune complexes rapidly formed causing a significant increase in the number of events and the size of the events. Each current recording is composed of multiple concatenated data files; a small gap separates each file. The time in minutes since addition of rabbit serum, or antigen is indicated above the beginning of each file. A pore with a diameter of 575 nm (Figure 2.C.1a) was used for all experiments.

2.G. Materials and Methods

Solutions. We prepared all solutions with deionized water (resistivity of 18.2 MΩ cm, Aqua Solutions, Jasper, GA) and used potassium chloride, sulfuric acid (both from EMD Biosciences, La Jolla, CA), TRIS (Shelton Scientific, Shelton, CT), bovine serum albumin (Sigma, St. Louis, MO), Tween 20 (Mallinckrodt Chemicals, Phillipsburg, NJ), hydrochloric acid (VWR International, West Chester, PA), nitric acid (Fluka Chemie, Buchs, Switzerland), and hydrogen peroxide (EMD Chemicals, Gibbstown, NJ) without further purification. Recording buffer was filtered through sterile 0.1 or 0.2 μm, low protein absorption polyethersulfone membrane filters (both from Pall, East Hills, NY).

We used affinity-purified monoclonal antibody from mouse against baculovirus envelope gp64 protein (eBioscience, San Diego, CA) without further modification. Affinity-purified goat anti-mouse antibody (H+L) conjugate labeled with tetramethylrhodamine isothiocyanate (TRITC) and affinity-purified goat anti-rabbit antibody (H+L) conjugate labeled with TRITC (Zymed, San Francisco, CA) were diluted in recording buffer and filtered through either a 0.1 μm or 0.2 μm membrane filter. The TRITC labels on these antibodies were not used for the submicron pore assays but were useful to perform control experiments of immunoprecipitation with fluorescence microscopy (see Figure 2.D.1). We filtered the sheep anti-SEB serum and purified SEB (both from Toxin Technology, Sarasota, FL) through a 0.1 μm membrane filter. We used the 100, 130, and 160 nm particles (polystyrene microspheres functionalized with carboxyl groups, Bangs Laboratories, Fishers, IN) at a concentration of $\sim 1 \cdot 10^{10}$ particles mL^{-1} in recording buffer.

Nanomachining using a femtosecond-pulsed laser. We fixed a cover glass (Corning 0211 borosilicate, Fisher Scientific, Pittsburgh, PA) to a 3-axes microscope nanomanipulation stage (Mad City Labs, Inc., Madison, WI) as shown in Figure 2.G.1. A few drops of water were placed on the upper side of the cover glass at the area that was to be machined (if the machining time was greater than 30 minutes, we used an aluminum compartment sealed with tape to minimize evaporation of water). The laser, a directly diode-pumped Nd:glass CPA laser system (Intralase Corp., Irvine, CA), was focused through the a 100x oil immersion microscope objective (N.A. = 1.3, Zeiss, Thornwood, NY) and the cover glass to the machining site (Figure 2.1a). We used pulses with a duration of 600-800 fs (femtoseconds) that were frequency doubled from 1053 nm to 527 nm. The glass was machined by scanning the laser in circular patterns which removed material layer by layer. Since the subsequent layer was formed under water, machining always proceeded at the glass-water interface. The submicron pores were machined in a three stage process. We used the following parameters for the pores: 35 µm cylinder machined with 60-80 nJ per pulse at a frequency of 1.5 kHz; wide part of the cone machined with 12-15 nJ per pulse at 1.5 kHz; tip of the cone machined with 8-13 nJ per pulse at 10 Hz. After machining, we left the glass coverslides in water for 12 hours with the 35 µm cylinder facing down; this configuration facilitated settling of debris out of the pore. The glass coverslides were cleaned in a fresh mixture of 3:1 concentrated sulfuric acid to 30% hydrogen peroxide for at least 15 minutes, prior to use.

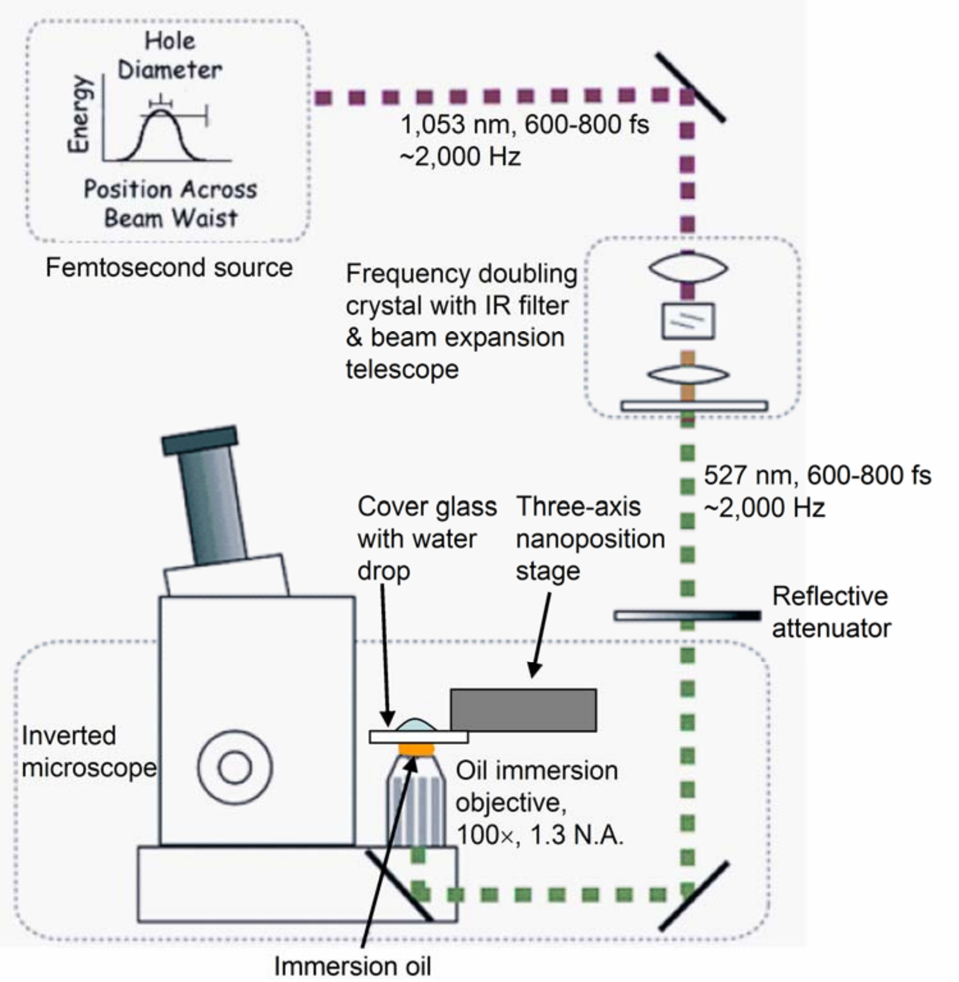

Figure 2.G.1. Experimental setup for nanomachining borosilicate cover glass with a femtosecond-pulsed laser (adapted from Joglekar *et al.* (130)).

SEM sample preparation. We coated the glass coverslides in gold (thickness ~10 nm) using a sputter coater (Structure Probe Incorporated, West Chester, PA) and imaged them with a high resolution scanning electron microscope (FEI Company NOVA 200 Nanolab, Hillsboro, OR). After imaging, we removed the gold layer using a 3:1 mixture of fuming nitric acid and concentrated hydrochloric acid.

Data acquisition. We placed the glass coverslide (narrowest part of the submicron pore facing the top liquid compartment) on a fluidic channel in poly(dimethylsiloxane) (PDMS, Sylgard 184 Silicone, Dow Corning, Midland, MI). A fresh film of PDMS with a hole in the center was placed on the top of the glass coverslide (Figure 2.2) to confine the electrolyte (recording buffer) to the top side of the cover glass. In order to guarantee reliable recording conditions while measuring relatively large currents (100-180 nA), we used Ag/AgCl pellet electrodes (Eastern Scientific, Rockville, MD). We used a patch clamp amplifier (Axopatch 200B, voltage clamp mode, applied potential of either 0.2 V (Figures 2.3, 2.F.1) or 0.15 V (Figure 2.4), analog low-pass filter set to a 100 kHz cutoff frequency), a low noise digitizer (Digidata 1322, sampling frequency set to 500 kHz), and a computer with recording software (Clampex 9.2, all from Axon Instruments, Union City, CA) for data acquisition.

Since we recorded the current at high bandwidth (~50 kHz), we took care in the analysis of the data to avoid two possible problems: amplifier saturation, and recording digitized data with low signal-to-noise ratios (SNR < 1) (148). We avoided amplifier saturation by ensuring that the currents including their high-bandwidth noise were at all times within the dynamic range of the amplifier and of the digitizer used in this work. The *maximum* recorded current with its RMS noise of ± 0.06 nA was at all times below 180 nA; the dynamic range of the recording setup was ± 200 nA. The second problem, recording digitized data with low SNRs, occurs if the amplitude of the signal of interest is considerably lower than the noise levels (148). Such low amplitude resolution can lead to inaccuracies during off-line analysis (*e.g.* event detection after filtering) (148). This condition was, however, avoided in the work presented here since the lowest signal-to-noise ratio of the high bandwidth (~50 kHz) data we recorded was 2:1 (peak amplitude:RMS noise). In addition, after filtering with a cutoff frequency of 10 kHz, we only included peak amplitudes of at least 5 times the RMS noise in the quantitative analysis of immune complexes (see below).

Data processing and event detection. For all data processing and event detection, we used Clampfit 9.2 (Axon Instruments, Union City, CA). We filtered the recorded data with a digital Gaussian low-pass filter with a cutoff frequency of 10 kHz and then decimated it to a sampling frequency of 50 kHz. We used a threshold search with two criteria to identify events (event is defined here as an immune complex or nanoparticle passing through the pore). We only counted transient reductions in current as an event if these reductions had an amplitude of at least 5 times the RMS noise of the current trace for a duration of *at least* 25 μs. These criteria established the lower limits for the algorithm that we used for analysis to distinguish events from noise; these criteria do not imply that most events lasted only for 25 μs. In fact, the vast majority of events lasted at least 100 μs. For instance, the histograms in Figure 2.G.2 show that the mean halfwidth of the smallest immune complexes was 190 ± 60 μs and the mean halfwidth of the smallest nanoparticles was 210 ± 110 μs. We therefore conclude that the sampling intervals of 20 μs used in this work were sufficiently short to resolve the events.

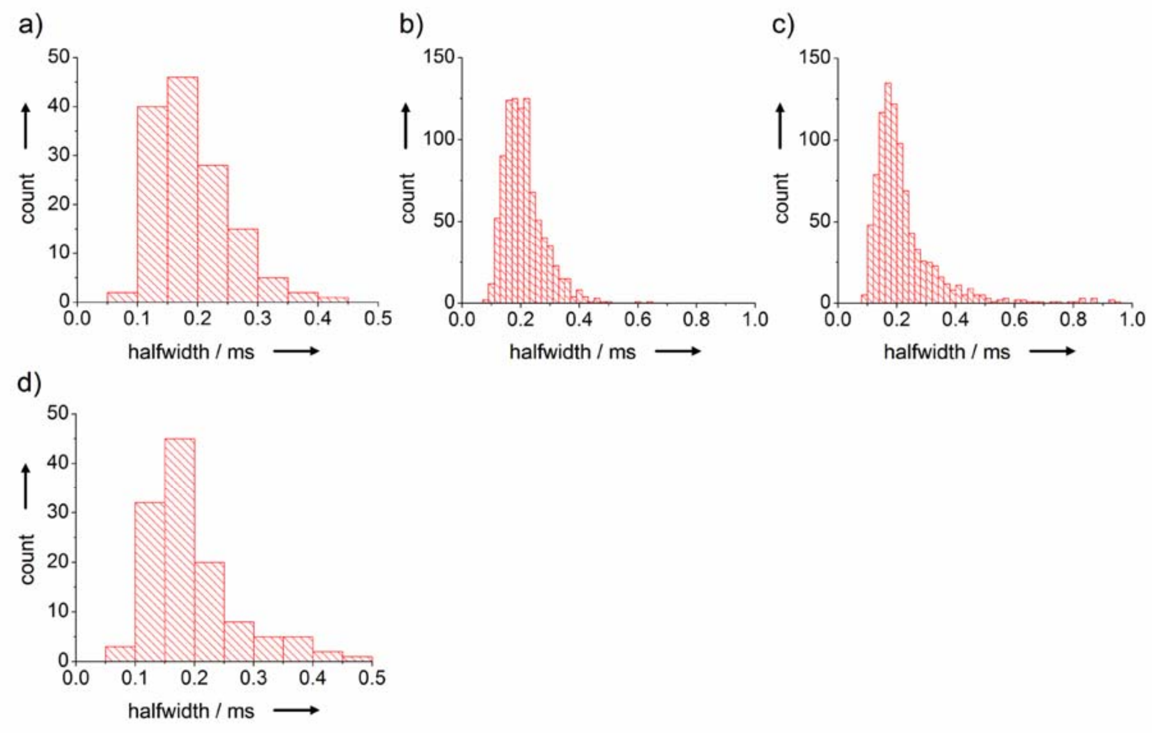

Figure 2.G.2. Histograms of the halfwidths of events caused by immune complexes and nanoparticles passing through submicron pores with conical geometry. a) Histogram of the halfwidths of some of the smallest events (mean peak amplitude = 107 ± 16 pA) that are shown in Figure 5d (recorded during the interval 4.8 – 6.9 min of the experiment). b) Histogram of halfwidths of medium-sized events (mean peak amplitude = 122 ± 40 pA) that were recorded during the interval 2.5 – 4.0 min of the experiment shown in Figure 5a. c) Histogram of the halfwidths of large events (mean peak amplitude = 380 ± 430 pA) that were recorded during the interval 8.3 – 8.6 min of the experiment shown in Figure 5a. d) Histogram of the halfwidths of events caused by the smallest nanoparticles (diameter 100 nm) moving through the pore with a diameter of 575 nm (Figure 2.C.1a).

We analyzed the collected data of events using Origin 7.5 software (OriginLab, Northampton, MA). The smallest peaks that were collected by the threshold search had a d*I*/*I* value of 0.1%. We did, however, apply a stringent requirement of a threshold of 5 times RMS for detection of events to ensure accurate assignment. Other investigators have previously reported d*I*/*I* values of 0.1% for reliable detection of DNA (113) and nanoparticles (28).

CHAPTER 3

SUBMICROMETER PORE-BASED CHARACTERIZATION AND QUANTIFICATION OF ANTIBODY-VIRUS INTERACTIONS

3.1. Introduction

This chapter describes the use of a submicrometer pore-based resistive-pulse sensor to i) detect a specific virus or a virus-specific antibody in solution, ii) probe the ability of an antibody to immunoprecipitate the virus, iii) determine the number of antibodies bound to individual virus particles, and iv) monitor the assembly of nanoparticles onto templates (here antibodies onto viruses) in situ. The assay is label-free, examines viruses in their native, assembled state, and requires no immobilization or modification of the virus or antibody. It functions by detecting the difference in the peak amplitudes of resistive pulses that occur when viruses with and without antibody bound pass through a submicrometer pore. This technique made it possible to monitor quantitatively the time-course of binding of an antibody to a non-pathogenic virus, the icosahedrical Paramecium Busaria Chlorella Virus (PBCV-1) with a diameter of ~ 190 nm (149). We found that the maximum number of antibodies that were able to bind to PBCV-1 was 4200 ± 450. Due to its small footprint and its simple detection scheme, submicrometer pore-based sensing of antibody-virus interactions may enable portable or high throughput immunoassays for diagnostics and biodefense.

The ability to determine the number of antibodies bound to a virus enables at least three important applications. First, it makes it possible to predict the efficacy of antibody-mediated neutralization of viruses (150,151). Second, the number of antibodies that are bound to a virus can be used for determining the antibody's affinity (152,153) and the valency of binding (154,155). And third, antibodies binding to a virus particle represent an accessible example of a well-defined self-assembly; monitoring this assembly process may thus be useful as a model system for studying templated self-assembly. Such a system may promote other attempts of controlled nano-assemblies (e.g. fabrication of hierarchical nanostructures by binding of nanoparticles to engineered templates – we are currently investigating this application) (1,4,5,156,157).

Currently available techniques for direct determination of the number of antibodies bound to virus particles include assays with radiolabelled antibodies (158-163), sodium dodecyl sulfate-polyacrylamide gel electrophoresis (SDS-PAGE) (164), capillary electrophoresis (CE) (165), and enzyme-linked immunosorbent assays (ELISA) (166). These techniques typically require: (i) a minimum concentration of $3 \cdot 10^9$ virus particles$\cdot$mL^{-1} (ELISA and CE typically use > $3 \cdot 10^{11}$ virus particles$\cdot$mL^{-1}), (ii) labeled antibodies, (iii) reaction volumes ranging from 10 μL (CE) to ≥ 100 μL, and (iv) in most cases, fairly bulky and sophisticated laboratory equipment with high power requirements (such as a CE apparatus, plate readers, etc).

Here we present a simple, non-destructive method for detecting virus-specific antibodies in solution and for determining the number of antibodies bound to an intact virus in a physiological buffer. This label-free technique is able to operate with virus concentrations as low as $5 \cdot 10^7$ virus particles$\cdot$mL^{-1} and establishes whether or not the antibody can aggregate (immunoprecipitate) the virus. As illustrated in Figure 3.1, the approach uses laser-fabricated pores in glass and simply measures transient changes in current, so-called resistive-pulses which are typical for Coulter counting experiments. In these experiments, the reaction volume was 40 μL, but this value could be reduced to < 10 μL via the integration of micro-fluidics (167). Due to the small size of the pores, this approach could potentially be miniaturized and performed in parallel for high throughput applications.

Previous work using submicrometer pores, nanopores and nanotubes for resistive-pulse sensing includes the detection of colloid aggregation (32,33), DNA (38,44,51,59,79,83,84,91,95-97,101,102,106,168,169), nanoparticles (24,26-28,73,109,112), proteins (61,90,92,111,114), small molecules (58,60,113), the measurement of the size and polydispersity of several viruses (29,30), as well as the analysis of the length of viral glycoproteins (spikes) (31). Sohn's group used resistive-pulse sensing to detect the binding of antibodies to synthetic colloids, which where functionalized with antigen (90,111). Here we demonstrate the use of resistive-pulse sensing for the detection, characterization, and quantification of the binding of antibodies to intact virus particles.

3.2. Recording Setup and Pore Characterization

In order to measure the resistive-pulses caused by the passage of virus particles through the pore, we used a similar setup to the one reported recently (see Appendix 3.A) (92). It consisted of a patch clamp amplifier with two Ag/AgCl electrodes and a conical pore with a diameter of 650 nm mounted in a poly(dimethylsiloxane) (PDMS) fluidic setup. The pore was fabricated in a borosilicate cover glass using a femtosecond-pulsed laser (92,129-131,133,167). We chose glass as the substrate because it is an excellent material for low-noise electrical recordings (i.e. low capacitance, low dielectric loss) (92,128,132,134), and the conical shape of the pore provided enhanced sensitivity compared to cylindrical pores (92,114). Replacement of the solutions on either side of the pore was straightforward due to the fluidic setup and the transparency of the entire assembly made it possible to observe the pore with a microscope when necessary.

Before examining the interaction of antibodies with virus particles, we characterized the response of the submicrometer pore to spherical nanoparticles of defined size and shape (see Appendix 3.A) (92). Deblois et al. demonstrated that a spherical particle passing through a cylindrical nanopore creates a resistive-pulse with a peak amplitude that was proportional to the volume of the particle (as long as the particle diameter was less than ~ 0.4 of the diameter of the pore) (24). We demonstrated recently a linear relationship for spherical particles passing through conical pores (92); the proportionality between current peak amplitude and particle volume for the conical pore was $3.9 \cdot 10^{-4}$ $pA \cdot nm^{-3}$. Virus particles are typically not perfectly spherical; however, experimental evidence suggests that the shape of particles which resemble spheroids does not influence the linear relationship between particle volume and peak amplitude (136). We made use of this linear correlation to estimate the change in the volume of PBCV-1 virus particles before and after antibody binding (Figure 3.1).

3.3. Measuring Resistive-Pulses from Individual Virus Particles

At the beginning of each experiment, we characterized the response of the submicrometer pore-based Coulter counter to single virions (see Appendix 3.B for a detailed analysis of the bandwidth of the measurement, the bandwidth and sampling frequency required resolve an event due to a virus completely, and the effects of digital filtering and decimation of data on the peak amplitudes and half-widths of the events). Even in the absence of antibodies, PBCV-1 virions passing through the conical pore created resistive-pulses with peak amplitudes significantly above the baseline noise (Figures 3.1, 3.2A). We analyzed these pulses with a computer algorithm by using a threshold value for the peak amplitude to identify individual "virus events" (the dotted red line in Figure 3.2A,B indicates the threshold value): peaks that had at least 10 times the amplitude of the standard deviation of the current noise from its mean baseline value (root mean square current noise, here called RMS noise) were counted as viruses (most events generated from a solution containing only virus had peak amplitudes of at least 700 pA, or ~ 40× the RMS current noise, Figure 3.2A). The analysis of resistive-pulses showed that the frequency of events was proportional to the concentration of the virus (29,73,112) in a concentration range from $4.4 \cdot 10^7$ – $2.5 \cdot 10^9$ virus particles·mL^{-1}; we found

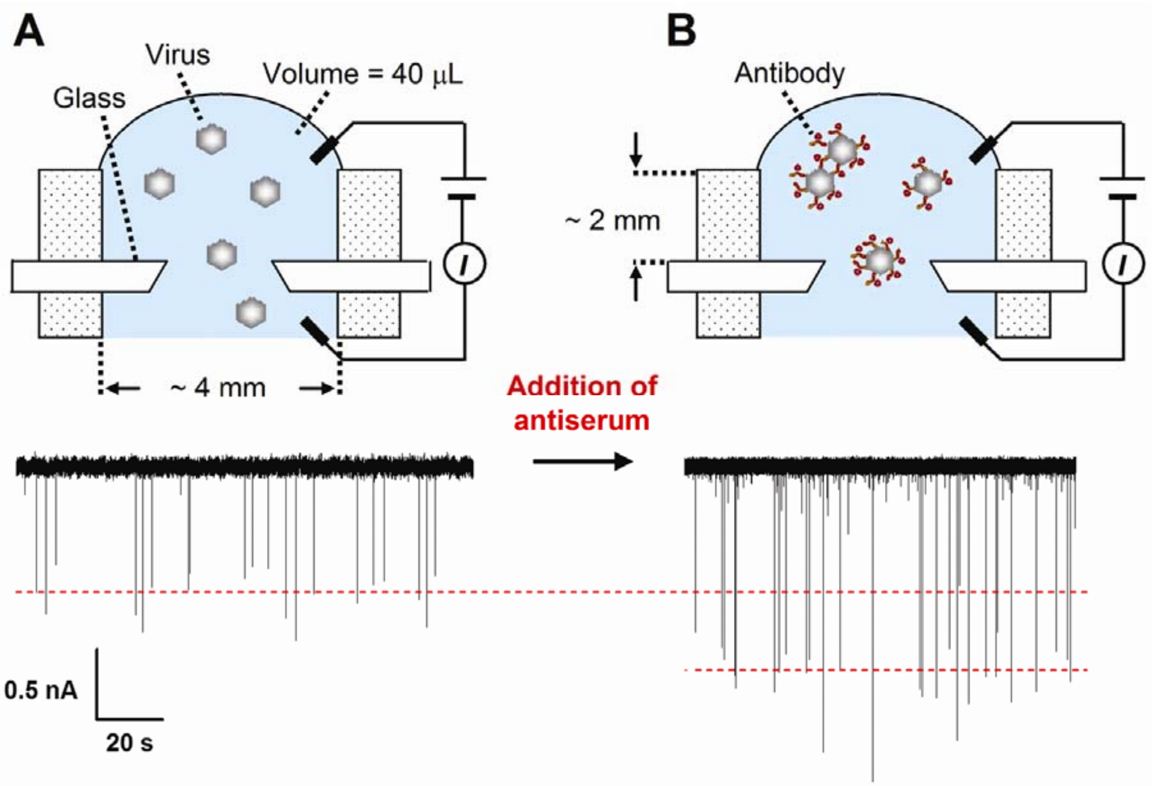

Figure 3.1. Resistive-pulse technique for detecting and characterizing the binding of antibodies to virus particles. A) Detection of virus particles before addition of antibodies. Single virions passing through the laser-fabricated, conical pore cause a transient reduction in current (resistive-pulse) as shown by the spikes (events) in the current trace. The dotted line represents the mean of a Gaussian curve fit to the distribution of the peak amplitudes of the events. The concentration of the virus was $4 \cdot 10^7$ particles·mL^{-1} and the average current passing through the pore for all experiments was ~ 140 nA. B) Detection of virus particles after addition of antibodies. Binding of antibodies to the virus increases the volume of the particle leading to an increase in the peak amplitude when the viruses pass through the pore. The current trace displays events that were recorded 10 – 15 minutes after addition of the antiserum, which was at a final dilution of 0.001× the original antiserum. If the antibody is capable of causing aggregation of viruses, this approach makes it possible to identify dimers (and larger complexes of virus particles) by detecting events with approximately twice (three times, etc) the peak amplitude of individual viruses.

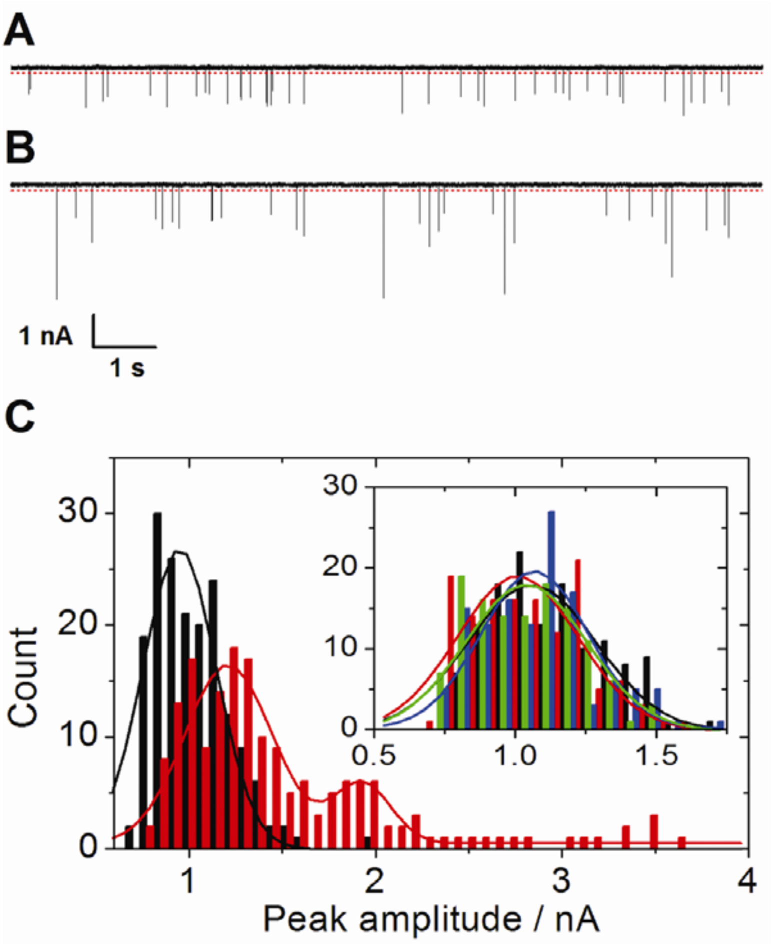

Figure 3.2. Detection of antibody-virus interaction using a submicrometer pore. A) Current versus time trace before addition of antiserum. The transient increases in resistance (events) that occurred when viruses passed through the pore lead to transient reductions in current. The dotted red line represents the threshold used to distinguish events caused by the passage of viruses from current noise. B) Current versus time trace approximately 8 min after addition of antiserum. The mean peak amplitude was approximately 22% larger than the mean peak amplitude before addition of antiserum; whereas the four largest peaks were presumably due to aggregates of virus particles. C) Histograms of the peak amplitudes of 175 events that occurred before antibody binding (black) and 6 – 8 min (red) after addition of antiserum (final virus concentration $4.4 \cdot 10^8$ virus particles$\cdot$mL^{-1}, final dilution of the antiserum: 0.001× the original antiserum). The Gaussian mean of the first (bigger) peak in the red histogram shifted compared to the histogram before antibody binding (shown in black). The second peak in the red histogram occurred presumably due to the formation of dimers. The inset represents data from control experiments: the histograms show events that occurred before (black) and 2.5 – 3.5 min (red), 7.5 – 8.5 min (blue), and 13 – 15 min (green) after addition of serum from a rabbit that was not immunized (final virus concentration $4.4 \cdot 10^8$ virus particles$\cdot$mL^{-1}, final dilution of this control serum: 0.0013× the original control serum). The change in the mean peak amplitude of the control experiments was < 6.5%.

the following relationship: frequency of events (Hz) = $4.0 \cdot 10^{-9}$ (Hz·mL·virus particles^{-1}) × concentration of virus particles (particles·mL^{-1}); N = 6; $R^2 = 0.95$ (see Appendix 3.C).

In order to estimate the size of individual virus particles without antibody bound, we analyzed approximately 1400 virus events (see Appendix 3.C). This analysis was based on fitting a Gaussian distribution to a histogram of the peak amplitudes as shown in Figure 3.2C. Applying the linear relationship between peak amplitude and particle volume to the mean peak amplitude from the Gaussian distribution then made it possible to calculate the mean volume of the virus particles. Using equations that relate the volume of an icosahedron to its diameter (170), we obtained a diameter of 203 ± 14 nm along the fivefold axes for PBCV-1 virions (see Appendix 3.C for a more detailed discussion). This result compares well with measurements of the size of PBCV-1 by cryoelectron microscopy, which revealed an average diameter of 190 nm along the fivefold axes (depending on the microscope technique, diameters of 140-190 nm have been reported (149); however, cryoelectron microscopy is known to preserve the native state of the virus (171,172) and may therefore reflect the size of the virus particles in their hydrated state more accurately than EM techniques that require drying of the samples). Coulter counting with a submicrometer pore is thus a rapid, simple, and effective technique to determine the size of virus particles in their native state (29,30).

3.4. Quantitative Monitoring of the Binding of Antibodies to Virus Particles

To examine the binding of antibodies to PBCV-1, we monitored the peak amplitude of the events after adding a polyclonal antiserum against PBCV-1; the dilution of the antiserum and therefore the concentration of antibodies in the mixture was kept constant in all experiments while the concentration of virus particles was varied (the concentration of the specific antibody in the antiserum was unknown; however, in Appendix 3.D, we calculated a lower bound of 0.55 $mg \cdot mL^{-1}$ for the concentration of the specific antibody based on the collected data). Upon addition of antiserum to solutions with various virus concentrations, the peak amplitudes of the virus events increased. A Gaussian fit of the resulting histograms showed a shift of the mean peak amplitude that indicated particles of increased volume (Figure 3.2C). The final increase in amplitude upon antibody binding onto individual virus particles ranged from + 7 to + 60% (Figure 3.3), depending on the ratio of antibody concentration to virus concentration in the solution. By calculating the difference between the mean current peak amplitudes from the Gaussian fits before and after addition of antiserum (Figure 3.2C), we were able to determine the increase in volume due to antibody binding. The maximum increase in volume occurred at the highest antibody to virus ratio and was $+ 1.4 \cdot 10^6$ nm^3, corresponding to + 60% (Figure 3.1).

Figure 3.2C also shows a second peak in the histogram of the peak amplitudes upon addition of antibody to the virus particles. The mean value of the Gaussian distribution fitted to the second peak was approximately twice that of the first peak. Since the antiserum that we used can cause aggregation of viruses (173) (see also Appendix 3.E), we suggest that the second peak was caused by dimers of viruses which were linked by the divalent polyclonal IgG antibodies in the antiserum. Control experiments with serum from a rabbit that was not immunized caused only a small

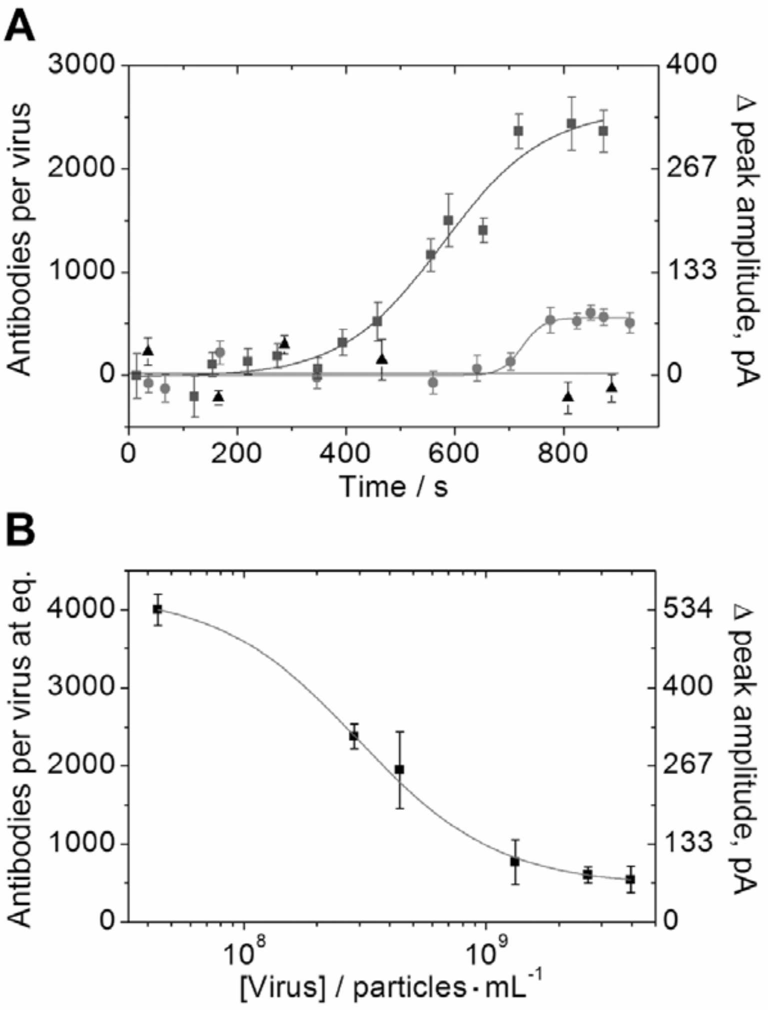

Figure 3.3. Kinetics of antibody binding at different ratios of antibody to virus concentration and estimation of the maximum number of antibodies that can bind to the virus. In all experiments, the final dilution of the antiserum or control serum was held constant and was 0.001× the original serum. A) Plot of the number of antibodies bound to virus particles versus time. The final concentration of the virus was either $2.8 \cdot 10^8$ (squares) or $4.0 \cdot 10^9$ (circles) virus particles·mL^{-1}. The triangles are from a control experiment with non-specific rabbit serum and a virus concentration of $3.4 \cdot 10^8$ virus particles·mL^{-1}. The error bars reflect the error of the mean value from a Gaussian fit to a histogram of the peak amplitudes of at least 50 events. B) Plot of the number of antibodies bound to PBCV-1 viruses at equilibrium versus the concentration of the virus (increasing virus concentration corresponds to decreasing antibody to virus ratio). The data were fitted with a sigmoidal function of the form y = A2 + (A1-A2)/(1 + (x/x0)^p) ($N = 6$, $R^2 = 0.99$). The error bars were calculated by summing the standard deviation of the mean values of the Gaussian fits to histograms of the peak amplitudes.

(< 6.5%) change of the mean of a Gaussian fit to the peak amplitudes of the virus (Figure 3.2C inset), indicating that binding of non-specific antibodies (or other proteins) to the viruses was minimal.

3.5. Determination of the Kinetics of Antibodies Binding to Virus Particles

Using the aforementioned approach to calculate the increase in volume of virus particles upon binding of antibodies, we were able to estimate the number of antibodies attached to individual virus particles by assuming that each antibody contributed a volume of 347 nm^3 (this molecular volume of IgG antibodies was measured by Atomic Force Microscopy) (141). Since the assay presented here provided the ability to record virus events continuously, it was possible to follow the number of antibodies bound to virus particles over time. We were thus able to extract the kinetics of the antibody-virus interaction at different ratios of antibody concentration to virus concentration as shown in Figure 3.3A. The equilibrium stage of antibody binding was typically reached after 6 – 13 minutes (depending on the ratio of antibody to virus). We found that the equilibrium occupancy decreased with decreasing antibody to virus ratio and that it ranged from 500 – 4000 antibodies per virus particle (Figure 3.3B).

Based on the sigmoidal fit of the data shown in Figure 3.3B, we estimate that the maximum number of antibodies that could bind to the virus particles was 4200 ± 450. Wang et al. report (173) that PBCV-1 contains a major capsid protein which carries the primary epitope to which the polyclonal antiserum binds. PBCV-1 is enclosed in 5040 copies of this major capsid protein (174). Since we observed a maximum number that was close to this number, namely 4200 ± 450 antibodies bound to each virus particle, we propose that most of these primary epitopes were accessible for antibody binding. The close agreement of these numbers also suggests that the majority of the antibodies in the antiserum were bound to an individual virus particle with one of their two binding sites (i.e. monovalent binding; purely divalent binding would result in a maximum possible antibody load of ~ 2520 per virus assuming that the major surface antigen is responsible for most antibody binding interactions). The observation that this antiserum aggregates the virus also supports the hypothesis of significant monovalent binding.

3.6. Conclusion

In conclusion, we have developed a simple technique for determining the number of antibodies bound to viruses in their native conformation. The assay is label-free, non-destructive, requires no immobilization or modification of the virus or antibody, and can establish if the antibody is suitable for immunoprecipitation. Due to the specificity of most antibody-virus interactions, this method can be used to detect the presence of an antibody directed against a particular virus in complex media such as serum (here the anti-PBCV-1 antibody); it may therefore be useful for immunoassays (175) and vaccine development. One potential drawback of this technique is that it may be challenging to detect a small number of antibodies (< 10) bound to a virus particle. While we applied this method to sense the binding of antibodies to viruses, we expect that this technology could be extended to characterize and monitor other types of nanoscale assemblies such as the assembly of nanoparticles to functional components (1,4,5,156,157).

3.6. Materials and Methods

Solutions. We prepared all solutions with deionized water (resistivity of 18.2 MΩ cm, Aqua Solutions, Jasper, GA) and we used potassium chloride, sulfuric acid (both from EMD Biosciences, La Jolla, CA), TRIS (Shelton Scientific, Shelton, CT), bovine serum albumin (Sigma, St. Louis, MO), Tween 20 (Mallinckrodt Chemicals, Phillipsburg, NJ), hydrochloric acid (VWR International, West Chester, PA), nitric acid (Fluka Chemie, Buchs, Switzerland), and hydrogen peroxide (EMD Chemicals, Gibbstown, NJ) without further purification. Recording buffer, composed of 150 mM KCl, 50 mM tris(hydroxymethyl)aminomethane (TRIS) buffer, pH 7.8, 0.1 mg·mL^{-1} bovine serum albumin, 0.1% w/v Tween 20, was filtered through sterile, low protein absorption polyethersulfone membrane filters with a pore size of 0.2 μm (Pall, East Hills, NY). Concentrated PBCV-1 virions and the polyclonal antiserum from rabbit were both kindly provided by J. L. Van Etten, University of Nebraska-Lincoln, Lincoln, NE. We diluted the virus and antiserum in recording buffer and filtered the antiserum solution through a 0.2 μm membrane filter.

Nanomachining using a femto-second pulsed laser. We described this procedure in detail previously (see Appendix 2.G) (92). Briefly, we attached a borosilicate glass coverslide (Corning 0211, Fisher Scientific, Pittsburgh, PA) to a 3-axes microscope nanomanipulation stage (Mad City Labs, Inc., Madison, WI), and placed a droplet of water on the area that was to be machined. For laser-based ablation of the glass at defined locations, we focused a directly diode-pumped Nd:glass CPA laser system

(Intralase Corp., Irvine, CA) through a 100× oil immersion microscope objective (N.A. = 1.3, Zeiss, Thornwood, NY), and used laser pulses that were frequency doubled from 1053 nm to 527 nm with a duration of 600-800 fs. We used a three stage process that employed different pulse energy and repetition rates for the shaft, top of the cone, and tip of the cone to machine the pore.

Preparation of the substrates with the pore for SEM. We coated the glass coverslide with the pore in gold (thickness ~ 10 nm) using a sputter coater (Structure Probe Incorporated, West Chester, PA) and imaged them with a high resolution scanning electron microscope (FEI Company NOVA 200 Nanolab, Hillsboro, OR).(92) After imaging, we removed the gold layer using a 3:1 mixture of fuming nitric acid and concentrated hydrochloric acid.

Mixing and data analysis. We added the diluted virus solution to the buffer in the top liquid compartment (final volume of this mixture was 40 μL). To keep the concentration of the polyclonal antibodies constant, we always added a volume of 2 μL of the diluted antiserum to this virus-buffer mixture. We then aspirated and expelled the volume in the top liquid compartment 3 times using a pipette (Eppendorf Reference, Westbury, NY) with a volume setting of 5 μL. This procedure combined with the small volume ensured that the two solutions were well mixed.

The addition of the virus to the top liquid compartment caused the RMS noise (filter cutoff frequency = 10 kHz) to change by a maximum of 15.5% (15.6 to 18.0 pA

RMS at a virus concentration of $4.4 \cdot 10^8$ particles·mL^{-1}). This change was, however, not correlated with the concentration of the virus; the maximum concentration of virus ($4 \cdot 10^9$ particles·mL^{-1}) caused a change of only 3%. The addition of the antiserum to the top liquid compartment caused the RMS noise to change by less than 4%.

During the data analysis, we usually noticed that immediately after the addition of antiserum or control serum the peak amplitude from virus particles of the events was slightly reduced (< 4.7%). We attributed this decrease in amplitude to a small change in the conductance of the solution. In order to minimize the error in our determination of the number of antibodies bound to a virus, we used the average of the Gaussian means of the peak amplitudes immediately after addition of antiserum (before significant binding of antibodies could occur) as the peak amplitude of virus particles that did not have antibodies bound on their surface.

Data acquisition and processing. Prior to each experiment, we cleaned the glass cover-slide that contained the pore in a fresh mixture of 3:1 concentrated sulfuric acid to 30% hydrogen peroxide for at least 15 minutes. The poly(dimethylsiloxane) (PDMS, Sylgard 184 Silicone, Dow Corning, Midland, MI) support that contained the bottom liquid compartment (see Appendix 3.A) was cleaned thoroughly after each experiment with alternating rinses of DI water and 95% ethanol (VWR International). We cut the PDMS film that was used for the top liquid compartment from a slab of PDMS that was cured in a clean Petri dish; we used a new PDMS film in each experiment. This procedure ensured a good seal between the PDMS and the glass, and we encountered no leaks during the experiments. We used Ag/AgCl pellet electrodes (Eastern Scientific, Rockville, MD) since the recorded currents were relatively large (~ 140 nA). We used a patch clamp amplifier (Axopatch 200B) in voltage clamp mode and set the analog low-pass filter to a cutoff frequency of 100 kHz. The setup was completed by a low noise digitizer (Digidata 1322, sampling frequency set to 500 kHz), and a computer with recording software (Clampex 9.2) for data acquisition. For all data processing and event collection, we used Clampfit 9.2 (all from Axon Instruments, Union City, CA).

We filtered the data with a digital Gaussian low-pass filter with a cutoff frequency of 10 kHz and then decimated it to a sampling frequency of 50 kHz (see Appendix 3.B for a detailed analysis of the bandwidth of the measurement, the bandwidth and sampling frequency required to resolve an event due to a virus completely, and the effects of digital filtering and decimation of data on the peak amplitudes and half-widths of the events). We defined a peak as an event that was due to passage of a virus if the signal had an amplitude of at least 13 times the standard deviation of the baseline signal from its mean for a duration of at least 25 μs and a maximum of 10 ms (all events had a halfwidth > 100 μs). We analyzed the collected data using Origin 7.5 (OriginLab, Northampton, MA) and Matlab (The MathWorks, Natick, MA).

3.7. Acknowledgements

This work was supported by an NSF career award (M.M.) and by a research grant from IMRA America and AISIN USA as well as seed funds from the College of Engineering, University of Michigan. The author thanks Daniel J. Estes, James Gurnon, and James L. Van Etten for valuable discussions.

CHAPTER 3 APPENDICES

3.A. Recording Setup and Pore Characterization

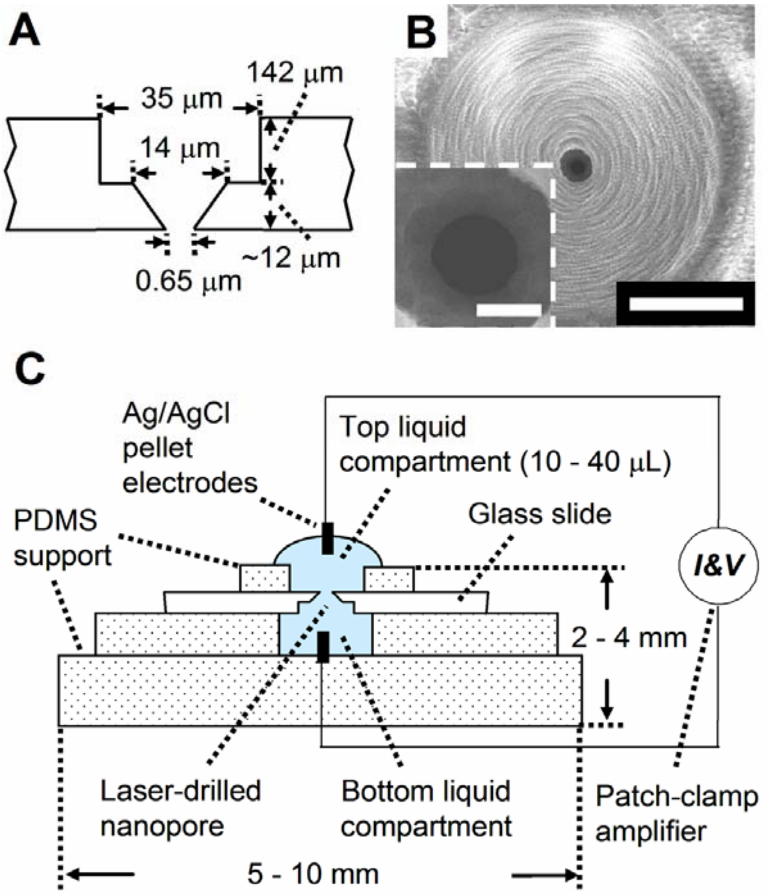

Figure 3.A.1. Schematic design of the conical pore and the recording setup used in this work. A) Geometry and dimensions of the pore used in all experiments. B) Scanning electron microscope (SEM) image looking into the 35 μm cylinder of the pore shown in A; scale bar = 5 μm. The inset shows a close-up of the narrowest part of the pore; scale bar = 500 nm. C) Sideview of the experimental setup. A patch-clamp amplifier applied a constant voltage and detected small changes in current (pA-range) with a bandwidth of ~50 kHz (the sampling frequency was 500 kHz). A poly(dimethylsiloxane) (PDMS) fluidic setup allowed for replacement of solution on either side of the pore (92). The electrode in the top liquid compartment was always polarized positively (+ 0.2 V) and virus particles were always added to this compartment.

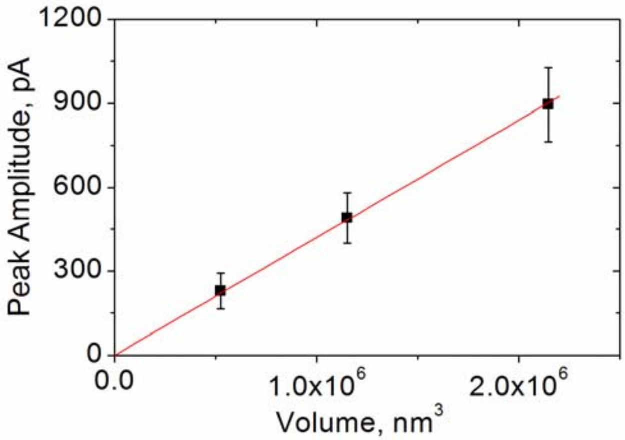

Figure 3.A.2. Plot of the average peak amplitude of the resistive-pulses caused by particles with a diameter of 100, 130, and 160 nm passing through a pore with a diameter of 575 nm versus particle volume (92). The data were fitted using a linear regression algorithm that required the line to pass through the origin; the slope of the line was $4.2 \cdot 10^{-4}$ pA nm^{-3}. We obtained a slope of $3.9 \cdot 10^{-4}$ pA nm^{-3} for the pore with a diameter of 650 nm (Figure 3.A.1A,B).

3.B. Determination of the Bandwidth Required for Accurate Extraction of Quantitative Information from Coulter Counting Analysis

Extracting quantitative data from Coulter counting experiments requires careful design of the recording system and the pore since these two entities determine the bandwidth of the measurement (92). The bandwidth is one of the most important aspects of the recorded data because it determines the time resolution. The time resolution of the measurement sets the upper bound of the "speed" at which changes in current can be recorded. That is, if a change in current occurs faster than the time resolution of the recording, then the recorded current "jumps" from one value to the next and the intervening information on how the current arrived at this value is lost. In the context of a Coulter counting experiment, the time resolution of the measurement determines the maximum resolution with which the resistive pulse of a particle can be observed while it passes though the pore. If the particle moves faster than the time resolution, then the peak amplitude of the resistive-pulse will be clipped. This clipping can cause inaccuracies in calculations that are based on the peak amplitude. Another important aspect of recording data accurately is the sampling frequency. According to the Nyquist theorem, the minimum sampling frequency required to prevent aliasing is twice the signal bandwidth (*i.e.* if the signal has a bandwidth of 10 kHz, the sampling frequency must be at least 20 kHz); however, it is typically recommended that a sampling rate at least 5 times the signal bandwidth be used (176).

The maximum possible bandwidth that is obtainable in a Coulter counting experiment is determined by the geometry of the pore, the substrate material, the conductivity of the buffer, and the recording electronics. In order to determine the bandwidth that was available during our experiments, we examined the power spectrum of a high bandwidth current trace (taken at the maximum bandwidth of the recording setup, 4-pole Bessel filter with cutoff frequency of 100 kHz and a sampling rate of 500 kHz; see black power spectrum in Figure 3.B.1A). The power spectrum contained a linear decrease in power between 4-1000 Hz and a roll-off in power after ~50 kHz. The linear drop in the range of 4-1000 Hz is most likely due to 1/*f* noise (85,177). This hypothesis is supported by the reduction in power (noise) seen in this frequency range when the applied voltage was decreased to 0 V as shown by the red power spectrum in Figure 3.B.1A (177,178). Therefore the decrease in power in the range from 4-1000 Hz is not due to a limited bandwidth of the recording setup or pore but rather to the reduction of 1/*f* noise with increasing frequency.

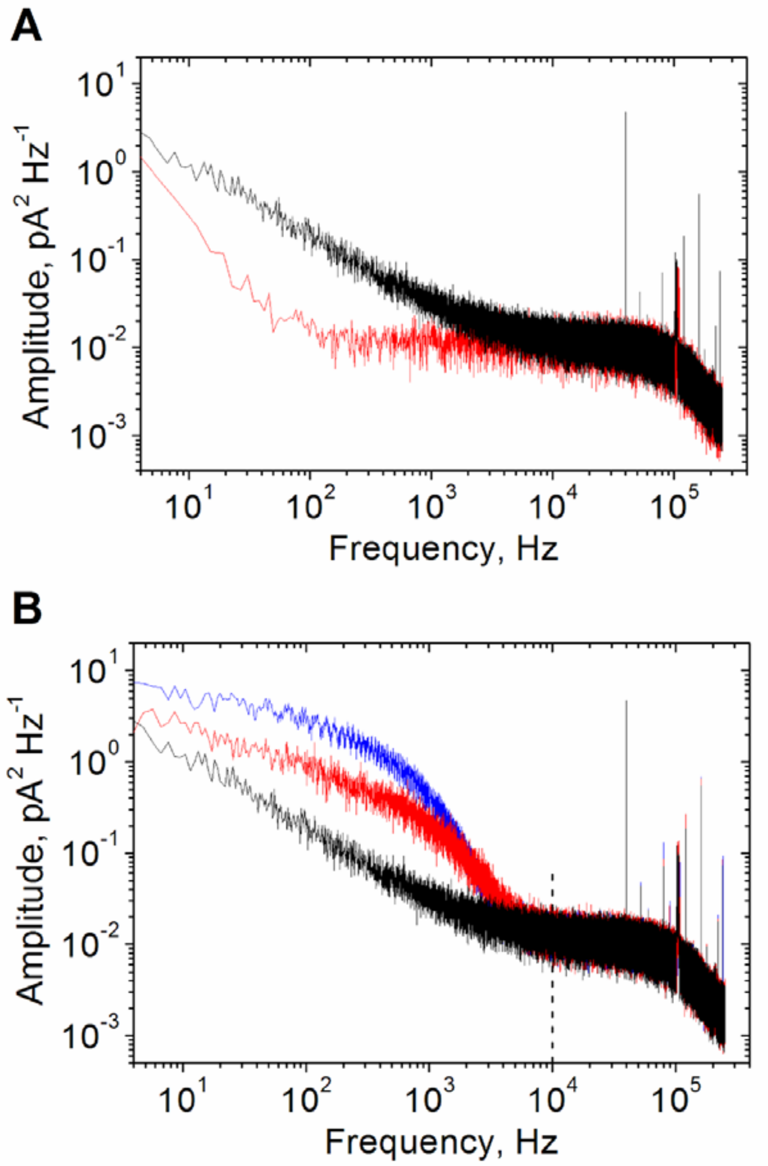

Figure 3.B.1. Determination of the bandwidth available during Coulter counting experiments and the bandwidth required to resolve events. A) Power spectra of current traces under two conditions: black – an applied voltage of 0.2 V, red – an applied voltage of 0 V. Based on these power spectra, the bandwidth of the Coulter counting apparatus (patch clamp amplifier and submicrometer pore) was ~50 kHz (see text for details). B) Power spectra of high bandwidth traces (~50 kHz; no digital filtering) without events from viruses (black), with events from viruses (red), and with events 12 minutes after addition of antiserum (blue). As illustrated by this plot, the maximum frequency component of the virus events was ≤ 8 kHz. The concentration of the virus was $2.8 \cdot 10^8$ virus particles·mL^{-1} and the antiserum was added to the top liquid compartment such that the final dilution was 0.001× the original antiserum.

The parameter that is important here, namely the reduction of bandwidth due to the recording setup can be obtained from the "roll-off" at higher frequencies. This roll-off begins at ~50 kHz and is most likely due to a combination of two factors: the bandwidth limitation of the headstage (according to Axon Instruments, the headstage operating in the configuration that we used, *i.e.* whole cell mode with $\beta = 0.1$, has a bandwidth of ~50 kHz) and the 4-pole Bessel filter that was used to prevent aliasing (cutoff frequency of 100 kHz). The analysis of the power spectra in Figure 3.B.1 therefore shows that the available bandwidth was ~ 50 kHz.

Since the pore can be modeled as a network of resistive and capacitive components, it is possible that the pore itself could limit the bandwidth; this bandwidth limitation can be estimated by the following equation (135):

$$B \leq \frac{1}{2\pi RC} \tag{3.B.1}$$

where R is the resistance leading to the pore and C is the capacitance of the substrate. Assuming a resistance of 1200 Ω (the maximum resistance leading to the pores we fabricated) and a substrate capacitance of 10 pF, the theoretical bandwidth of the recording was 13 MHz (see Chapter 5 for a more detailed discussion). Therefore, we believe that in the frequency range of interest in this work, the submicrometer pore structure was not acting as a filter and the bandwidth of the measurement was not limited by the pore but rather by the recording electronics to ~50 kHz as shown in Figure 3.B.1A.

We also used power spectrum analysis to determine the bandwidth required to resolve events due to viruses with or without antibody bound. As shown in Figure 3.B.1B, the current traces that contained events had more power in frequencies ranging from 4-8000 Hz compared to the trace that did not contain events. Therefore, a bandwidth of ~8 kHz was required to resolve the events completely. Due to this result, we were able to reduce the RMS noise of the current traces by filtering with a digital low-pass filter (Gaussian) with a cutoff frequency of 10 kHz without causing significant distortion of events: as expected, the amplitude of the virus peaks was not significantly reduced (< 5% decrease) by the 10 kHz filter when compared to the peaks that were filtered at 50 kHz as illustrated in Figure 3.B.2A,C (we also examined more than 200 events and their mean peak amplitude and the mean value of a Gaussian curve fit to the peak amplitude distribution decreased by less than 5%). Similarly, the mean half-width value of over 200 events changed by less than 8% due to the 10 kHz filter (Figure 3.B.4A,B). Figure 3.B.2E demonstrates that filtering with a cutoff frequency as low as 5 kHz would have only reduced the peak amplitude of the signal by less than 11%. Significant reduction in amplitude would have been observed, however, if we would have used a cutoff frequency of 1 kHz as shown in Figure 3.B.2F (~ 50% decrease). In the work presented here, we filtered the recorded data with a 10 kHz low-pass filter, and decimated the data to a sampling frequency of 50 kHz. As predicted by the Nyquist sampling theorem, this decimation had a minimal effect on the peak amplitude (Figure 3.B.2C,D and Figure 3.B.3 show that the decimation of data caused a negligible change in the peak amplitude of an event; the mean peak amplitude and the mean value of a Gaussian fit of over 200 events decreased by less than 1%). Decimation also had a negligible effect on the event half-width (Figure 3.B.3 and Figure 3.B.4B,C show that the decimation caused the mean half-width of over 200 events to decrease by less than 1%).

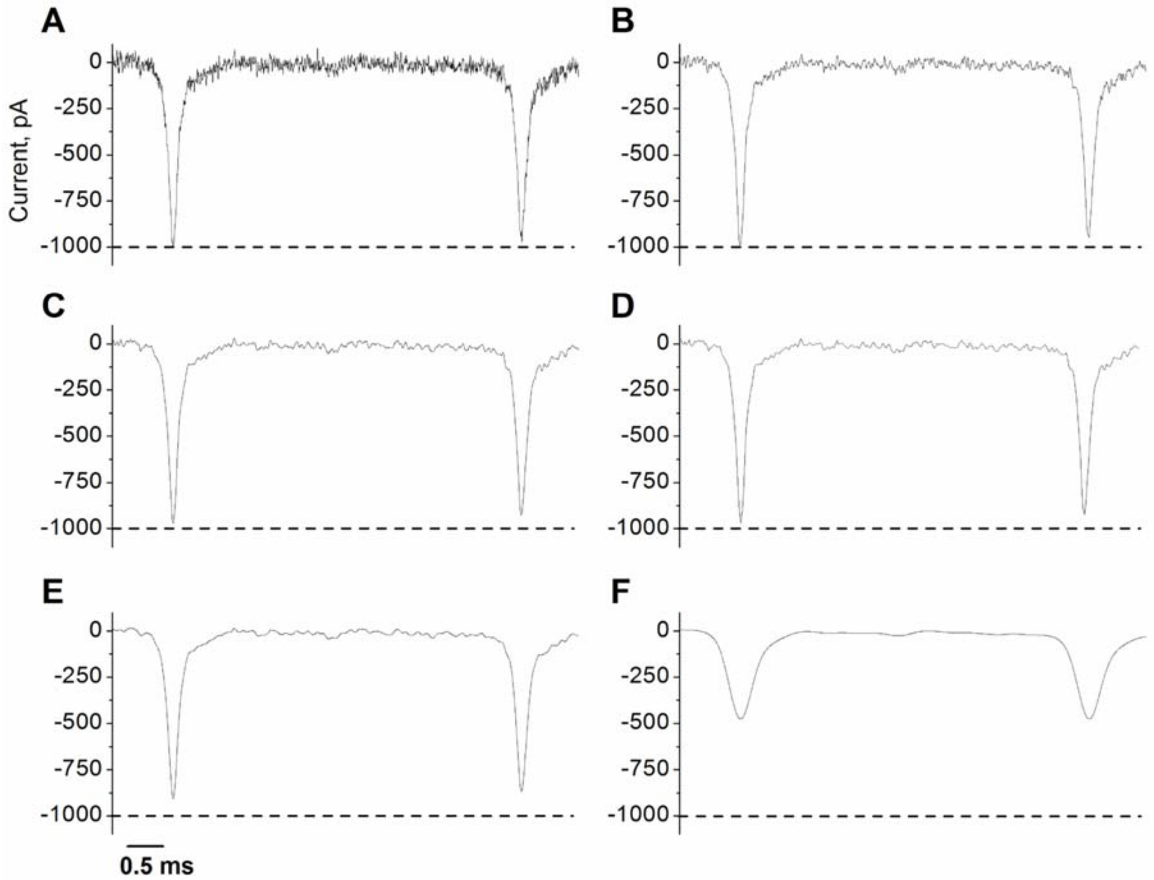

Figure 3.B.2. Effect of the cutoff frequency used for low-pass filtering on the peak amplitudes of current events during passage of viruses through a submicron pore. A) Current trace with two events after filtering with a digital (Gaussian) low-pass filter with a cutoff frequency of 50 kHz. B) Same current trace after filtering with a cutoff frequency of 20 kHz. C) Same current trace after filtering with a cutoff frequency of 10 kHz. D) Same current trace as in C but decimated to a sampling frequency of 50 kHz, instead of 500 kHz as in A-C. As predicted by the Nyquist sampling theorem, the amplitude of the signal did not change significantly (see Figure 3.B.3). E) Same current trace as in A-C after filtering with a cutoff frequency of 5 kHz. Under these conditions, the peak amplitude of the events decreased slightly since the cutoff frequency of the filter was below the maximum frequency component of the events (~8 kHz, see Figure 3.B.1B) F) Same current trace after filtering with a cutoff frequency of 1 kHz. Since the cutoff frequency of the filter was significantly below the maximum frequency component of the events, the events are distorted and the peak amplitude has decreased by a factor of approximately 0.5. The digital filters were always applied to the original, high-bandwidth current trace.

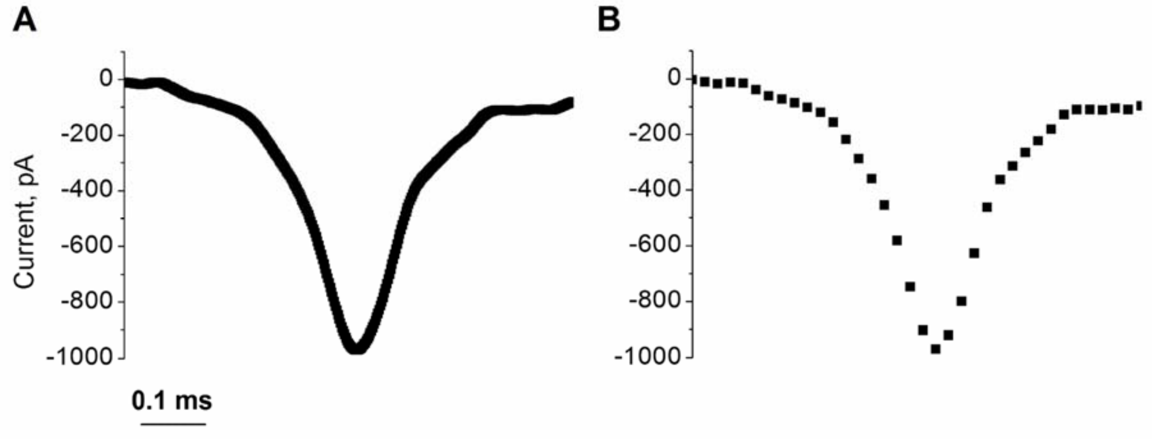

Figure 3.B.3. Close-up view of a single event due to the passage of a virus through the pore before and after decimation of data. A) Close-up view of a single event after filtering with a digital low-pass filter with a cutoff frequency of 10 kHz (sampling frequency of 500 kHz). B) Same trace as in A decimated by a factor of ten (sampling frequency of 50 kHz). The change between the peak amplitude and half-width of trace A and trace B was smaller than 1%.

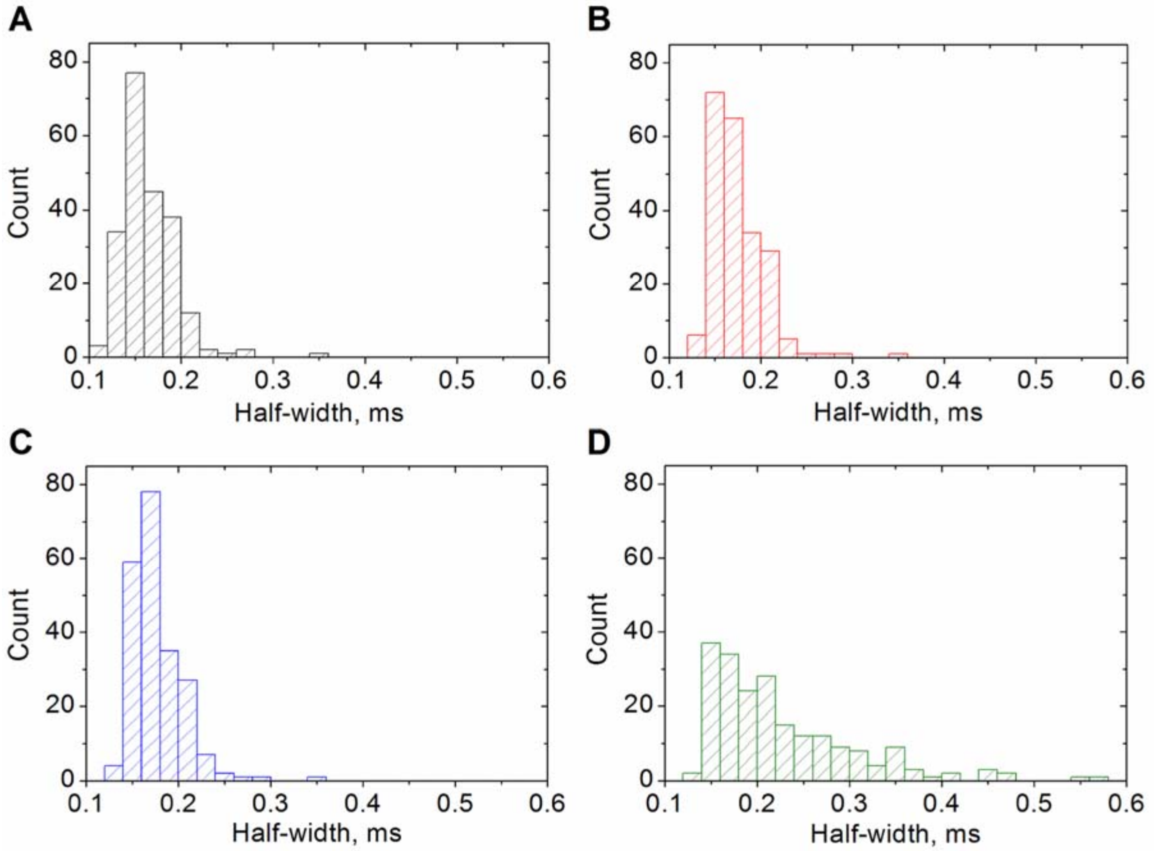

Figure 3.B.4. Histogram of the half-widths of events due to the passage of viruses at different bandwidths in the absence and presence of antiserum to demonstrate that the bandwidth and data decimation used in this work did not distort the recorded signals (*i.e.* was sufficient to resolve the entire signal). A) Half-widths of events due to the passage of viruses after filtering with a digital Gaussian low-pass filter with a cutoff frequency of 50 kHz. B) Same events as in A but filtered with a low-pass filter with a cutoff frequency of 10 kHz. C) Same events as in B but after decimation to a sampling frequency of 50 kHz. Out of all virus events collected (after digital filtering and decimation), less than 3% of events had a half-width less than 0.12 ms, and all events had a half-width greater than 0.10 ms. D). Half-widths of events collected 10.5 – 14.5 minutes after addition of antiserum (digital filter cutoff of 50 kHz, sampling frequency decimated to 50 kHz). The concentration of the virus was $2.8 \cdot 10^{8}$ virus particles·mL^{-1} and the antiserum was added to the top liquid compartment such that the final dilution was 0.001× the original antiserum.

3.C. Analysis of the Measured Diameter of PBCV-1 and Frequency of Events Versus Virus Concentration

The measured diameter of PBCV-1 reported in the main text (203 ± 14 nm) had a standard deviation (STD) of ~ 7%. Previous reports in the literature on using resistive-pulse sensing to size virus particles have resulted in STDs of ≤ 4% (29). The STD of ~ 7% reported here may be due to one of following three effects, or to a combination of these effects. First, the data used to create the histogram in Figure 3.C.1A was collected from 5 separate experiments that were conducted over seven days. Although the procedure for the experiments was always the same, there may have been small differences (*e.g.* in temperature or recording buffer) that caused an increase in the STD. Second, virus particles may have passed through the pore off center which could lead to off-axis effects that can increase the STD of a population of particles by as much as 3.5% (107). Finally, while unlikely, the STD of ~ 7% could be due the existence of structural variants of PBCV-1 (*i.e.* the population of PBCV-1 particles may have multiple distinct diameters) (30).

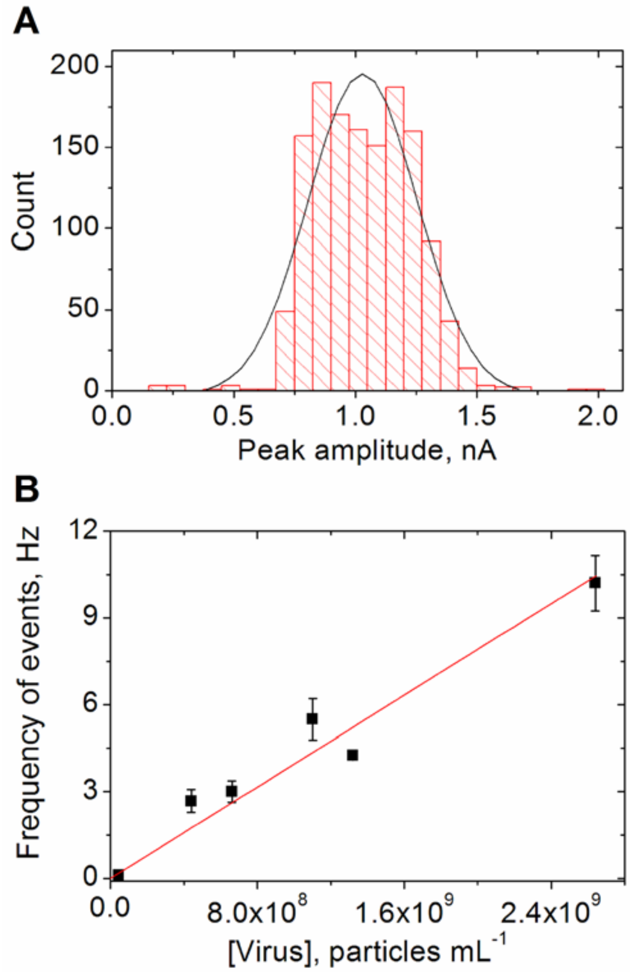

Figure 3.C.1. Histogram of the peak amplitude of resistive-pulses from single virions and frequency of viral events versus the concentration of virus particles. A) Histogram of the peak amplitudes of 1395 events caused by PBCV-1 without antibody bound passing through the pore shown in Figure 3.A.1A,B. The histogram was fit with a Gaussian distribution. B) Frequency of events versus the concentration of virus. The data points were fit using a linear regression algorithm that required the line to pass through the origin; the slope of the line was $4.0 \cdot 10^{-9}$ Hz·mL·virus particles^{-1}.

3.D. Concentration of Antibodies Specific for PBCV-1 in the Rabbit Antiserum

The concentration of specific antibody in the rabbit antiserum was unknown. We were, however, able to obtain a lower bound for the concentration of the specific antibody in the antiserum based on the number of antibodies bound per virus at equilibrium and the concentration of the virus. At the highest concentration of virus ($4 \cdot 10^9$ particles·mL^{-1}), approximately 550 antibodies were bound to each virus at equilibrium. Therefore there were *at least* $4 \cdot 10^9 \times 550 = 2.2 \cdot 10^{12}$ specific antibodies·mL^{-1} present in the diluted serum. Based on the molecular weight of an IgG antibody of 150,000 Daltons, this value corresponds to a specific antibody concentration of $5.5 \cdot 10^{-4}$ mg·mL^{-1}. Since the serum was diluted by a factor of 1000, the original serum contained at least 0.55 mg·mL^{-1} of specific and active antibody. This lower bound compares favorably to a previous study that reported an average concentration of specific antibody of 0.78 mg·mL^{-1} in rabbit antiserum (179).

3.E. Pore Blockage by Aggregates of Virus

In the experiments that involved antiserum (the antiserum dilution was held constant at 0.001× the original antiserum, the virus concentration was varied), the pore eventually blocked (> 8 min after addition of antiserum) due to the formation of large viral aggregates. No more events could be recorded after blockage (at the lowest virus concentration only partial blockage occurred). This blockage terminated the experiment, and before the next use, the pore was cleaned in a fresh mixture of 3:1 concentrated sulfuric acid to 30% hydrogen peroxide.

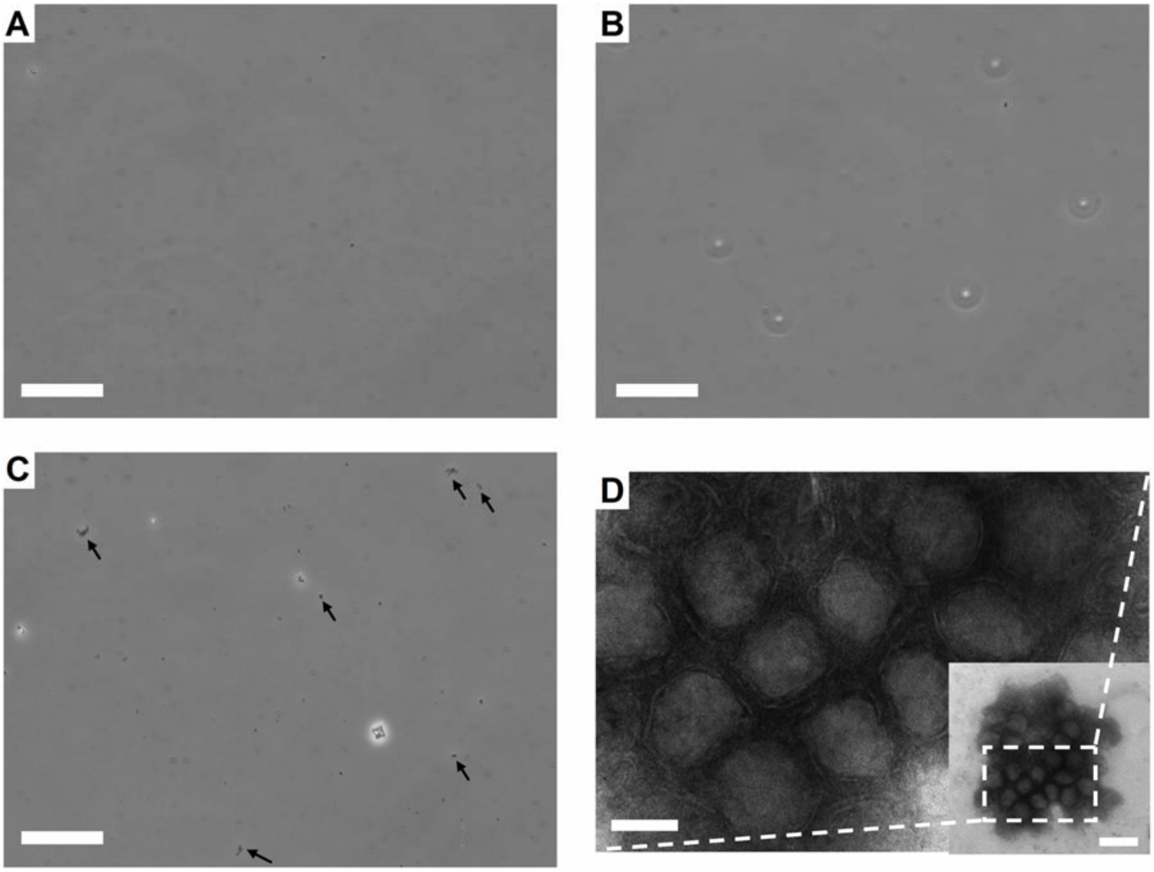

Figure 3.E.1. Microscopic observation of antiserum, control serum, and of virus antibody complexes. A) Phase contrast microscope image of the antiserum at a dilution of 0.001 in the absence of virus particles; scale bar = 75 µm. B) Phase contrast microscope image of *control* serum at a dilution of 0.001 in the presence of virus at a concentration of $6{\cdot}10^8$ virus particles·mL^{-1}; scale bar = 75 µm. C) Phase contrast microscope image of immune complexes formed by the antiserum at a dilution of 0.001 and the virus at a concentration of $6{\cdot}10^8$ virus particles·mL^{-1}. The black arrows indicate micrometer-sized viral aggregates; scale bar = 75 µm. D) Transmission electron microcopy (TEM) image of virus aggregated by antibody. The average distance between viruses in the aggregate was 23 ± 7 nm which is close to the maximum span (~ 15 nm) of an IgG molecule (see Figure 3.E.2) (154). The serum was used at a dilution of 0.001 and PBCV-1 was used at a concentration of $1{\cdot}10^9$ particles·mL^{-1}. Scale bar = 100 nm. The inset shows the entire aggregate. Scale bar of the inset = 300 nm. The buffer used for all images was composed of 150 mM KCl, 50 mM tris(hydroxymethyl)aminomethane (TRIS) buffer, pH 7.8.

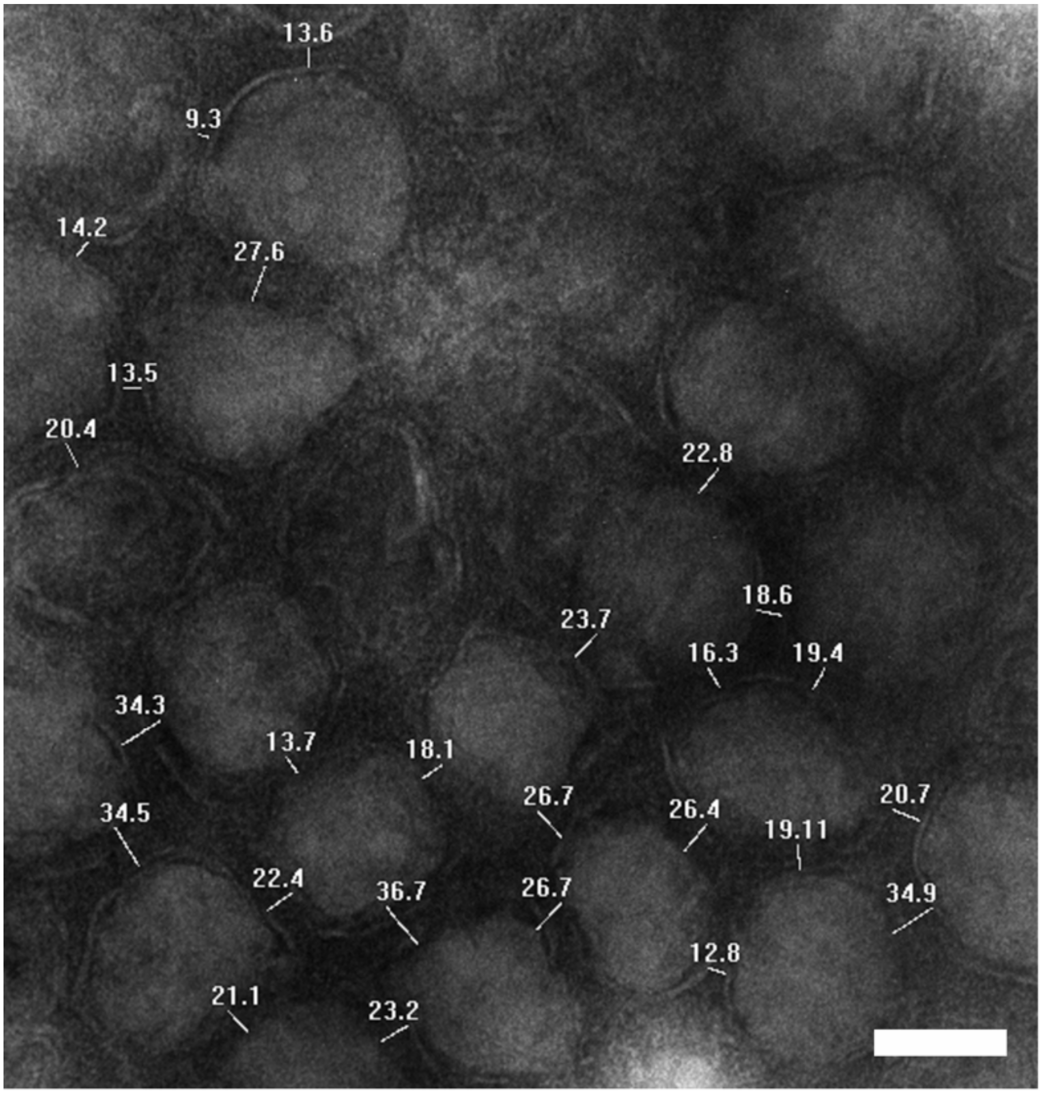

Figure 3.E.2. TEM image with individual measurements of the distance between virus particles in an aggregate. The serum was used at a dilution of 0.001 and PBCV-1 was used at a concentration of $1 \cdot 10^9$ particles·mL^{-1}. All of the measurements are in nm. Scale bar = 100 nm.

3.F. Preparation of Virus Samples for TEM.

A 300 mesh copper carbon grid (Electron Microscopy Sciences, Hatfield, PA) was placed in a glow discharge for 1 minute at 100 millitorr and 60 volts (Denton Vacuum DV-502, Moorestown, NJ) to increase the hydrophilicity of the grid. We diluted the serum 1000 fold and incubated it with the virus at a concentration of $1 \cdot 10^9$ particles$\cdot$mL^{-1} in buffer containing 150 mM KCl, 50 mM tris(hydroxymethyl)aminomethane (TRIS) buffer, pH 7.8 for 1 hour. A drop of this solution containing the virus and antiserum was placed on the hydrophilic grid and the solution was wicked away with a kimwipe paper (Kimberly-Clark, Neenah, WI). For negative staining of the antibody-virus aggregates, a drop of 1% phosphotungstic acid was placed on the grid for ~ 2 minutes and the solution was then wicked away with a kimwipe. The aggregates were imaged using a transmission electron microscope (Phillips CM100, FEI Company, Hillsboro, OR) at 60 kV.

CHAPTER 4

ESTIMATION OF SOLID PHASE AFFINITY CONSTANTS USING RESISTIVE-PULSES FROM FUNCTIONALIZED NANOPARTICLES

4.1. Introduction

Resistive-pulse sensing (Coulter counting) is a simple yet powerful method for the detection and characterization of micro- and nano-scale objects (39,41,43,92,108,180). Assays based on this technique function by monitoring the transient change in electrical resistance (resistive-pulse) when the object of interest passes through a small, electrolyte-filled pore. Resistive-pulse sensing is useful to characterize a sample of interest due to three properties: (i) the signal, *i.e.* the change in current from baseline, is proportional to the volume of the particle that created the peak (23,24,92), (ii) the number of resistive-pulses per time interval (frequency of pulses) is related to the concentration of particles (26,27,29,93), and (iii) the residence time of the particle in the pore is related to its velocity (26,27,109). The smallest particle that can be detected with a resistive-pulse sensor is determined largely by the diameter of the pore, but also by the electrical current noise, the time resolution (bandwidth) of the measurement, and the applied voltage (24,92,134). Gu *et al.* were able to detect individual molecules by exploiting the extremely small pore diameter of ion channel proteins (60).

The critical importance of the pore diameter of nano-Coulter counters has recently sparked the development of methods for obtaining membranes with single pores that have diameters significantly smaller than 1 μm (24,27,28,38,59,60,67,70,79,82-84,86,88,90,92,127). Access to these pores has lead to a rapid increase in research activity that applies resistive-pulse sensing to assays ranging from the detection or characterization of: (i) viruses (29,30,93), (ii) DNA (38,44,51,59,78,79,83,84,91,95-97,101,102,106,168), (iii) nanoparticles (24,26-28,73,92,109,112), (iv) small molecules (58-60,113,181), (v) proteins (61,90,92,93,111,114), and (vi) the aggregation of colloids (32,33). The reports on protein detection that used *fabricated* nanopores (90,92,111,114) (as opposed to nanopores based on pore-forming proteins in planar lipid bilayers (61,182)) have thus far focused on semi-quantitative data; that is they have not provided affinity constants for the antibody-antigen (or ligand-receptor) interaction. Here we demonstrate that resistive-pulse experiments can be used to estimate the solid phase affinity constant (also called avidity or functional affinity constant) (183) of an antibody for binding to its antigen.

4.2. Detection of the Binding of Antibodies to Colloids Functionalized with Antigen

Saleh *et al.* recently described a novel immunoassay that used a micropore and the resistive-pulse technique to detect the interaction of a monoclonal anti-streptavidin antibody with streptavidin-functionalized nanoparticles (90). The authors recorded the resistive-pulses during the passage of these spherical colloids with a diameter of 510 nm through the pore. A constant concentration of colloids ($1.2 \cdot 10^9$ particles mL^{-1}) was incubated with an increasing concentration of the antibody, and the resistive-pulses from the colloids with bound antibody were recorded and compared to the pulses before antibody binding. The authors calculated the diameter of the colloids at different concentrations of antibody using the following equation:

$$\left|\frac{\delta I}{I}\right| = \frac{D}{L}\left[\frac{\arcsin(d/D)}{\sqrt{1-(d/D)^2}} - \frac{d}{D}\right], \qquad (4.1)$$

where δI is the change in current from baseline, I is the baseline current flowing through the pore, D is the diameter of the pore, L is the length of the pore, and d is the diameter of the colloid. Since the change in current from baseline increased with increasing concentration of antibody, the authors concluded that the diameters of the nanoparticles increased due to antibody binding. Assuming that the antibody-antigen interaction reached *equilibrium* (Saleh *et al.* incubated the colloids with the antibody for up to thirty minutes (184), and we reported recently (93) that the binding of polyclonal antibodies to virus particles typically reached equilibrium within 13 minutes), we show that an extended analysis of Saleh *et al.*'s data makes it possible to use resistive-pulse sensing to estimate solid phase affinity constants of *e.g.* antibody-antigen interactions.

Equation 4.1 was derived by Gregg *et al.* for spherical particles by proposing that the transient increase in the resistance of the pore is due to the displacement of a volume of conducting electrolyte by the spherical particle (23,28). By using Equation 4.1, Saleh et al. assumed that binding of antibodies to the colloids created a dielectric layer of antibodies which could be treated as an increase in the diameter of the colloids. The thickness of this hypothetical confluent film (and therefore the mean increase in particle diameter) was proposed to depend on the extent of coverage of the colloids with antibodies.

We propose that the colloid diameters obtained by Saleh *et al*. from equation 4.1 can yield additional information if they are used to calculate the volume of these particles. Basing the analysis on particle volumes has the additional benefit of extending it to particles that may not be perfect spheres (92,93); experimental evidence suggests that irregularly (spheroidal) shaped particles of the same volume produce peak amplitudes of identical magnitude (136). Based on the diameters of the colloids that Saleh *et al.* reported at various antibody concentrations, we calculated the corresponding volumes of spheres with these diameters (using $V = 1/6 \cdot \pi \cdot d^3$) to obtain the volume of the colloids with and without antibodies bound. By assuming a volume of 347 nm^3 for an antibody (141), we were able to calculate the number of antibodies bound to each colloid at equilibrium, r as shown in Figure 4.1. This additional information enabled the estimation of the solid phase affinity constant of the antibody as demonstrated below.

4.3. Effect of Particle Charge on Resistive Pulses

The derivation of equation 1 did not take into account possible effects from the surface charge of the particle. Recent Coulter counting experiments with double stranded DNA (dsDNA) demonstrated that the highly charged properties of dsDNA can significantly alter the peak amplitude of the resistive-pulse (78,83,106). Depending on the ionic strength of the buffer, dsDNA even caused transient *increases* in current (conductive-pulses) when it passed through a nanopore. Several investigators proposed

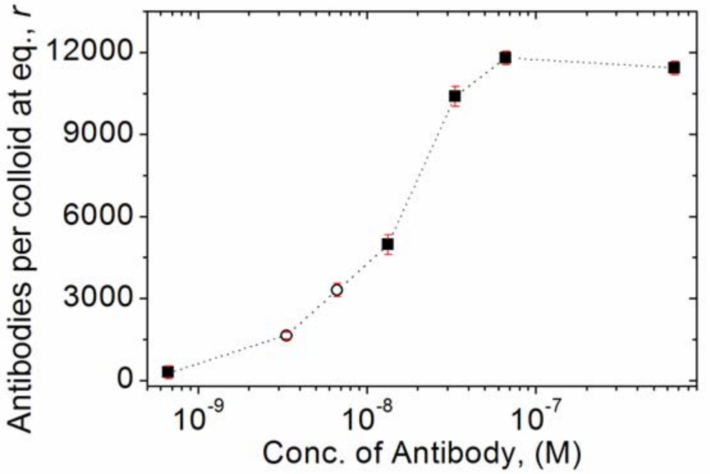

Figure 4.1. Number of monoclonal anti-streptavidin antibodies from mouse bound per streptavidin-functionalized colloid, *r*, versus the initial concentration of antibody in solution. The concentration of the colloids was held constant at $1.2 \cdot 10^9$ particles mL^{-1} (90). We created this plot by analyzing and converting the data presented by Saleh *et al* (90). See main text for an explanation concerning the two data points with open circle symbols.

that the amplitude and sign of the pulse is determined by two competing effects (78,83,106). One, the dsDNA displaced a volume of conducting electrolyte thereby removing mobile charge carriers from the electrolyte solution in the pore which caused a transient increase in resistance. Two, the dsDNA delivered a cloud of mobile counter ions into the pore due to its highly charged nature (two negative charges per base pair) which caused a transient decrease in resistance. Under certain conditions, these two effects were able to cancel each other out causing the passage of dsDNA through the pore to create no signal as demonstrated by Smeets *et al.* (106).

The effect due to the surface charge of the dsDNA depends on the length of the dsDNA and the length of the pore; if the length of the dsDNA is significantly shorter than the length of the pore, the effect of the surface charge on the amplitude of the resistive-pulses is assumed to be negligible (Smeets, R.M.M., personal communication). This hypothesis agrees with the results of Ito *et al* (27,109). These authors demonstrated that particles with nearly identical diameters of ~60 nm and different surface charge (they used particles with 120 carboxylic acid groups and particles with 24,200 carboxylic acid groups in an aqueous electrolyte with pH = 7.3, where most of these carboxylic acid groups were deprotonated and thus charged) produced resistive-pulses with nearly identical peak amplitudes in pores with lengths ≥ 0.83 μm (ratio of pore length to particle diameter of 830 nm / 60 nm = 13.8). In the experiments conducted by Saleh *et al.*, the length of the pore was 7 – 9 μm and the diameter of the colloids was 510 nm. These values constituted experimental conditions that were nearly identical to those of Ito *et al.* (ratio of pore length to particle diameter of 7000 nm / 520 nm = 13.5). Based on the experimental evidence from Ito *et al.*, we assume here that the surface charge of the antibody-colloid complex does *not* significantly affect the peak amplitude of the resistive-pulse.

Before estimating the solid phase affinity constant, the valency of the antibody-antigen interaction must be considered (185). Given that the antigen was immobilized on the colloid, the antibody could bind in a monovalent or divalent fashion (*i.e.* one or two arms of the antibody could bind to streptavidin molecules). In the following analysis, we discuss both possibilities.

4.4. Derivation of the Thermodynamics of the Antibody-Antigen Interaction

In order to estimate the solid phase affinity constant, K_a, of the antibody in the case of monovalent binding between the antibodies and the antigen at all concentration of antibody, we analyzed the binding equilibria of the antibody-antigen interaction studied by Saleh *et al*. Under these conditions, we were able to consider the colloids (with many antigen molecules covalently attached to their surface) in a fashion analogous to macromolecules that possess many identical binding sites for a single ligand. The thermodynamics of such as system are straight-forward and described in detail by G. G. Hammes (186). Following Hammes' approach, we begin the derivation by examining the simplest case, the one in which the entire macromolecule possesses only a single binding site for the ligand. This situation is equivalent to the interaction of an antibody, *Ab*, with a colloid, C_{Ag}, that would carry a single antigen (here streptavidin) molecule. This scenario can be described using the following equation (186):

$$Ab + C_{Ag} \rightleftharpoons C_{Ag}Ab. \tag{4.2}$$

The equilibrium for this reaction is characterized by K_a, the equilibrium constant, which is the solid phase affinity constant of the antibody (186):

$$K_a = \frac{[C_{Ag}Ab]}{[C_{Ag}][Ab]}, \tag{4.3}$$

where $[C_{ag}\ Ab]$ represents the concentration of the complex between the antigen-functionalized colloid and the antibody at equilibrium**,** $[C_{ag}]$ represents the concentration of free colloids at equilibrium, and $[Ab]$ represents the concentration of free antibody at equilibrium. The binding equilibria governed by equation 4.3 can be characterized by a binding isotherm of the form (186):

$$r = \frac{[C_{Ag}Ab]}{[C_{Ag}] + [C_{Ag}Ab]} = \frac{K_a[Ab]}{1 + K_a[Ab]}, \tag{4.4}$$

where *r* represents the moles of antibody bound per mole of colloid at equilibrium (or the number of antibodies bound per colloid at equilibrium). Equation 4.4 describes a single interaction and can be extended to colloids with multiple antigens (in analogy to macromolecules with multiple binding sites) by adding the isotherms for all interactions (186):

$$r = \frac{nK_a[Ab]}{1 + K_a[Ab]}, \qquad (4.5)$$

where *n* represents the number of antigens immobilized on a colloid. Provided that *r* and [*Ab*] are known or can be determined experimentally, equation 4.5 can be used to determine K_a, and *n*.

4.5. Estimation of the Solid-Phase Affinity Constant of the Antibody

The concentration of the colloids is typically known and was held constant at $1.2 \cdot 10^9$ particles mL^{-1} by Saleh et al. in all experiments. The volume-based analysis of the Coulter counting data introduced here made it possible to calculate the number of antibodies bound per colloid at equilibrium, *r*, as shown in Figure 4.1. Multiplying *r* by the concentration of colloids revealed the concentration of bound antibodies at equilibrium. The concentration of free antibody at equilibrium, [*Ab*], was then obtained by subtracting the equilibrium concentration of bound antibodies from the initial antibody concentration. During this analysis, we observed that two of the colloid diameters reported by Saleh *et al.* corresponded to bound antibody concentrations that exceeded slightly (≤ 6%) the initial antibody concentration. Since it is not possible that more antibodies bound to the colloids than were present in solution, we used the lower limit of the mean diameter of the antibody decorated colloids, which was provided by the error bars in Saleh *et al.*'s paper to calculate the number of antibodies bound and hence to obtain a plausible concentration of bound antibody. These two data points are denoted in Figure 4.1 and Figure 4.2 with open circles as opposed to filled squares, and were excluded from the generation of the best fits in Figure 4.2.

Based on the analysis derived above, we were able to create a plot of the number of antibodies bound per colloid at equilibrium, *r,* as a function of the free antibody concentration, [*Ab*] (Figure 4.2). By fitting the data with equation 4.5 ($R^2 = 0.98$, $N = 5$), we obtained the maximum number of antibodies which could bind to the colloids at saturation, *n*, and the solid phase affinity constant, K_a, for the interaction. As expected, the value of $n = 12{,}300 \pm 730$ obtained from the fit was in good agreement with the *n* (11,800) we calculated above (Figure 4.1) from the maximum volume increase as determined from resistive-pulses, and this value also matches well with the number of 9,800 streptavidin molecules immobilized on the colloid (90). Therefore, at saturation, approximately one antibody was bound perstreptavidin molecule (monovalent binding). We obtained a value of $2.6 \cdot 10^8 \pm 0.8 \cdot 10^8$ M^{-1} for K_a from this analysis, which is in agreement with the manufacturer's specifications that this monoclonal antibody has an affinity greater than $1 \cdot 10^8$ M^{-1}. Taking possible ligand depletion effects (185) into account resulted in a solid phase affinity constant of $K_a = 3.7 \cdot 10^8 \pm 1.9 \cdot 10^8$ M^{-1}.

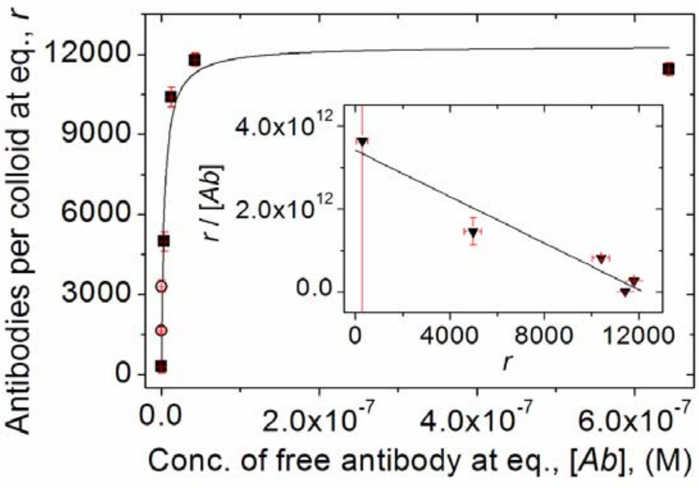

Figure 4.2. Plot of the number of antibodies bound per colloid at equilibrium, *r*, as a function of the free antibody concentration at equilibrium, [*Ab*]. Equation 4.5 was fitted to the data using nonlinear regression ($R^2 = 0.98$, $N = 5$). The two data points marked by open circles were not included in the Scatchard plot and they were not included in the best fit analysis (see main text). The inset represents a Scatchard plot of $r \cdot [Ab]^{-1}$ versus *r* (equation 4.6). Linear regression was used to fit the data ($R^2 = 0.93$, $N = 5$).

4.6. Examination of the Possibility of Bivalent Antibody Binding

In order to examine the case of bivalent binding, we plotted the data using the following linearized form of equation 4.5 (185,186):

$$\frac{r}{[Ab]} = nK_a - rK_a\,. \qquad (4.6)$$

Equation 6 is known as the Scatchard equation and the inset of Figure 4.2 shows a plot of the data in this format (this plot makes it possible to determine K_a by linear regression; we obtained $K_a = 2.8 \cdot 10^8 \pm 0.4 \cdot 10^8\ \mathrm{M}^{-1}$). Scatchard plots, as shown in Figure 4.2, are commonly used to assess the presence of divalent binding. If there was significant divalent binding, the Scatchard plot would be non-linear since at least two apparent solid phase affinity constants would determine the binding interaction (185,186). The data in

Figure 4.2, inset, follow a linear trend which implies predominantly monovalent binding across all antibody concentrations; however, the error bars in the horizontal and vertical direction combined with the recent debate on the validity of using Scatchard plots for determining the valency of binding (187,188) makes a conclusive determination of the valency of binding impossible. It is therefore conceivable that a fraction of antibodies bound divalently under conditions of low antibody concentration (*i.e.* at low occupancy of antigens by antibodies). As a consequence, the solid phase affinity constant of $2.6 \cdot 10^8 - 3.7 \cdot 10^8$ M^{-1} obtained here is most accurate for the condition of significant occupancy of antigens by antibodies.

As a final remark, it is possible that a fraction of the anti-streptavidin antibody bound to the colloids in a non-specific fashion. We calculated previously that the maximum number of antibodies bound to a colloid was 11,800, while the manufacturer specifies ~ 9,800 streptavidin molecules on the surface of the colloids. This difference suggests that as many as 17% of the antibodies may have been bound non-specifically. Assuming that the fraction of antibodies that bound non-specifically remained at a constant 17% over the range of antibody concentrations used, we re-calculated the solid phase affinity constant for the anti-streptavidin antibody using equation 4.5; the resulting solid phase affinity constant was $1.8 \cdot 10^8 \pm 0.7 \cdot 10^8$ M^{-1}.

4.7. Conclusion

In conclusion, we demonstrated that resistive-pulse sensing can be used to estimate the solid phase affinity constant for the binding of an antibody to a specific antigen (or more generally, for receptor-ligand interactions – especially when the binding interactions is predominately monovalent). The system analyzed here is analogous to antibodies binding to intact virus particles (93) or to the attachment of nanoparticles to templates (1). We recently estimated the number of polyclonal antibodies that were able to attach to native virus particles (93), and we believe that the quantitative approach outlined here will make it possible to estimate the solid phase affinity or the avidity constant of monoclonal antibodies or Fab fragments for their binding to antigens on viruses (or other epitopes that are intrinsically immobilized on nanoparticles) in physiological conformation. In addition, this method may be useful for determining the number of nanoparticles attached to a template and thus for extracting the average "association constant" of nanoparticle-template interactions. Obtaining these values for synthetic systems is difficult by established methods such as electron microscopy or atomic force microscopy. The technique presented here may thus be useful to accelerate the characterization and fabrication of the next generation of functionally assembled nanodevices (1,4,188).

4.8. Acknowledgements

This material is based upon work supported by a National Science Foundation career award (M.M., grant No. 0449088) and by a research grant from IMRA America and AISIN USA as well as seed funds from the College of Engineering, University of Michigan. The author thanks Daniel J. Estes and Ralph M. M. Smeets for valuable discussions.

CHAPTER 5

NOISE AND BANDWIDTH OF CURRENT RECORDINGS FROM SUBMICROMETER PORES AND NANOPORES

5.1. Introduction

Membranes that contain a single submicrometer pore or nanopore are attracting rapidly increasing interest from a broad community of scientists in chemistry, physics, engineering, and the life sciences (39,41,72,108,189,190). This interest partially stems from the ability of these pores to act as a highly sensitive transducer that can detect nanoparticles, individual macromolecules, and even small, single molecules in solution (39,41,72,108,189,190). In these experiments, a voltage is applied across the membrane and the ionic current flowing through the pore is monitored. Two parameters of critical importance for pore-based sensing are the signal bandwidth and the current noise (134,135,147,176). The signal bandwidth determines the accuracy with which a change in the current flowing through the pore is detected while the noise directly influences the sensitivity of a given pore. Here we present a detailed theoretical and experimental study on the signal bandwidth and the noise of current recordings from synthetic membranes that contain a single submicrometer pore or nanopore with the goal of enabling optimization and accurate prediction of these two parameters as well as providing guidelines for reliable and sensitive low-noise recordings from these pores.

Recent advances in fabricating membranes that contain a single submicrometer pore or nanopore (27,28,38,59,60,67,69-71,73-77,79,80,82-84,86-90,92,94,104,127,128,182,191-193) have generated a dramatic increase in the number of applications that use these pores for sensing (24-38, 40, 42, 44-47, 49-53, 56-66, 68, 73, 75, 78, 79, 83-85, 90-93, 95-106, 109, 111-122, 124-126, 168, 181, 182, 194-201). The largest body of work has been generated by using these pores for resistive-pulse sensing experiments. These experiments monitor the transient change in current (resistive-pulse) when an object of interest passes through the pore. Resistive-pulse sensing has been used to detect and characterize: i) synthetic polymers (36,37), ii) DNA and RNA (38,40,42,44-47,49-53,56,59,75,78,79,83,84,91,95-106,115,116,168,195-197,201), iii) nanoparticles (24-28,73,92,109,112,198), iv) viruses (29-31) and antibody-virus interactions (93), v) proteins (57,90,92,93,111,114,194,200) and unfolding of proteins (66), vi) small molecules (58-60,113,181,199), vii) ligand binding (61), viii) chemical reactions (62-65,182), and ix) the aggregation of nanoparticles (diameter > 235 nm) by cross-linking with antibodies (32-35). Additional work using current recordings from synthetic membranes with a single nanopore has included studies on the fundamental aspects of ion transport through the pore (68,117-122), on the tomography of a laser focus (124), and on the effect of surface properties of the pore on the generation of 1/f noise (85,125,126).

The signal bandwidth and the noise of the current recordings are important parameters for almost all of these applications. For resistive-pulse sensing experiments, the noise of the recordings limits the signal-to-noise ratio and hence the sensitivity of the pore because the peak of a resistive-pulse must be above the noise to be detectable (73,85). Quantitative resistive-pulse sensing experiments (*i.e.* experiments that make use of the peak amplitudes or widths of resistive-pulses) require that the signal bandwidth is sufficient to resolve fully the resistive-pulses (92,134,202) otherwise the data may be inaccurate. Ensuring a high signal bandwidth increases the information content and accuracy of the recordings which is also important for experiments that analyze the noise to obtain data on the surface properties of the pores (125,126). High signal bandwidth, however, also strongly increases the current noise, so the appropriate choice of signal bandwidth is critical. Furthermore, determining individual sources of the noise may make it possible to design the pore and the experimental setup in a fashion that minimizes the noise, and makes it possible to predict accurately the noise of a given experiment. Accurate noise prediction combined with equations that predict the peak amplitude of a resistive-pulse (22,24,25,27,28,106,168,203) would also aid in experiment design, for instance with regards to the optimal geometry and diameter of the pores for a given application or to the ideal material properties of the substrate in which the pore is fabricated.

While a significant research effort has focused on the noise and signal bandwidth of current recordings from patch-clamp experiments (132,135,147,176,178,204-207) and planar lipid bilayer experiments (134,208), we present here the first detailed study on the noise and signal bandwidth of current recordings from synthetic membranes that contain a single submicrometer pore or nanopore. We examine the signal bandwidth of each experimental element (pore, headstage-amplifier-analog filter, digitizer, and digital filter) that is used for recording, as well as the overall signal bandwidth of these recordings. We discuss the individual sources of noise that are expected to contribute to the overall noise of the recordings, and we present theoretical equations describing these noise sources. Where possible, we compare the theoretical prediction of the individual noise source with experimental results. By combining theory with experiments, we were able to predict the total noise of the recorded current traces with high accuracy when no voltage was applied. Application of a voltage generated in some, but not all cases, an extra noise component that appeared to be of a 1/f origin. Finally, we provide suggestions for minimizing the noise of current recordings, and for obtaining current recordings from resistive-pulse sensing experiments with adequate signal bandwidth to resolve fully resistive pulses.

5.2. Overall Signal Bandwidth of Current Recordings from Submicrometer Pores and Nanopores

The overall signal bandwidth of current recordings from a submicrometer pore or nanopore is one of the most important parameters of the measurement because it determines the time resolution of the data and, as described later, strongly influences the noise of the recording. The time resolution sets the upper bound of the "speed" at which changes in current can be resolved. That is, if a change in current occurs faster than the time resolution, then the recorded current will "jump" from one value to the next and the intervening information on how the current arrived at this new value is lost. In the context of resistive-pulse sensing experiments, the signal bandwidth can limit the accuracy of measurements of peak amplitude and peak width; for example, if the resistive-pulses require a larger bandwidth than what is available, then the peak amplitude of the resistive-pulses may be artificially reduced (*i.e.* the signal may be “clipped”, see Figure 5.1) or the duration of the resistive-pulse may be too short to be detected.

The overall signal bandwidth of the current recording is determined by a combination of the signal bandwidths of each individual element involved in the measurement of the ionic current. Here the individual elements are the submicrometer pore or nanopore, the headstage (*i.e.* the part of the amplifier that performs the initial amplification, placed as close as possible to signal of interest) and amplifier, the analog low-pass filter (which prevents aliasing (176) and reduces noise), the digitizer, and, if used, the digital filter. The overall signal bandwidth will always be smaller or equal to the lowest signal bandwidth available from each individual element, and determining an exact value for each element can be difficult (it is possible to group certain elements and measure the signal bandwidth of this group). In general, if the signal bandwidth of an element is approximately three times greater than the lowest signal bandwidth, its contribution to the overall signal bandwidth of the recordings is negligible (202). In the following sections, we examine the signal bandwidth of each of the aforementioned elements (or a grouping of these elements) as well the overall signal bandwidth of the current recordings.

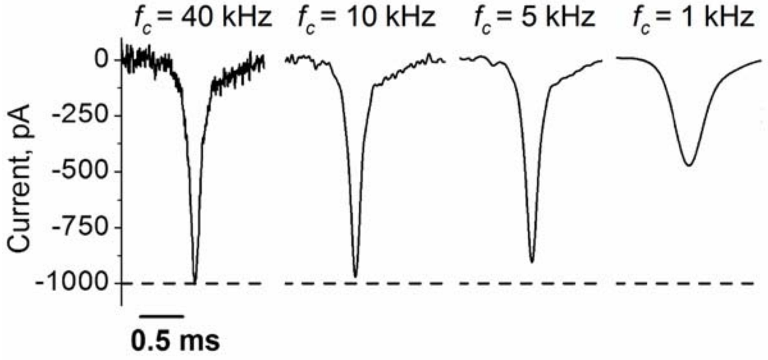

Figure 5.1. Comparison of a single resistive-pulse from a virus particle at four different signal bandwidths, including 40, 10, 5, and 1 kHz. Since complete resolution of the resistive-pulse required a signal bandwidth of at least 10 kHz (see Figure 5.10) (93), the shape of the resistive-pulse is modified significantly at signal bandwidths less than this value.

Before beginning this analysis, we would like to clarify the meaning of the term signal bandwidth. When measuring signals in the presence of noise, two distinct bandwidths should be considered (209), the signal bandwidth and the noise bandwidth. Usually, the signal bandwidth is more important than the noise bandwidth since it determines the time resolution of the recordings. The noise bandwidth is only required for an accurate prediction of the root-mean square (RMS) noise from theoretical equations and can be derived from the signal bandwidth as discussed below in the section *Theoretical calculations of the RMS current noise from power spectral densities*.

The signal bandwidth of systems that attenuate all frequency content above a specific frequency (*e.g.* a system that contains a low-pass filter) is typically defined as the frequency at which the signal (including its noise) has been attenuated by -3 dB (*i.e.* the signal bandwidth is the frequency at which the power of the signal and noise output from the system has been attenuated by 50% compared to the power of the signal and noise input to the system). Since the frequency at which a low-pass filter attenuates the input signal by -3 dB is commonly defined as the cutoff frequency f_c of the filter (a definition we also used in this work), the terms signal bandwidth and cutoff frequency are often used interchangeably along with the terms -3 dB bandwidth and bandwidth. Here we will use the terms signal bandwidth and cutoff frequency synonymously in the text and f_c in the equations.

Signal bandwidth of the pore:

Submicrometer pores and nanopores are typically fabricated in dielectric materials such as glass, silicon dioxide, silicon nitride, and polymers. The use of such materials as substrates makes it possible to model the pore as a network of resistive and capacitive components. Consequently it is possible that the pore structure itself could limit the signal bandwidth of the measurement (135,176,205). In the simple case of a cylindrical pore spanning a membrane (as in the PET pores we used, see Figure 5.2B), the signal bandwidth of the pore can be estimated using the following equation (135,205):

$$f_c \leq \frac{1}{2\pi RC}, \tag{5.1}$$

where f_c (Hz) is the cutoff frequency (*i.e.* signal bandwidth), C (F) is the capacitance of the membrane that supports the pore, and R (Ω) is the total resistance leading to and from the membrane in which the pore is fabricated. Note, in this model circuit for a pore in an electrolyte, R is not the resistance of the pore itself; R is only the resistance that arises in series with the capacitance of the chip (i.e. only the resistance to and from the pore is considered in this approach).

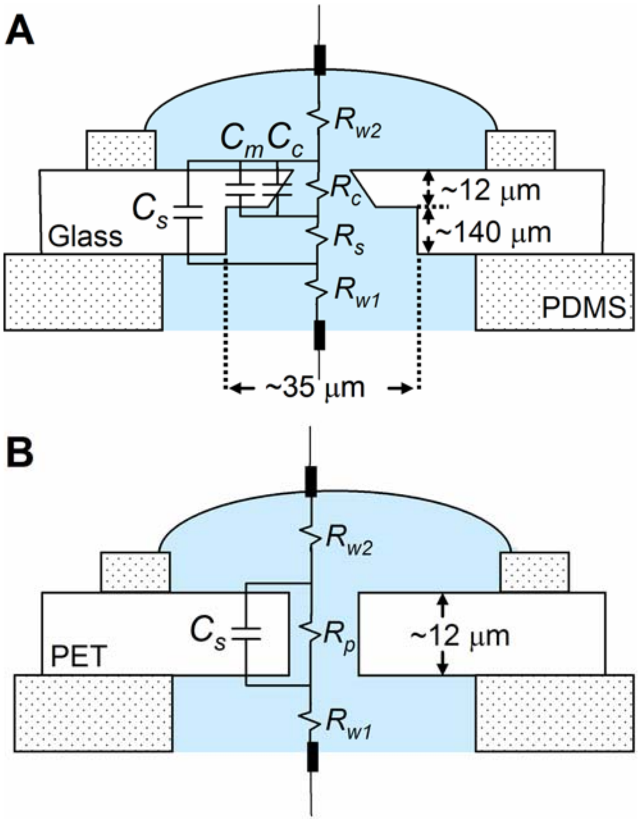

Figure 5.2. Model circuits of the pores used in this work. A) Model circuit of the glass pores with conical geometry. R_{w1} and R_{w2} are the resistance of the fluidic channels leading to the glass substrate, R_s is the resistance of the 35 µm wide cylindrical shank, C_s is the capacitance of the substrate supporting the glass membrane with the pore, R_c is the total resistance of the conical part of the pore structure, C_c is the total capacitance of the conical part of the pore structure, and C_m is the capacitance of the glass membrane in which the pore was fabricated. B) Model circuit of the PET pores with cylindrical geometry. R_p is the resistance of the pore. The model circuits shown above do not include the resistance or capacitance of the electrodes since these parameters are not expected to affect significantly the signal bandwidth of the pore. In the models shown in A) and B), we considered the convergence resistance (210) to and from the pore as a part of the resistance of the pore (*i.e.*, R_p and R_c include the convergence resistance).

In the experiments performed here, we used glass pores with conical geometry as shown in Figure 5.2A as well as polyethylene terephthalate (PET) pores with cylindrical geometry as shown in Figure 5.2B. For the glass pores with conical geometry, Eq. 5.1 is not directly applicable; however, it may be used to provide an estimate of the signal bandwidth for these pores by using the lower value of the bandwidth calculated with the following two sets of parameters (see Figure 5.2 for definitions of parameters): 1) $C = C_s$ and $R = R_{w1} + R_{w2}$ and 2) $C = C_m + C_c$ and $R = R_{w1} + R_{w2} + R_s$. In the fluidic setup we used with the recording buffer of lowest conductivity, R_{w1} was approximately 100 Ω, R_{w2} was approximately 1100 Ω, R_s was approximately 80 kΩ, C_s was approximately 10 pF, C_m was approximately 5 fF, and C_c was approximately 2 fF. Examining the two parameter sets resulted in a signal bandwidth of 13 MHz for parameter set 1 or of 280 MHz for parameter set 2. Taking the lower value thus predicts that the signal bandwidth of the glass pores with conical geometry is ~13 MHz (211). For the PET pores, R_{w1} was approximately 20 Ω, R_{w2} was approximately 300 Ω and C_s was approximately 30 pF. Using Eq. 5.1, these values result in an estimated signal bandwidth of 16 MHz for the PET pores.

In summary, we estimate that the signal bandwidth of the pore structures we used here was in the low MHz range, which is significantly greater than the signal bandwidth of the recording electronics we used (~ 52 kHz, see below). It is important to realize that for the cylindrical pores used here, the resistance of the pore R_p did not affect the signal bandwidth since it was not *in series* with a significant capacitance. In the case of conical pores, the equivalent model circuit was complicated but based on the estimate performed here (211), we suggest that the bandwidth of the conical pores used in this work was at least 13 MHz. In general, as long as the pore structures do not generate a large resistance *in series* with a large capacitance (*i.e.* as long as the product of $R \times C$ is smaller than approximately $1 \cdot 10^{-6}$ Ω F), the signal bandwidth will not be limited by the pore structure itself but rather by the recording electronics as discussed in the following paragraphs.

Signal bandwidth of the headstage, amplifier, analog low-pass filter, and digitizer:

The manufacturer of the headstage and amplifier used here does not specify the signal bandwidth of these individual elements. Instead, the headstage (H), the amplifier (A), and an analog low-pass Bessel filter (F) are grouped together and the maximum signal bandwidth of this HAF group is specified in the form of a no load (no external components such as electrodes attached to the headstage) 10 – 90% risetime. Here, the 10 – 90% risetime $t_{10\text{-}90}$ (s) of a system is the time that it takes for the output of the system to go from 10% of its final value to 90% of its final value when a step function is the input. This value can be used to estimate the signal bandwidth of the HAF combination by using the following relationship (202,212):

$$t_{10-90} \approx \frac{0.34}{f_c}\,. \tag{5.2}$$

In the work presented here, we used two of the three amplification modes available in the Axopatch 200B amplifier: a headstage amplification of $\beta = 0.1$ and of $\beta = 1.0$. For $\beta = 0.1$, the feedback resistor in the headstage of the amplifier R_f equals 50 MΩ and the amplifier is able to pass a maximum current of 200 nA. For $\beta = 1.0$, R_f equals 500 MΩ and the amplifier is able to pass a maximum current of 20 nA. The third mode of this amplifier uses a feedback capacitor instead of a resistor to decrease the noise; however, due to the relatively large currents recorded in most pore-based sensing experiments (hundreds of picoamps to nanoamps), this capacitive feedback mode is often not practical due to the large number of resets required to discharge the feedback capacitor. The manufacturer of the amplifier specifies that the two modes of headstage amplification $\beta = 0.1$ and $\beta = 1.0$ have a $t_{10\text{-}90}$ risetime of 6 μs when an analog low-pass Bessel Filter with eight poles and a cutoff frequency of 100 kHz is used and no load is applied to the input. This risetime corresponds to a signal bandwidth (Eq. 5.2) of 57 kHz ($0.34 / 6 \cdot 10^{-6}$ s = 56.6 kHz). The manufacturer states that this signal bandwidth is lower than expected for a low-pass Bessel filter with a cutoff frequency of 100 kHz due to the signal bandwidth limitation of the electronics in the headstage of the amplifier (for a discussion of the electronic components used in a patch-clamp amplifier, see references (204,205)).

Since the signal bandwidth of the HAF combination is a very important parameter, we used an experimental technique to measure it (205,213). For this measurement, we added the digitizer (D) to the grouping (HAFD) to test its effect on the signal bandwidth of the current trace (since the digitizer has a signal bandwidth larger than 250 kHz, no effect was expected). Adding the digitizer also made it possible to record the data. Using the built in low-pass Bessel filter with four poles set to a cutoff frequency of 100 kHz and a square wave that was capacitively coupled into the amplifier (see Experimental Section), we measured a no load $t_{10\text{-}90}$ risetime of 6.3 ± 0.8 μs corresponding to a signal bandwidth of 54 ± 6 kHz for $\beta = 0.1$ and a $t_{10\text{-}90}$ risetime of 6.5 ± 0.7 μs corresponding to a signal bandwidth of 52 ± 5 kHz for $\beta = 1$. When we loaded the system with glass or PET pores with various resistances (0.2 MΩ to 4.3 GΩ), the $t_{10\text{-}90}$ risetime of either mode changed by less than 3.2%. In summary, the signal bandwidth of the HAFD combination was close to the value specified by the manufacturer for the HAF combination, and the signal bandwidth of the HAFD combination was minimally affected when loaded with electrodes and pores of either substrate material.

Overall signal bandwidth of current recordings before and after application of a digital filter:

Since the signal bandwidth of the pores that we used was significantly greater than the signal bandwidth of the HAFD combination, the overall signal bandwidth of the current recordings was set by the HAFD combination to ~ 52 kHz (214). After digitizing original current traces, it is common practice to filter these recordings with low-pass digital filters to reduce the noise by reducing the signal bandwidth of the sources of noise. What then is the effect of digital filtering on the overall signal bandwidth? The answer can be complicated depending on the type of filter used and depending on the cutoff frequency of the filter compared to the overall signal bandwidth of the originally recorded current trace (215). For the experiments presented in this work, the solution was straightforward since the signal bandwidth of the pore was significantly greater than the signal bandwidth of the HAFD combination, and since we only used analog Bessel filters and digital Gaussian filters (216). In this case of similar types of filters, the overall signal bandwidth can be estimated using the following equation (202):

$$f_c = \sqrt{\frac{1}{\frac{1}{f_{c1}^2} + \frac{1}{f_{c2}^2}}}, \qquad (5.3)$$

where f_{c1} is the signal bandwidth of the HAFD combination (here ~ 52 kHz) and f_{c2} is the cutoff frequency of the digital filter. In addition to using Eq. 5.3, the overall signal bandwidth of the digitally filtered recordings can be determined experimentally by measuring the $t_{10\text{-}90}$ risetime of a digitally filtered square wave that was coupled in capacitively. For all discussions of current noise below, we used the experimentally determined signal bandwidth.

In summary, the overall signal bandwidth of the current trace was limited by the HAFD combination to ~ 52 kHz since the estimated signal bandwidth of the pore structures we used was large (low MHz range). We expect the same result for most pore structures of other investigators as long as the product of $R \times C$ is smaller than approximately $1 \cdot 10^{-6}\ \Omega$ F. While it can be difficult to determine an exact overall signal bandwidth, there are two key ideas which help to estimate the overall signal bandwidth: 1) the overall signal bandwidth will always be less than or equal to the lowest signal bandwidth of any element (pore, HAFD, digital filter) involved in the recording and 2) if the signal bandwidth of an element is significantly greater than the lowest signal bandwidth of an element (i.e. by a factor of approximately three), its contribution to the overall signal bandwidth of the recordings can be ignored (202).

5.3. Noise of Current Recordings from Submicrometer Pores and Nanopores

The noise of the current recording is a critical parameter for resistive-pulse sensing experiments since it limits the signal-to-noise ratio and hence the sensitivity of a pore (73,85), and in some cases it enables fundamental studies on the surface properties of the pores (125,126). A careful examination of the pore and the electrical components involved in current recordings permits a determination of the individual sources and magnitudes of noise that contribute to the overall noise. With this information, it may be possible to minimize the amount of noise through knowledge-based design of the experimental parameters, the pore structures, and the recording electronics (see below). Knowing the sources of noise may also enable an accurate prediction of the noise from a given pore; combining this prediction with theoretical equations that predict the peak amplitude of a resistive-pulse for a given particle (22,24,25,27,28,106,168,203) enables the simulation of resistive-pulse sensing experiments without the need for experimental work (assuming the bandwidth is adequate to resolve fully the resistive-pulses). Finally, a detailed understanding of the noise can be helpful in studies that examine "extra" noise that may appear due to specific properties of a given pore (125,126).

There are several well-established methods for describing the noise of current recordings. The most generally used technique is to calculate a single value that can be directly related to the noise measured in the current trace (176). Two examples of such single values are: 1) peak-to-peak (p-p) noise, which is calculated by measuring the change in the current from peaks in the noise trace above the mean value of the noise to peaks below the mean value, and 2) root-mean-square (RMS) noise, which is the standard deviation of the noise from its mean value (176). In order to obtain detailed information about the noise, it is common practice to calculate its power spectral density (also known as power spectrum). The power spectral density of the noise provides information on the distribution of the power of the noise (which can be thought of as the strength of the noise signal) as a function of frequency. This information can be useful for determining the origin of the noise (147,176). In this work, we describe the theoretical and experimental noise of the current traces based on RMS values and power spectral densities. We chose to use RMS noise values because p-p noise values are somewhat ambiguous (there are no strict definitions on which peaks to choose), and RMS noise values can be calculated easily from power spectral densities (described below) or from original current traces.

In the following sections, we examine in detail the theoretical noise from each component involved in recording the ionic current flowing through a synthetic pore. We describe the origin of each noise source and provide equations for calculating theoretical power spectral densities and RMS values of the noise of each source; these equations represent the minimum amount of noise that can be expected from the individual sources of noise. Where possible, we compare the theoretical value of the individual source with an experimentally measured value, and we use this comparison to predict accurately the noise that is experimentally observed in current traces from glass and PET pores. Finally, we examine the "extra" noise that is observed in some of the pores under an applied voltage and conclude that the extra noise may be of a 1/f origin (85,125,126).

Theoretical calculations of the RMS current noise from power spectral densities:

Before beginning a detailed analysis of the noise, we will briefly discuss a detail that enables a more accurate calculation of the predicted RMS noise from the theoretical power spectral densities. Equations that provide RMS values of the noise are derived by integrating the power spectral densities of the noise with respect to frequency f from 0 to the cutoff frequency of the filter (see Eqs. 5.4 and 5.5). This approach assumes that the noise from a given source is completely attenuated above the cutoff frequency that is used in the calculation; however, the filters (digital or analog) commonly used in recording the ionic currents from the pores do not completely attenuate signals above their given cutoff frequency (*i.e.* the gain of the filter is not equal to 0 above the cutoff frequency of the filter) (147) which can lead to an appreciable amount of noise power above the cutoff frequency of the filter.

This additional noise can be taken into account by using the noise bandwidth of the filter in place of the signal bandwidth in theoretical calculations of RMS noise. The noise bandwidth is calculated by multiplying the signal bandwidth of the filter with coefficients that are determined by the type of filter and by the frequency dependence of the power spectral density (147). For a low-pass Bessel filter with eight poles, the correction coefficients are: $c_1 = 1.04$ for a noise source with a power spectral density that has no dependence on frequency; $c_2 = 1.3$ for a noise source with a power spectral density that grows linearly as a function of f; and $c_3 = 1.9$ for a noise source with a power spectral density that grows as a function of f^2 (147). Since we could not find the precise coefficients for a four pole low-pass Bessel filter or a low-pass Gaussian filter (as used in this work), we used coefficients c_1, c_2, and c_3 as the best available approximation for all theoretical RMS calculations performed in this report (except for quantization noise that was not filtered by a digital filter (176)).

Theoretical noise generated by the headstage and amplifier:

In nearly all current recordings from submicrometer pores or nanopores, the recording electronics convert the measured current into a voltage signal by using a current-to-voltage (I-V) converter. This I-V converter generates the majority of the noise that is added to the current signal in the headstage and amplifier (205). The power spectral density of the noise of an I-V converter $S_A^2(f)$ (A^2 Hz^{-1}) is given by Eq. 5.4 and the RMS noise of an I-V converter $I_A(f_c)$ (A RMS) is given by Eq. 5.5 (176):

$$S_A^2(f) = 2qI_{fet} + \frac{4akT_h}{R_f} + e_n^2\left(\frac{1}{R_f^2} + 4\pi^2 C_t^2 f^2\right), \tag{5.4}$$

$$I_A(f_c) = \sqrt{2qI_{fet}c_1 f_c + \frac{4akT_h c_1 f_c}{R_f} + e_n^2\left(\frac{c_1 f_c}{R_f^2} + \frac{4}{3}\pi^2 C_t^2 c_3 f_c^3\right)}, \tag{5.5}$$

where q (C) is the elementary charge of an electron, $1.6 \cdot 10^{-19}$ C, I_{fet} (A) is the gate leakage current of the input field effect transistor (FET), a (unitless) is a constant factor that represents excess noise (176), T_h (K) is the temperature of the feedback resistor, R_f (Ω) is the resistance of the feedback resistor, e_n (V $Hz^{-1/2}$) is the input voltage noise of the input FET of the I-V converter, and C_t (F) is the total capacitance that interacts with the input of the headstage.

The first term in the power spectral density (Eq. 5.4) $2qI_{fet}$ represents the shot noise generated by the gate leakage current of the input FET of the I-V converter. The input FETs used for patch-clamp amplifiers like the Axopatch 200 series are designed to exhibit low shot noise and have I_{fet} values of ~ 0.2 pA (176), which is the value that we used in our calculations. The second term $\frac{4akT}{R_f}$ represents the thermal noise generated by the feedback resistor. As stated above, the constant a is used to account for excess noise that may be present in the feedback resistor (176). The headstage of the patch-clamp amplifier we used was cooled so that $T_h \approx 258$ K, and R_f was either 50 MΩ ($\beta = 0.1$) or 500 MΩ ($\beta = 1$). The third term $e_n^2\left(\frac{1}{R_f^2} + 4\pi^2 C_t^2 f^2\right)$ represents the noise generated by the interaction of the input voltage noise with the input capacitance. The value of e_n ranges from 2 – 3 nV Hz$^{-1/2}$ (176), and we used a value of 3 nV Hz$^{-1/2}$ for e_n in the calculations here. The total input capacitance C_t is equal to the sum of the capacitance in the amplifier C_a and the capacitance of the dielectric material(s) C_d that interacts with the headstage (see preceding section for numerical values of C_d). With no load connected to the input pins, C_t is equal to C_a. For a headstage amplification of $\beta = 0.1$, the value of C_a is ~ 70 pF (*i.e.* the sum of the capacitance of the FET, which is ~ 20 pF, and an injection capacitance of 50 pF (176)). For a headstage amplification of $\beta = 1$, C_a is ~ 25 pF (*i.e.* the sum of the gate capacitance of the FET, which is ~ 20 pF, and an injection capacitance of 5 pF (176)).

The dash-dot line (-· -·) in Figure 5.3 shows the theoretical RMS value of the noise generated by the headstage and amplifier with a headstage amplification of $\beta = 0.1$. For comparison, we show in Figure 5.4 the theoretical RMS value of the noise generated by the headstage and amplifier when $\beta = 1$. These two figures demonstrate that the headstage and amplifier contribute one of the most important sources of noise in current

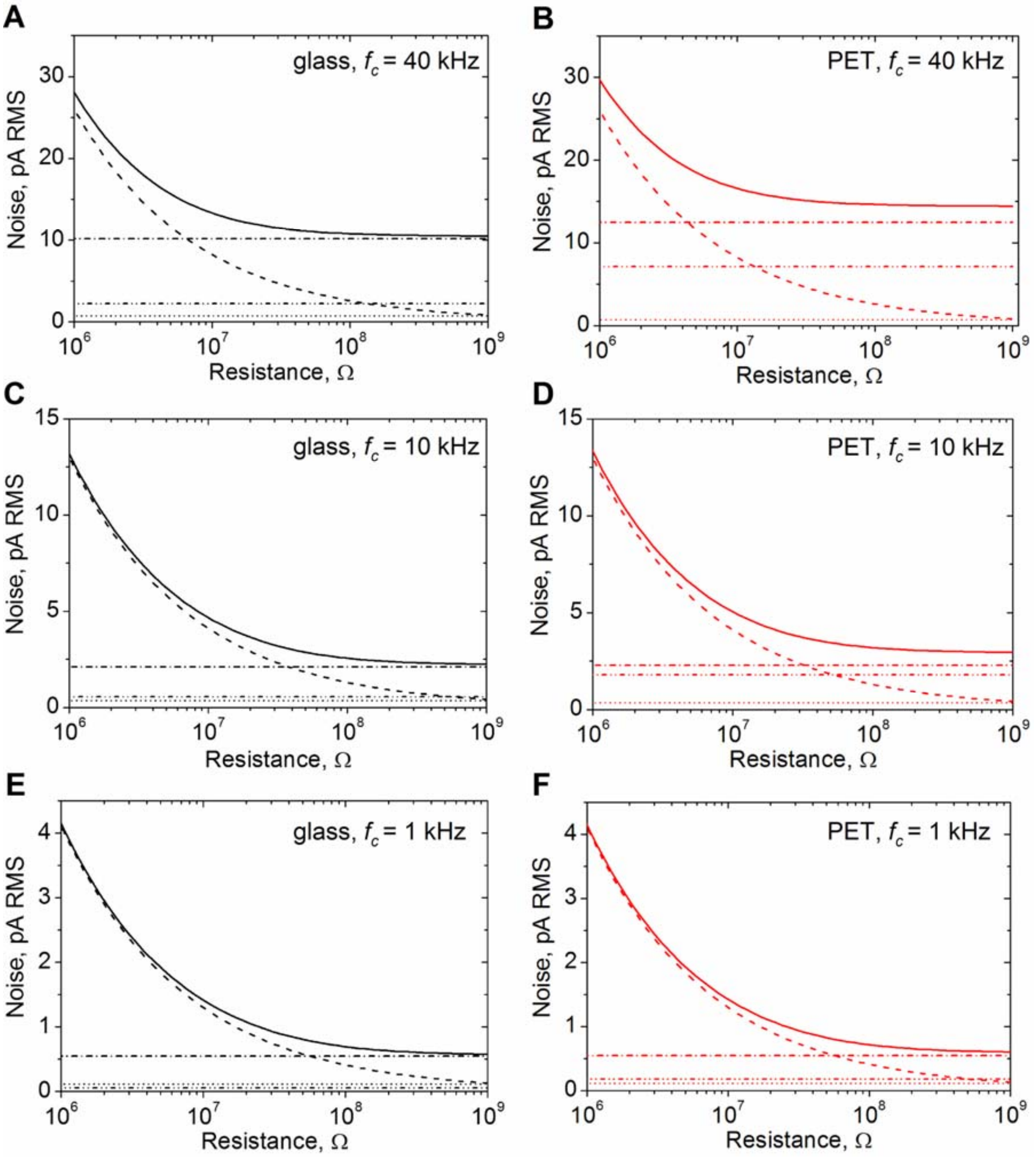

Figure 5.3. Magnitude of four theoretical noise sources and the total theoretical noise in current recordings from submicrometer pores and nanopores as a function of the resistance of the pore structure for a headstage amplification of $\beta = 0.1$ ($R_f = 50$ MΩ, C_a = 70 pF, and G = 50 MV A^{-1}) assuming no excess noise in the feedback resistor (a = 1, other parameters as listed in the text). The graphs show the thermal noise I_T, dielectric noise I_D, headstage and amplifier noise I_A, quantization noise I_Q, and the resulting total noise I_{total}, at three different signal bandwidths for pores fabricated in glass and PET. A) Predicted noise for the glass pores used in this work at a cutoff frequency of f_c = 40 kHz for all sources of noise. The dashed line (- - -) represents the thermal noise I_T of the pore, the dash-dot (-· -·) line represents the noise of the headstage and amplifier I_A, the dash-

dot-dot (-·· -··) line represents the dielectric noise of the substrate I_D, the dotted line (···) represents the quantization noise I_Q, and the solid line (—) represents the total noise I_{total} (*i.e.* the RMS sum of the four noise sources). B) Predicted noise from the four noise sources for the PET pores used in this work with f_c = 40 kHz. Note that the increased capacitance and dissipation factor of the PET pores compared to glass pores increased the dielectric noise, the headstage and amplifier noise, and the total noise. C) Same graph as in A) except with f_c = 10 kHz. D) Same graph as in B) except with f_c = 10 kHz. E) Same graph as in A) except with f_c = 1 kHz. F) Same graph as in B) except with f_c = 1 kHz. At this reduced cutoff frequency, the increased capacitance and dissipation factor of PET pores compared to glass pores did not result in a significant increase in the noise.

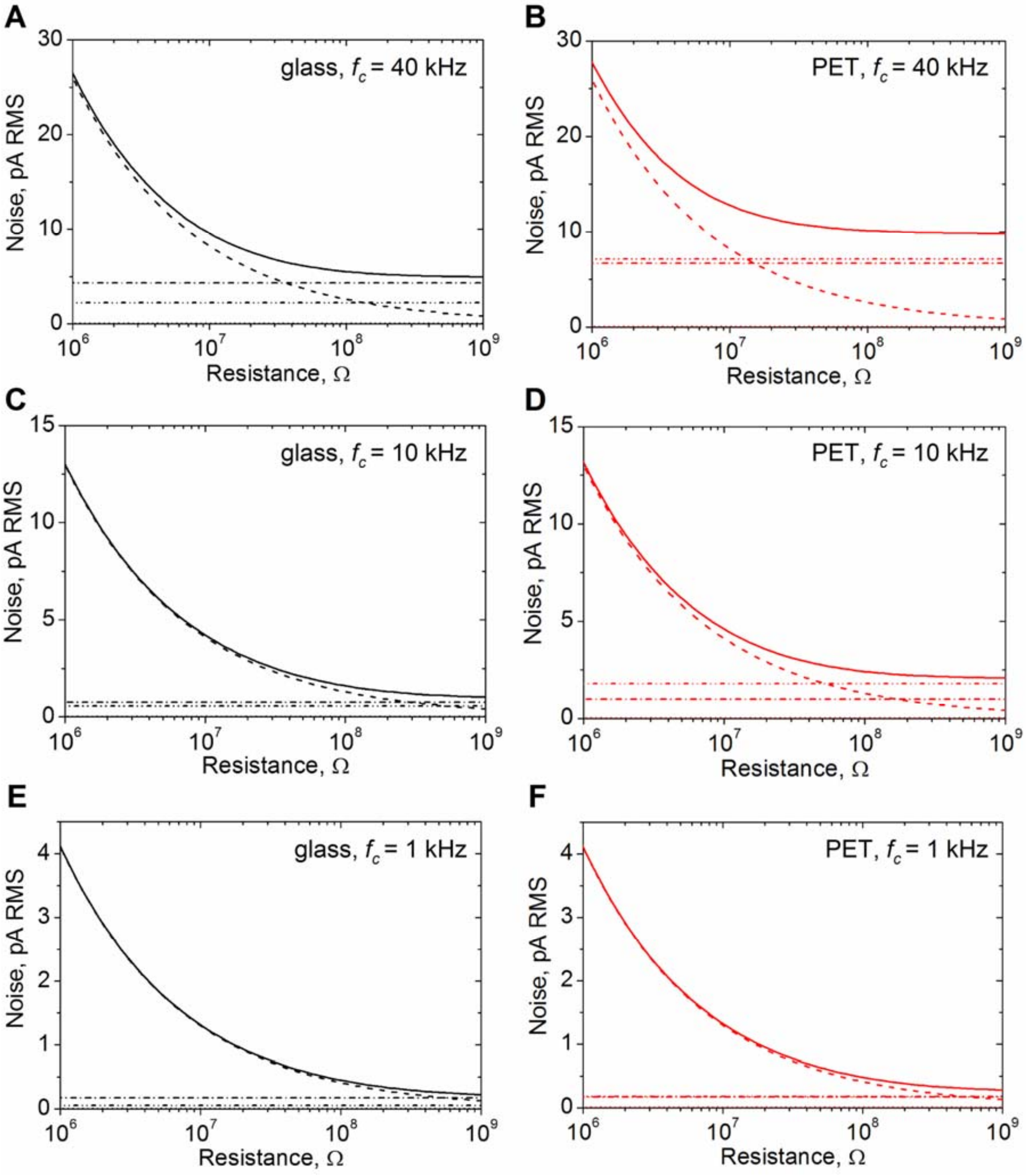

Figure 5.4. Magnitude of four theoretical noise sources and the total theoretical noise in current recordings from submicrometer pores and nanopores as a function of the resistance of the pore structure for a headstage amplification of β = 1 (R_f = 500 MΩ, C_a = 25 pF, and G = 500 MV A^{-1}) assuming no excess noise in the feedback resistor (a = 1, other parameters as listed in the text). A) Predicted noise for the glass pores used in this work at a cutoff frequency of f_c = 40 kHz for all sources of noise. The dashed line (- - -) represents the thermal noise I_T of the pore, the dash-dot (-· -·) line represents the noise of the headstage and amplifier I_A, the dash-dot-dot (-·· -··) line represents the dielectric noise

of the substrate I_D, the dotted line (···) represents the quantization noise I_Q, and the solid line (—) represents the total noise I_{total} (*i.e.* the RMS sum of the four noise sources). B) Predicted noise from the four noise sources for the PET pores used in this work with f_c = 40 kHz. Note that dielectric noise is now larger than the headstage and amplifier noise. C) Same graph as in A) except with f_c = 10 kHz. D) Same graph as in B) except with f_c = 10 kHz. E) Same graph as in A) except with f_c = 1 kHz. F) Same graph as in B) except with f_c = 1 kHz.

recordings for pores with resistances greater than ~10 MΩ when β = 0.1 and ~50 MΩ when β = 1. Overall, we expect that the noise of the headstage and amplifier will be significant (or dominant) in many experiments (especially experiments that require high signal bandwidths). We discuss methods for minimizing I_A in later sections of this chapter.

Theoretical noise generated by the pore:

To a first approximation, the overall pore structure can be considered as a simple resistive element. Resistors generate noise due to thermal agitation of charge carriers inside the device (176), and this type of noise is known as thermal noise (also called Johnson noise or Nyquist noise). The power spectral density of thermal noise $S_T^2(f)$ is given by Eq. 5.6 and the RMS thermal noise $I_T(f_c)$ is given by Eq. 5.7 (147,176):

$$S_T^2(f) = \frac{4kT}{R}, \tag{5.6}$$

$$I_T(f_c) = \sqrt{\frac{4kTc_1 f_c}{R}}, \tag{5.7}$$

where R (Ω) is the resistance of the pore structure, k is Boltzmann's constant, $1.38\cdot10^{-23}$ m^2 kg s^{-2} K^{-1}, and T (K) is the temperature (here, T = 294 K). The dashed lines (- - -) in

Figures 5.3 and 5.4 show the resulting theoretically estimated RMS value of the thermal noise I_T as a function of the resistance of the pore structure for three different signal bandwidths using Eq. 5.7.

We think that Eqs. 5.6 and 5.7 provide a reasonable approximation of the thermal noise that is generated by many of the pore structures that are commonly used; however, if the capacitance of the substrate is large (greater than ~100 pF), or the resistance of the pore is large (greater than ~100 MΩ), or the resistance leading to and from the pore is large (greater than ~500 Ω), Eqs. 6 and 7 may no longer accurately describe the thermal noise of the pore structure. In this instance, it may be more accurate to derive the theoretical thermal noise equation of the pore from the model circuit of the pore (Figure 5.2) rather than using Eqs. 6 and 7 (147). For comparison, we present a general method for determining the thermal noise from the model circuit in Appendix 5.A, and we used this method to derive thermal noise equations for the model circuits presented in Figure 5.2.

Based on the graphs in Figures 5.3 and 5.4, we predict that the thermal noise generated by the pore structure is an important or dominant source of noise for both dielectric materials given that the resistance of the pore is smaller than ~50 MΩ (at bandwidths smaller than 10 kHz, thermal noise dominates up to approximately 400 MΩ). As a general rule, the thermal noise of the pore is the minimum amount of noise achievable in a current trace, and we expect that it will be a significant source of noise in many experiments. Thermal noise cannot be reduced for a pore structure with a given resistance without lowering the bandwidth; we therefore discuss in later sections of this paper ways to perform measurements with the optimal signal bandwidth to reduce the thermal noise to its minimum value without compromising the accuracy of resistive-pulse recordings.

Theoretical noise generated by the substrate material:

Synthetic nanopores are typically fabricated in dielectric materials such as silicon dioxide, silicon nitride, glass, and polymers. While these materials provide excellent substrates that can be chemically and mechanically robust, they exhibit loss in the form of thermal energy. The thermal energy generated by this loss generates thermal noise from the dielectric material (176), and this type of noise is known as dielectric noise. The power spectral density of dielectric noise $S_D^2(f)$ is given by Eq. 5.8 and the RMS dielectric noise $I_D(f_c)$ is given by Eq. 5.9 (147,176):

$$S_D^2(f) = 8\pi\, kTDC_d f\ , \tag{5.8}$$

$$I_D(f_c) = \sqrt{4\pi\, kTDC_d c_2 f_c^2}\ , \tag{5.9}$$

where D is the dissipation factor (dielectric loss tangent, unitless) of the material(s), and C_d (F) is the capacitance of the dielectric(s).

In general, D is determined by combining the dielectric loss of all materials that contribute to the capacitance C_d. These materials do not, however, contribute to D equally; thus it can be difficult to determine an exact value of D (134). Since the pores that we used were made of a single substrate material, either glass or PET, (and the substrate did not require any form of support that made a significant contribution to Cd), we estimated D as the dielectric loss of the material in which the pore was fabricated (D is frequency dependent but usually changes minimally over the range of frequencies of interest here (176)). For the conical pores in Corning 0211 borosilicate glass, the value of D was 0.0047 and the capacitance of the dielectric was $C_d = C_s + C_m + C_c \approx 10$ pF (217). For the cylindrical pores fabricated in PET, the value of D was 0.016 and the capacitance of the dielectric was $C_d = C_s \approx 30$ pF (218). The dash dot dot line (-·· -··) in Figures 5.3 and 5.4 shows the theoretical RMS value of the dielectric noise of the glass and PET pores for three signal bandwidths.

Figures 5.3 and 5.4 demonstrate that the increased capacitance and dissipation factor of the PET pores compared to the glass pores causes an increase in the dielectric noise of the substrate (as well as the noise of the headstage and amplifier). In the case of PET pores with resistances larger than ~50 MΩ, reducing the noise of the headstage and amplifier by selecting a headstage amplification of $\beta = 1$ renders the dielectric noise the largest source of noise. Dielectric noise can be particularly important for high signal bandwidth applications since the RMS value of the dielectric noise grows linearly with the signal bandwidth (Eq. 5.9). We discuss methods for minimizing dielectric noise in later sections of this paper.

Theoretical noise generated by the digitizer:

The digitizer converts an analog signal to a discrete signal by performing an operation known as quantization. Quantization refers to the mapping of each value of an analog signal to an integer multiple of a fundamental value known as the quantizing step, δ (unitless) (176). The approximation of the original signal by the discrete values available to the digitizer adds additional noise to the signal, and this noise is known as quantization noise. If the analog signal is “reasonably large” compared to δ, then the power of the quantizing noise can be approximated by $\delta^2/12$ (176). During digitization, the signal is sampled at a specific frequency f_s as well as quantized. The power of the quantizing noise lies in the band of frequencies from 0 to $f_s/2$ and is usually independent of frequency (176). Hence the power spectral density of the voltage quantization noise $S_{QV}^2(f)$ can be approximated by Eq. 5.10 and the RMS voltage quantization noise $V_Q(f_c)$ can be approximated by Eq. 5.11 (176) (recall that the current flowing through the pore is converted to a voltage by the I-V converter before quantization):

$$S_{QV}^2(f) = \frac{\delta^2}{6f_s}, \tag{5.10}$$

$$V_Q(f_c) = \sqrt{\frac{\delta^2 c_1 f_c}{6f_s}}. \tag{5.11}$$

The digitizer that we used has 16 bits of accuracy and accepts signals from +10 V to –10 V (*i.e.*, the full scale range, FSR, of the digitizer is ± 10 V). Hence $\delta = 20\text{ V} / 2^{16} = 0.305\text{ mV}$ (this value was held constant throughout all of the experiments). In order to obtain the power spectral density of the quantization noise and RMS quantization noise expressed in current, $S_{QA}^2(f)$ and $I_Q(f_c)$, the overall gain of the system G (V A^{-1}) must be included in Eqs. 5.10 and 5.11:

$$S_{QA}^2(f) = \frac{\delta^2}{6f_s G^2}, \tag{5.12}$$

$$I_Q(f_c) = \sqrt{\frac{\delta^2 c_1 f_c}{6f_s G^2}}. \tag{5.13}$$

In the experiments discussed here, G was $5 \cdot 10^7$ V A^{-1} for $\beta = 0.1$ and $5 \cdot 10^8$ V A^{-1} for $\beta = 1$. We held f_s constant at a value of 500 kHz throughout all experiments. Note that the coefficient of correction c_1 present in Eqs. 5.11 and 5.13 is only used if the quantization noise has been filtered by a digital filter, otherwise this coefficient should be removed. The dotted lines (···) in Figures 5.3 and 5.4 show the theoretical RMS value of the quantization noise generated by the digitizer for three bandwidths.

Figures 5.3 and 5.4 show that the quantization noise is typically not an important source of noise. In most cases, we do not expect quantization noise to make a significant contribution to the overall noise in a current trace; however, since this noise source is added in *after* the current trace is filtered with an analog filter, it can be significant in current traces that have been strongly filtered with analog filters. As we show in a following section, the experimentally determined noise generated by the digitizer can also be greater than what is predicted by the quantization noise equation. Therefore we discuss methods for minimizing quantization noise in the later sections of this paper.

Calculation of the total theoretical RMS noise:

The total theoretical RMS value of the noise can be calculated by considering the underlying random nature of the sources of noise. This randomness causes uncorrelated noise sources to add in an RMS fashion (Eq. 5.14) (176). Since the RMS value of the thermal noise of the pore I_T, the dielectric noise of the substrate I_D, the noise of the amplifier I_A, and the quantization noise of the digitizer I_Q are uncorrelated, the total RMS noise I_{total} is equal to:

$$I_{total} = \sqrt{I_T^2 + I_D^2 + I_A^2 + I_Q^2} \ . \qquad (5.14)$$

Due to the RMS addition of the sources of the noise, the largest source(s) of noise tends to dominate the total noise as shown in Figures 5.3 and 5.4. Considering this characteristic is crucial for attempts to reduce the noise of the current recordings.

To predict accurately the total RMS noise, the noise bandwidth of each source must be determined. In general, the signal bandwidth of the HAFD combination (or HAFD-digital filter combination) should be used for calculations of the noise bandwidth of the headstage and amplifier noise, the dielectric noise of the substrate, and the thermal noise of the pore (219). The remaining source of noise to consider for calculating the total noise is quantization noise, which is added after the current trace has been filtered with an analog filter. If the current trace is not filtered digitally, then quantization noise will have a noise bandwidth of $f_c = f_s/2$ (as mentioned above, no correction coefficient is used (176)). If a digital filter is used, the noise bandwidth of the quantization noise can be calculated from the signal bandwidth of the digital filter by using the correction coefficient

To summarize, the total theoretical noise of current recordings from submicrometer pores or nanopores is dominated by the largest source(s) of noise. Figure 5.3 shows that the total noise is dominated by thermal noise for PET and glass pores with resistances less than 10 - 50 MΩ. For pores with resistances greater than ~50 MΩ, the largest source of noise is the headstage and amplifier. If the noise of the amplifier can be reduced by choosing a larger headstage amplification (β = 1 rather than 0.1), then the noise of glass pores with resistances above ~50 MΩ can be dominated by the thermal noise of the pore instead of the headstage and amplifier noise whereas the noise of PET pores with resistances above ~50 MΩ can be dominated by dielectric noise.

Effect of substrate capacitance on current noise:

The capacitance of the substrate that contains the pore can have a significant effect on the noise of a current trace since it influences the noise of the headstage and amplifier, the dielectric noise of the substrate, and potentially the thermal noise of the pore (as discussed in Appendix 5.A). To examine the effect of substrate capacitance, we plotted in Figure 5.5 the theoretical RMS noise of the four individual sources as well as the total noise as a function of the substrate capacitance. Since we allowed the substrate capacitance to range from 10 pF to 2 nF, we used a thermal noise equation (Eq. 5.A.6) which includes the effect of the substrate capacitance (derived for cylindrical pores, Figure 5.2B); this equation and its derivation are provided in Appendix 5.A. In Figure 5.5, we examine a "low-noise scenario" ($D = 0.0047$ and $\beta = 1$, Figure 5.5A,C,E) and a "high-noise scenario" ($D = 0.016$ and $\beta = 0.1$, Figure 5.5B,D,F) at three different signal bandwidths. In both scenarios, we found that the capacitance of the substrate had an increasing effect on the noise at higher bandwidths as expected from the theoretical equations. It is therefore critical to use a substrate with low capacitance (≤ 100 pF) to obtain recordings with low-noise at high signal bandwidths.

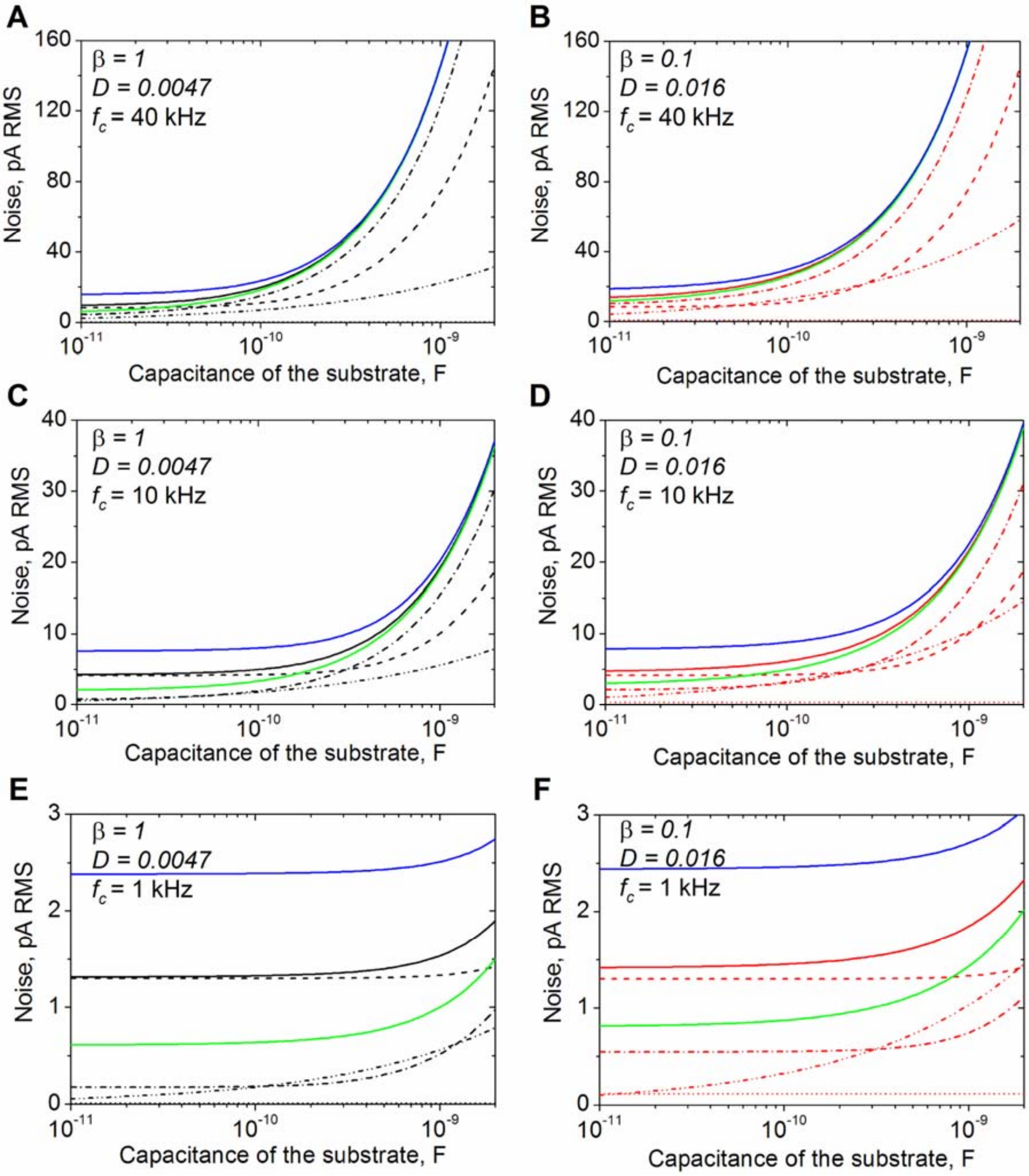

Figure 5.5. Magnitude of four theoretical noise sources and the total theoretical noise in current recordings from submicrometer pores and nanopores as a function of the capacitance of the substrate C_s. The graphs show the thermal noise $I_{T\text{-}Cyl}$ (- - -, calculated using Eq. 5.A.6 from Appendix 5.A) derived for a cylindrical pore structure (Figure 5.2B), the headstage and amplifier noise I_A (-·· -··, Eq. 5.5), the dielectric noise I_D (-··· -···, Eq. 5.9), the quantization noise I_Q (···, Eq. 5.13), and the resulting total noise I_{total} (—, Eq. 5.14) at three different signal bandwidths for a "low-noise" case (black curves) with D = 0.0047 and β = 1 and a "high-noise" case (red curves) with D = 0.016 and β = 0.1. The black and red curves in each plot were calculated for a pore with a resistance of R_p = 10

MΩ ($R_a = R_{w1} + R_{w2} = 350$ Ω). The blue and green curves show the total noise for two additional values of the resistance of the pore: R_p = 3 MΩ (blue) and R_p = 50 MΩ (green). A) Predicted noise at a signal bandwidth of 40 kHz for pores with a dielectric loss $D = 0.0047$, headstage gain $\beta = 1$ (R_f = 500 MΩ, C_a = 25 pF, and G = 500 MV A^{-1}) and assuming no excess noise in the feedback resistor ($a = 1$). B) Predicted noise at a signal bandwidth of 40 kHz for pores with a dielectric loss $D = 0.016$, headstage gain $\beta = 0.1$ (R_f = 50 MΩ, C_a = 70 pF, and G = 50 MV A^{-1}) and assuming no excess noise in the feedback resistor ($a = 1$). C) Identical to graph as in A except with f_c = 10,000 Hz. D) Identical to graph as in B except with f_c = 10,000 Hz. E) Identical to graph as in A except with f_c = 1,000 Hz. F) Identical to graph as in B except with f_c = 1,000 Hz.

Comparison of theoretical and experimental noise of the digitizer and amplifier:

In order to test the accuracy of the theoretical equations of the noise of the headstage and amplifier and the digitizer, we compared the theoretically calculated values with experimental results. To determine experimentally the quantization noise power S_{QA}^2, we examined the power spectra of current recordings after filtering with analog filters that reduced the noise power from the other sources of noise below that of the noise power of the digitizer as shown in Figure 5.6A. We determined the quantization noise power from the flat part of the power spectrum at frequencies higher than the roll-off of the filter that was used. This analysis provided a value of $S_{QA}^2 = 2.1\cdot10^{-4} \pm 0.38\cdot10^{-4}$ pA^2 Hz^{-1} for $\beta = 0.1$ and a value of $S_{QA}^2 = 2.0\cdot10^{-6} \pm 0.26\cdot10^{-6}$ pA^2 Hz^{-1} for $\beta = 1$. Using Eq. 5.12, we obtained $S_{QA}^2 = 1.24\cdot10^{-5}$ pA^2 Hz^{-1} for $\beta = 0.1$, and $S_{QA}^2 = 1.24\cdot10^{-7}$ pA^2 Hz^{-1} for $\beta = 1$. In contrast, both of the experimentally measured values were approximately 16 times larger than the theoretical values (the two measured values for $\beta = 0.1$ and $\beta = 1$ were, however, different by a factor of 100 which agrees with the expectation based on Eq. 5.12; we also examined other gain settings of the

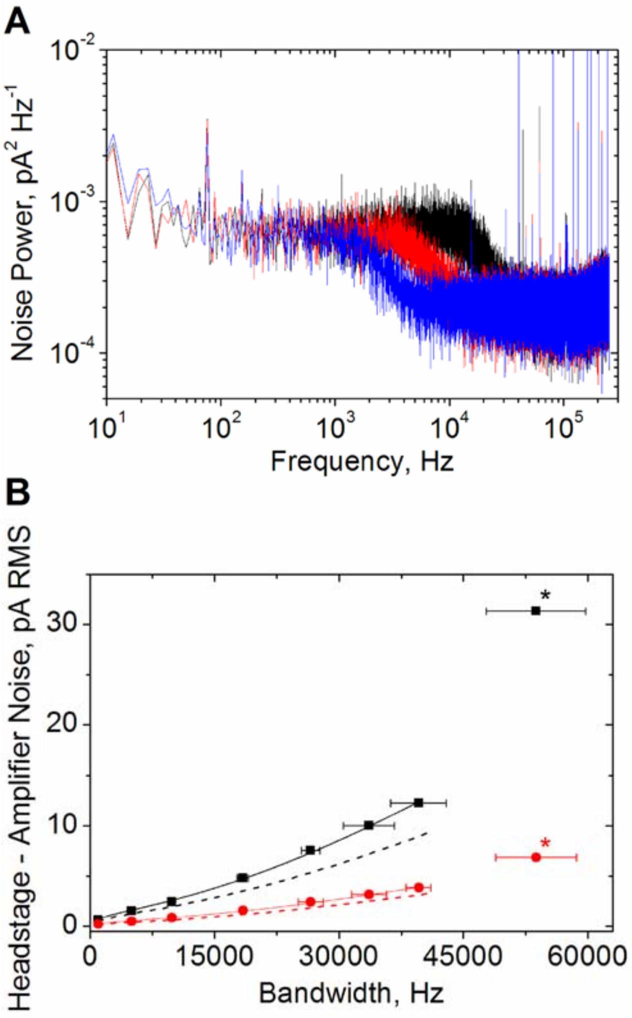

Figure 5.6. Power spectra used to determine experimentally the amount of quantization noise and dependence of the RMS noise generated by the amplifier on the signal bandwidth. A) Power spectra calculated from current traces that were recorded with a headstage gain of β = 0.1. An analog low-pass Bessel filter with four poles and a bandwidth of 10 kHz (black), 5 kHz (red), and 2 kHz (blue) was used to reduce the noise of the current trace below that of the quantization noise that was added in during digitization. The flat region of the power spectra at frequencies higher than the cutoff frequency of the filter was used to calculate the value of the quantization noise; the average value of the flat region of the three traces was $2.1 \cdot 10^{-4} \pm 0.38 \cdot 10^{-4}$ pA^2 Hz^{-1}. The power spectra used to determine experimentally the quantization noise with β = 1 were very similar to the ones shown here. B) Noise generated by the combination of the headstage (no load applied to the input pins) with the patch clamp amplifier as a function of the bandwidth at two different settings of the gain: β = 0.1 (black) and β = 1 (red). All data points were obtained by selecting the signal bandwidth by digital filtering (220) except for the two points marked with an asterisk (which were obtained by analog filtering only). The dashed lines were calculated (not fitted) using Eq. 5.5 without consideration of excess noise (*a* = 1). The solid lines were generated by fitting Eq. 5.5 to

the data using a and C_t (since there was no load attached, $C_t = C_a$) as fitting parameters. For β = 0.1, the best fit ($R^2 \geq 0.99$) generated a value of $a = 1.6$ and of $C_a = 98$ pF. For β = 1, the best fit ($R^2 \geq 0.99$) generated a value of $a = 1.9$ and of $C_a = 30$ pF. The points marked with an asterisk were excluded from the best fit analysis (221).

amplifier and in each case the changes between the measured values of noise always agreed with Eq. 5.12). This large discrepancy may be caused by the digitizer adding extra noise to the quantization noise.

The power spectrum of the quantization noise was constant over the frequency range of interest as predicted by theory, hence we were able to subtract the experimentally determined quantization noise from the measured value of the noise of the recording electronics. The resulting experimentally determined headstage and amplifier noise made it possible to compare the theoretical equations of the RMS noise generated by the amplifier (no load applied to the input pins) with the measured RMS noise from current traces that were filtered with digital Gaussian low-pass filters of varying cutoff frequency for β = 0.1 and β = 1 as shown in Figure 5.6B.

Since the capacitance of the amplifier C_a and the constant representing excess noise in the feedback resistor a were not well defined, we carried out best fit analyses with the experimental data points (except for the data points marked with an asterisk (221)) with Eq. 5.5 by using C_a and a as fitting parameters (since no load was connected to the input pins, $C_a = C_t$). With this procedure, we obtained excellent fits for β = 0.1 with $C_a = 98$ pF and $a = 1.6$ as well as for β = 1 with $C_a = 30$ pF and $a = 1.9$ as shown in Figure 5.6B. We also examined the accuracy of Eq. 5.5 if we would use $a = 1$ (no excess noise in the feedback resistor) as well as the values for C_a that we estimated from the specifications of the manufacturer and Sherman-Gold (176) ($\beta = 0.1$, $C_a = 70$ pF; $\beta = 1$, $C_a = 25$ pF). In this case, the maximum error between the measured noise and the theoretical noise was ≤ 30% for both $\beta = 0.1$ and for $\beta = 1$ (not including the data points with an asterisk).

In summary, the experimental value of the noise of the digitizer was significantly higher than the theoretical value of the quantization noise. The theoretical equations of the quantization noise, however, accurately predicted the reduction in the noise of the digitizer caused by an increase in the gain of the amplifier. Therefore, the theoretical quantization noise equations are useful for predicting the change of the experimentally measured digitizer noise when a given parameter of the experiment is modified. For the case of the amplifier and headstage noise, two parameters in Eq. 5.5 were not well defined so we fit the experimental noise data with this equation. We obtained excellent fits and the values of the amplifier capacitance obtained from the fits were close to the theoretically estimated values.

A combination of theory and experimental results enabled an accurate prediction of the total noise of pores in glass or PET substrates:

One of the main goals of this work was to enable the prediction of the expected noise of current recordings from pores with a variety of geometries that were fabricated in various materials. To this end, we demonstrate the accurate prediction of the experimentally observed noise of pores in glass or PET substrates. The pores in glass substrates that we used had conical geometry and diameters ranging from 250 nm to 1.5 µm (Figure 5.2A). The pores in PET substrates that we used had cylindrical geometry and diameters ranging from ~10 nm to 610 nm (Figure 5.2B). In order to predict the current noise, we used Eq. 14 with C_a = 98 pF and a = 1.6 for β = 0.1 and with C_a = 30 pF and a = 1.9 for β = 1 (as obtained from the best fits shown in Figure 5.6B) to perform the calculation of the theoretical noise of the headstage and amplifier (all other values were used as given previously in the text). For the quantization noise, we used the experimentally measured value since it was straightforward to determine and significantly greater than the theoretical value (as mentioned before). We used the thermal noise and dielectric noise equations as given by Eqs. 5.7 and 5.9.

In order to carry out the analysis, we determined first the experimental signal bandwidth of the HAFD-digital filter combination (using Eq. 5.2) by measuring the $t_{10\text{-}90}$ of a digitally filtered square wave that we coupled in capacitively after mounting the glass pores or PET pores in the recording setup. From this experimental value of the signal bandwidth, we then calculated the theoretically predicted noise values for pores in PET or glass as a function of resistance. As shown in Figure 5.7, the predicted noise values and the measured values were in excellent agreement, in particular for recordings at signal bandwidth ≤ 23 kHz. Consequently, the theoretical approach described here can be used to predict accurately the expected noise from pores *before* fabricating these pores and *before* carrying out any experiments. This predicted, minimal achievable noise can be used to assess the best possible signal-to-noise ratio for resistive pulse recordings of objects that move through the submicrometer- or nanometer-sized pores by combining

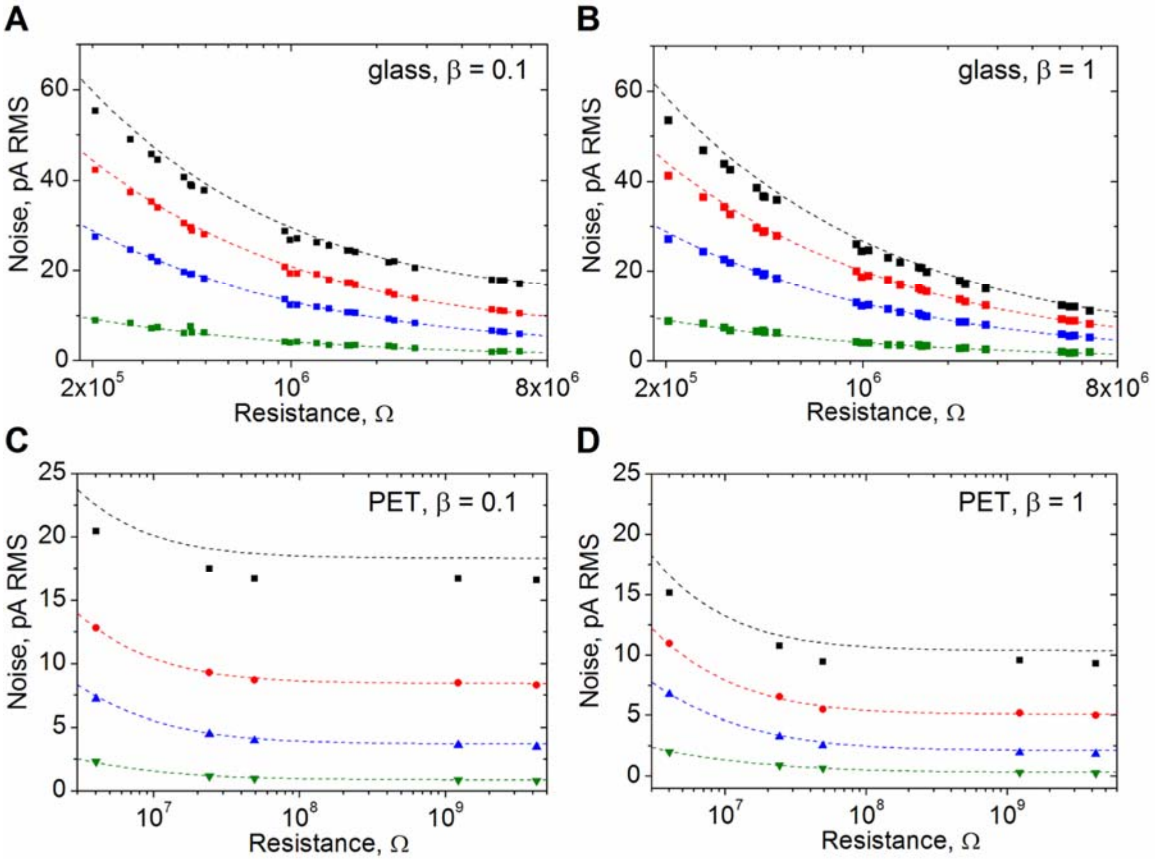

Figure 5.7. Comparison between predicted and measured noise of pores fabricated in glass and PET at four different signal bandwidth values (*i.e.*, the original current trace was filtered with a digital Gaussian low-pass filter with one of four different cutoff frequencies). The signal bandwidth of the HALD-digital filter combination was determined experimentally from the t_{10-90} risetime; it was ~40 kHz (black), ~23 kHz (red), ~10 kHz, (blue), and ~1 kHz (green). The dashed lines were calculated using Eq. 5.14 with the modifications to the individual sources of noise as discussed in the text. A) Predicted and measured noise values from conical pores in glass with diameters ranging from 250 nm to 1.5 μm as a function of the resistance of these pores with β = 0.1 (parameters used for calculating the predicted noise as discussed in the text). B) Identical graph as in A except with β = 1 (parameters used for calculating the predicted noise as discussed in the text). C) Noise values measured from cylindrical pores in PET with diameters ranging from ~10 nm to 610 nm as a function of the resistance of these pores (β = 0.1). D) Identical graph as in C except with β = 1. The recording buffer for experiments with the glass pores was either 1.00 M KCl with 0.01 M phosphate buffer pH 7.3 and 0.1% w/v Triton X-100 or 0.15 M KCl with 0.01 M phosphate buffer pH 7.3 and 0.1% w/v Triton X-100; the recording buffer for the experiments with the PET pores was 1.00 M KCl with 0.01 M phosphate buffer pH 7.3 and 0.1% w/v Triton X-100. The applied voltage was 0.0 V in all cases.

the analysis with theoretical equations for predicting the amplitudes from translocating objects (22,24,25,27,28,106,168,203).

One surprising result from Figure 5.7 is that at the highest signal bandwidth (40 kHz), the pores in glass and in PET generated a measurable current noise that was *smaller* than the theoretically predicted value (which we expected to be the minimal possible noise). For pores in glass the maximum difference between the measured and predicted noise value was ≤ 8.5% and for the pores in PET is was ≤ 12% for either value of β. We think that these decreased experimental noise levels at the highest signal bandwidths are mainly due to inaccuracies in the measurement of the signal bandwidth of the HAFD-digital filter combination (222).

To summarize, in the absence of an applied voltage, the total noise from current recordings through submicrometer- and nanometer-size pores can be predicted with high accuracy up to a signal bandwidth of 23 kHz (error < 5%); at a signal bandwidth of 40 kHz, this prediction is still within an error of 12%. The equations provided above (Eqs. 5.4-14) also provide insight on possible strategies to reduce the inherent current noise of recordings from submicrometer pores and nanopores.

Application of a voltage, in some cases, increased the noise of the current trace:

Many of the experiments that use submicrometer pores and nanopores for sensing require the application of a voltage across the membrane in order to monitor the current flowing through the pore. The application of a voltage can, however, cause an increase in the noise of the current trace (in some cases, the noise can grow by more than one order of magnitude) (85,125,126). Therefore, we examined the noise for all pores used in this work while applying a voltage. Typical resistive-pulse sensing experiments use a voltage of 0.1 – 0.4 V (39,41,72,108,189,190). Here we limit our discussion to pores that produced currents smaller than 200 nA (the saturation value of the amplifier) under voltage biases ≤ 0.4 V (*N* = 17). Figure 5.8 shows that, in some cases, the noise increased significantly after a voltage was applied. For glass pores, the magnitude of the increase showed a weak dependence on the resistance of the pore with increased noise at low resistance values. For PET pores, we observed almost no change in the noise.

In general, the noise generated by the headstage and amplifier, the quantization noise generated by the digitizer, the dielectric noise generated by the substrate, and the thermal noise generated by the pore are not expected to increase when a voltage is applied (or when current flows). So the question is, what caused the extra noise when a voltage is applied? One possible source is shot noise (176,205,207,223-227). RMS shot noise is usually modeled as increasing proportionately with the square root of the current, which would agree with the trend of increasing noise with decreasing resistance in glass pores; however, significant amounts of shot noise are only expected in circuits that contain a potential barrier (such as a diode or certain ion channels) (223,226,228,229) and the power spectral density of shot noise is independent of frequency (147,223,228). As far as we know, the pores used in this work did not contain a potential barrier and they did not exhibit rectification. Nanopores, under certain conditions, can be strongly rectifying (69,117-119,121,122) and hence may contain a potential barrier; these pores may therefore require a shot noise term to predict the noise accurately.

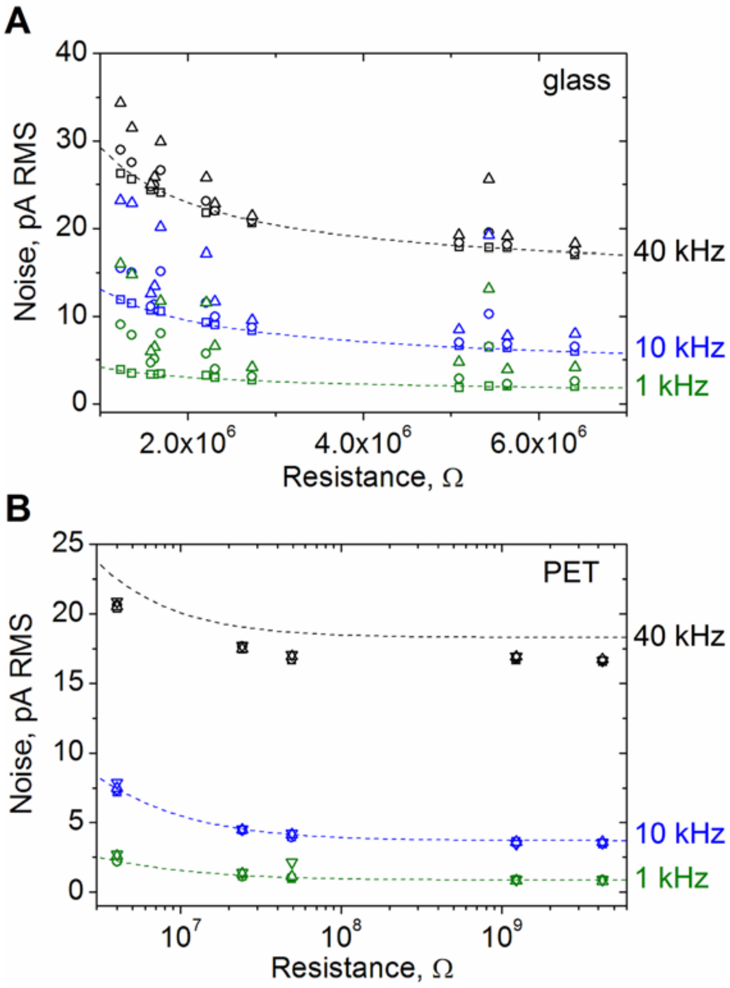

Figure 5.8. Influence of an applied voltage on the RMS current noise recorded from pores in glass and PET substrates. A) Noise measured with glass pores at a signal bandwidth of ~40 kHz (black), ~10 kHz (blue), and ~1 kHz (green) with an applied voltage of 0 V (squares), 0.1 V (circles) or 0.2 V (up triangles) with a headstage gain of β = 0.1. B) Noise obtained from PET pores at a signal bandwidth of ~40 kHz (black), ~10 kHz (blue), and ~1 kHz (green) with an applied voltage of 0 V (square), 0.1 V (circles), 0.2 V (up triangles), or 0.4 V (down triangles) with a headstage gain of β = 0.1. The recording buffer for the glass pores was either 1.00 M KCl with 0.01 M phosphate buffer pH 7.3 and 0.1% w/v Triton X-100 or 0.15 M KCl with 0.01 M phosphate buffer pH 7.3 and 0.1% w/v Triton X-100. The recording buffer for the PET pores was 1.00 M KCl with 0.01 M phosphate buffer pH 7.3 and 0.1% w/v Triton X-100.

Figure 5.9 shows that the increase in the power of the noise that we observed under an applied voltage was clearly dependent on frequency. Specifically, as the frequency decreased below approximately 50 kHz, the power of the noise from the current traces with an applied voltage increased linearly (on a log-log plot) whereas the power of the noise from the current trace without an applied voltage remained flat. Figure 5.9 also shows that the linear increase in noise power was maintained from the initial frequency at which the noise power began to increase (which varied from pore to pore) until the lowest frequencies on the power spectra (~6 Hz) (230).

A linear increase of the noise power as a function of decreasing frequency in a double logarithmic plot is in agreement with so-called 1/f noise or flicker noise. This type of noise is characterized by a power spectrum S_F^2 of (178):

$$S_F^2 = \frac{c}{f^{\alpha}}, \tag{5.15}$$

where c is a constant (and usually has the value 1) and α is close to 1. The value of α can vary considerably, and discussions on 1/f noise include values of α that range from 0 – 2 (178). Noise with the type of power spectra as shown in Figure 5.9 has been observed previously in nanopore structures that were fabricated in synthetic membranes (85,125,126), and recent reports have proposed a physical origin including nanobubbles in the pore (125) or mobile surface charges on the surface of the walls of the pore for the generation of this noise (126).

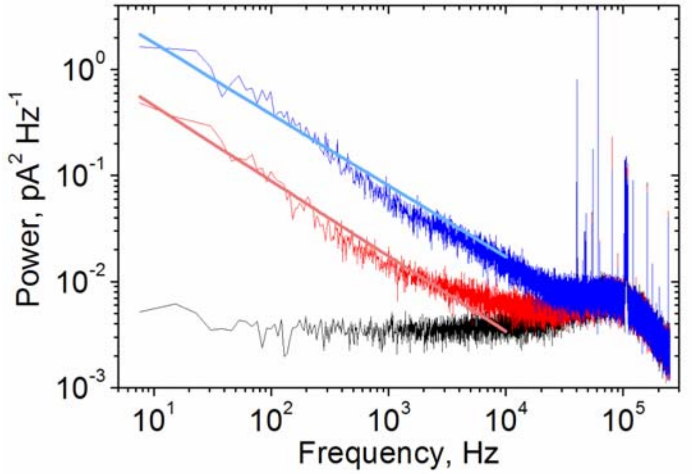

Figure 5.9. Representative power spectra of the current noise recorded from a glass pore that exhibited a large amount of extra noise under an applied voltage of 0.0 V (black), 0.1 V (red), 0.2 (blue). The light blue and the light red line were generated by fitting the power spectra to Eq. 15. For the light red line, α was equal to 0.70 ± 0.005; for the light blue line, α was equal to 0.67 ± 0.004.

In order to examine if the extra noise that we found experimentally with the glass pores when we applied a voltage had a 1/f origin, we fitted the power spectra of the current noise from these pores with Eq. 5.15 (applied voltage of 0.2 V). We obtained good fits with values for *c* that varied between 0.2 – 8.4 (average of 3.0 ± 2.4) and values for α that varied between 0.4 – 0.8 (average of 0.6 ± 0.1). To examine this extra noise in more detail, we compared the results reported here with a simple theoretical model of 1/f noise derived from experimentally similar conditions. In this approach, Hooge *et al.* predicted that the RMS value of the noise increases linearly (on a linear scale) with voltage (178,231). We found that approximately 66% of the glass pores that we examined followed a roughly linear trend in a voltage range of 0 to 0.2 V (signal bandwidth of 1 kHz), albeit with a significant variance in the slopes of the linear best fitted lines (the glass pores with the largest amount of extra noise tended to follow an exponential trend with increasing voltage as opposed to a linear trend). Several of the glass pores generated noise that deviated from this linear trend at 0.4 V, even though the power spectra displayed an apparent 1/f component at low frequencies. In summary, we suggest that the extra noise generated by the glass pores used here was of a 1/f origin, although, at this point, we do not know the exact mechanism causing its generation.

Overall, the occurrence of significant 1/f noise under conditions of an applied voltage appeared random from pore to pore. This variability has been described in other devices that display significant 1/f noise (228). Generally, we (and others) do not conduct current recordings with pores that exhibit amounts of extra noise under an applied voltage since this noise reduces the sensitivity of the measurement (in our experience, these pores are also more prone to clogging compared to pores that do not have significant amounts of extra noise). From an experimental point of view, the best pores exhibit a small increase in RMS noise (≤ 35% at a signal bandwidth of 10 kHz) when a voltage is applied (in our hands, ~60% of the glass pores and all of the PET pores fell in this category). Hence, for many experiments, the noise equations provided here can be used to predict the noise from current recordings with a maximum error of 35% even in the presence of an applied voltage.

5.4. Recommendations for Minimizing the Noise of Current Recordings

In order to minimize the noise of a current trace, it is helpful to analyze the relative magnitude of the contributions from each of the sources of noise. Since the noise values from various sources add in an RMS fashion, the largest source of noise dominates so that any reduction in the smaller values has a minimal effect on the overall noise.

Depending on the parameters of a given experiment, it is possible that any one of the sources of noise listed in the text here may be the dominant noise source. Therefore we will briefly introduce methods for minimizing each source of noise. We exclude the obvious method of reducing the signal bandwidth of the noise sources from these recommendations, as it will be discussed in detail in the next section.

Thermal Noise:

As expected, the thermal noise generated by a pore (or the feedback resistor of the headstage) represents the theoretical minimum amount of noise that can be obtained in a current trace. There are many instances in which this source of noise can be dominant (Figures 5.3 and 5.4), and barring a reduction in the bandwidth, thermal noise can only be reduced by increasing the resistance of the pore. Increasing the resistance of the pore could be achieved by reducing the diameter of the pore or by increasing the length of the pore. The diameter of the pore, however, has to be at least slightly larger than the largest object to be detected and increasing the length of the pore reduces the sensitivity of the pore (24,28,92,114)).

Dielectric noise:

Dielectric noise is dependent on the material(s) in which the pore was fabricated (or on the material of the support structure if applicable) since the dielectric loss D, and to some extent the total capacitance of the dielectric materials C_d, are material properties. Selecting material(s) with a low D such as some types of glass, quartz, or Teflon (134), while at the same time ensuring that C_d is as low as possible will minimize the dielectric noise.

Headstage and amplifier noise:

For pores with resistance values greater than approximately 10 MΩ, we predict that the noise generated by the headstage and amplifier represents an important or dominant source of noise in many cases (Figures 5.3 and 5.4). Hence minimizing this source of noise can have a significant impact on the overall noise of such high resistance pores. The noise of the headstage and amplifier can be minimized by following two key recommendations. One, the total input capacitance C_t should be as low as possible (the RMS value of the input voltage noise of the amplifier grows as $\sqrt{C_t^2 f_c^3}$, and this term becomes the dominant noise source in the amplifier above a few kilohertz bandwidth (176)). Hence the capacitance of the pore structure (and if necessary its support) as well as any injection capacitors (such as the ones used in many patch clamp amplifiers for capacitance compensation) should be reduced as much as possible (injection capacitors are not needed for resistive-pulse sensing experiments but are included in many patch-clamp amplifiers for whole-cell capacitance compensation; whole-cell capacitance compensation should be off for resistive-pulse recordings but these capacitors are still "seen" by the headstage). Two, the feedback resistor used by the amplifier should be as large as possible while still meeting the requirements of the experiment such as a sufficient signal bandwidth and amplifier saturation current (205).

Quantization noise:

It is rare for quantization noise (or the noise generated by the digitizer) to be the dominant noise source; however, if the current signal is filtered with an analog filter that reduces strongly the noise of all other sources, quantization noise can become a significant as it is added *after* the analog filtering step (Figure 5.6A). It is possible to reduce quantization noise by increasing the overall gain G of the amplifier (at least for the experimental setup considered here) or by using a digitizer with a larger number of bits of resolution. Increasing the gain of the amplifier may reduce the total range of detectable currents which can be undesirable if very small and very large signals have to be detected during the same experiment.

5.5. Recommendations for Obtaining Optimal Current Recordings for Resistive-Pulse Sensing Experiments

Submicrometer pores and nanopores are most commonly used to perform resistive-pulse sensing experiments; here we provide recommendations for optimizing the current recordings in the context of these experiments. In general, we think that it is best to record current traces using the highest possible signal bandwidth available from the headstage and amplifier, or in this case the HAFD combination (148,176). This method ensures that the maximum amount of information is contained in the current trace and increases the likelihood that the resistive-pulses in the current trace will be completely resolved. An exception to this recommendation is if the noise level of the current trace is similar to, or considerably higher than the amplitude of the resistive pulse (148); in this case, it would be better to reduce the signal bandwidth of the HAFD combination (and hence the noise) via analog filtering *before* digitization to reduce the RMS noise to less than half the value of the peak amplitude of the resistive-pulse. Failing to employ this noise reduction may lead to inaccuracies in the off-line data analysis (148).

Recording at high signal bandwidths requires a high speed digitizer since the sampling frequency of the digitizer should be at least twice the signal bandwidth of the HAF in order to prevent aliasing, which refers to the shifting (or mapping) of high frequency components to low frequency components. Using the minimum sampling frequency is not recommended since the types of filters used in resistive-pulse sensing experiments generally do not sharply attenuate the noise power at frequencies above their cutoff frequency (and accurate reconstruction of the time domain signal requires more data points than what is provided when the minimum sampling frequency is used) (176). A sampling frequency that is five times the signal bandwidth of the HAF is usually considered to be adequate (in some cases, a sampling frequency that is 10 times the signal bandwidth of the HAF may be advantageous) (176).

After the current trace has been digitized, the overall signal bandwidth of the current trace can be reduced to the optimal value for analysis (defined below) using a digital filter. Reducing the overall signal bandwidth after digitization has the added benefit of reducing the bandwidth of the quantization noise at the same time as the rest of the sources of noise. This procedure reduces the probability that quantization noise will become a dominant source of noise. As mentioned above if only an analog filter is used, the quantization noise may become significant, and a digital filter with a signal bandwidth similar to that of the analog filter would then have to be applied to the current trace.

Reducing the overall signal bandwidth to its optimal value:

If the overall signal bandwidth of the current trace is greater than the signal bandwidth necessary to resolve fully the resistive-pulses contained in the current trace, then additional noise will be included in the data but no additional information. This additional noise can reduce the accuracy with which the peak amplitudes and widths of resistive-pulses are measured. Therefore it is desirable to reduce the overall signal bandwidth to a value slightly higher (but not extensively higher) than the signal bandwidth required by the resistive-pulses in the current trace (usually by using digital filters on the high-signal bandwidth current trace).

It is relatively difficult to know *a priori* the signal bandwidth that will be required to resolve fully the resistive-pulse when a given object passes through the pore, and hence to know the optimum overall signal bandwidth. Fortunately, there is a relatively simple experimental procedure for determining this value assuming that the maximum overall signal bandwidth is greater than the signal bandwidth required to resolve fully the resistive-pulses. Using the maximum available overall signal bandwidth, a current trace can be recorded from the pore with an applied voltage equal to the voltage that will be used during the resistive-pulse sensing experiment. The objects of interest can then be added to one side of the pore and a current trace containing resistive-pulses from these objects can be recorded. In general, even a current trace that contains many resistive-pulse events will still consist mostly of the baseline current with its associated noise.

It is then possible to determine the signal bandwidth required to resolve the events completely by comparing the power spectrum of the current trace without events with the power spectrum of the current trace that contains events; the power spectrum from the current trace with events will display increased power in the range of frequencies that represent the power spectrum of the resistive-pulses when compared to the power spectrum of the current trace without events as shown in Figure 5.10. The optimum overall signal bandwidth for accurate measurements with minimized noise lies somewhat above the frequency where the power spectra converge. For example, since the power spectra from the traces with and without events converged completely at a frequency of approximately 8 kHz in Figure 5.10, we recommend an optimum overall signal bandwidth with a value close to 10 kHz. The overall signal bandwidth can then be reduced to the optimum value (*e.g.* to ~10 kHz in the example above) by using appropriate filtering.

For the pore structures presented here, it is simple to determine the appropriate filtering since the overall signal bandwidth of the current trace is determined by the HAFD combination or HAFD-digital filter combination (*i.e.* the pore does not limit the overall signal bandwidth). Assuming that the signal bandwidth of the HAFD combination was 52 kHz, using a digital Gaussian filter with a cutoff frequency of 11 kHz on the current trace would produce an overall signal bandwidth of ~10 kHz based on Eq. 5.3. If the signal bandwidth of the pore is such that it limits the overall signal

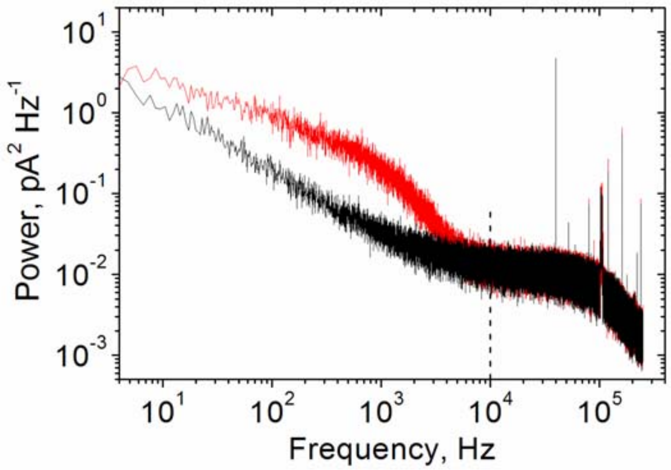

Figure 5.10. Power spectra of current recordings from a submicrometer pore; the black trace was calculated from a recording with no resistive-pulses and the red trace was calculated from a recording that had resistive-pulses caused by virus particles moving through the pore (93). As illustrated by this plot, the highest frequency component of the virus events was less than approximately 8 kHz. The signal bandwidth of the recordings was approximately 52 kHz.

bandwidth, the situation becomes more complicated; in this scenario, the goal is to reduce the signal bandwidth of the HAFD combination (and hence the noise bandwidth of the thermal noise, headstage and amplifier noise, and dielectric noise) (219) as much as possible while ensuring that the overall signal bandwidth remains above the bandwidth of the resistive-pulses.

For example, suppose the signal bandwidth of the HAFD combination was 52 kHz, the signal bandwidth of the pore was 10 kHz, and the signal bandwidth of the resistive pulse was 8 kHz. The overall bandwidth of the current trace is ~10 kHz which is the optimal overall signal bandwidth of the current trace; however, the signal bandwidth of the HAFD is not determined by the signal bandwidth of the pore (219) so extra noise is included in the current trace but no extra information (135,176). Therefore the noise of the current trace should be reduced by using a digital or analog filter with a cutoff frequency of approximately 20 kHz which will not cause a significant decrease in the overall signal bandwidth.

5.6. Conclusion

Based on a detailed discussion of the signal bandwidth and noise of current recordings from individual submicrometer pores or nanopores, we show that these two parameters can critically affect the sensitivity, accuracy, and information content of the recordings from experiments such as resistive-pulse sensing. The bandwidth sets a fundamental limit on the time resolution of changes in the current while the noise helps to determine the sensitivity of a given pore. The signal bandwidth and noise are currently two of the limiting factors for experiments that attempt to sense the very small, often short-lived resistive-pulses (or fluctuations in these pulses) during the passage of individual nucleobases through nanopores for applications such as DNA sequencing. Detection of such small, short-lived events will either require new recording modalities with very low noise at very high-bandwidth or it will require strategies to increase significantly the amplitudes of resistive-pulses (*i.e.* by fabricating pores with very small channel lengths and diameters) possibly combined with a strategy to prolong the duration of pulses from individual bases (*i.e.* by filling the pores with a chemically cross-linked sieving gel). At present, the bandwidth and noise pose a fundamental challenge to the tremendous potential of submicrometer pore- and nanopore-based sensing. We hope that this chapter provides some of the relevant parameters that may be helpful for realizing this potential.

5.7. Materials and Methods

Solutions. We prepared all solutions with deionized water (resistivity of 18.2 MΩ cm, Millipore, Billerica, MA), and we used all chemicals without further purification, including: potassium chloride, sulfuric acid (both from EMD Biosciences, La Jolla, CA), bovine serum albumin, Triton X-100 (both from Sigma Chemical Company, St Louis, MO), tris(hydroxymethyl)aminomethane (TRIS, Shelton Scientific, Shelton, CT), potassium phosphate – monobasic, potassium phosphate – dibasic (both from J.T. Baker, Phillipsburg, NJ), hydrochloric acid (VWR International, West Chester, PA), nitric acid (Fluka Chemie, Buchs, Switzerland), and hydrogen peroxide (EMD Chemicals, Gibbstown, NJ). Recording buffer for the noise measurements, which consisted of either 0.15 M KCl with 0.01 M phosphate buffer pH 7.3 and 0.1% w/v Triton X-100 or 1.00 M KCl with 0.01 M phosphate buffer pH 7.3 and 0.1% w/v Triton X-100, was filtered through sterile 0.1 or 0.2 μm polyethersulfone membrane filters (both from Pall, East Hills, NY). Recording buffer for the virus experiment, which consisted of 0.15 M KCl with 0.05 M tris(hydroxymethyl)aminomethane (TRIS) buffer pH 7.8 and 0.1 mg mL-1 bovine serum albumin as well as 0.1% w/v Tween 20, was filtered through sterile 0.2 μm polyethersulfone membrane filters.

Pore fabrication and imaging. We fabricated glass pores with conical geometry using a femtosecond-pulsed laser as described previously (Chapters 2 and 3). Briefly, we attached a glass coverslide (Corning 0211 borosilicate, Fisher Scientific, Pittsburgh, PA) to a 3-axes microscope nanomanipulation stage (Mad City Labs, Inc., Madison, WI), and placed a droplet of water on the area that was to be machined. For laser-based ablation of the glass at defined locations, we focused a directly diode-pumped Nd:glass CPA laser system (Intralase Corp., Irvine, CA) through a 100× oil immersion microscope objective (N.A. = 1.3, Zeiss, Thornwood, NY), and used laser pulses that were frequency doubled from 1053 nm to 527 nm with a duration of 600-800 fs (129,130,132,166). To fabricate the pore, we used a three-stage machining process that employed different pulse energy and repetition rates for the cylindrical shank that was 35 μm wide, top of the cone, and tip of the cone. Polyethylene terephthalate (PET) pores with cylindrical geometry and with diameters ranging from 10 – 610 nm were kindly provided by Professor Zuzanna S. Siwy, University of Irvine, CA; we used these pores without further cleaning or treatment.

After fabrication, we coated the glass pores in gold (thickness ~10 nm) using a sputter coater (Structure Probe Incorporated, West Chester, PA) and imaged them with a high resolution scanning electron microscope (HRSEM, FEI Company NOVA 200 Nanolab, Hillsboro, OR). Before using these pores for experiments, we removed the gold layer by etching in a 3:1 (vol/vol) mixture of fuming nitric acid and concentrated hydrochloric acid. In some cases, we reduced the diameters of the glass pores by depositing silicon dioxide at 380° C using plasma enhanced chemical vapor deposition (PECVD, Group Sciences Inc, San Jose, CA). The deposition time varied from pore to pore but was always less than 60 s. Before each experiment, we cleaned the glass pores in a fresh 3:1 (vol/vol) mixture of concentrated sulfuric acid with 30% hydrogen peroxide for at least 15 minutes.

Data acquisition. To assemble the recording setup, we placed the glass substrate with the pore or the PET substrate with the pore on a fluidic channel in poly(dimethylsiloxane) (PDMS, Sylgard 184 Silicone, Dow Corning, Midland, MI) (92,93). We used a fresh film of PDMS (thickness ~ 1 mm) with a hole in the center (diameter ~ 3.6 mm) to confine the electrolyte (recording buffer) in the top liquid compartment as shown in Figure 5.11. In order to guarantee reliable recording conditions while measuring the wide range of currents ($10^{-9} – 10^{-12}$ A) in the experiments, we used Ag/AgCl pellet electrodes (Eastern Scientific, Rockville, MD). For recording currents at constant voltage, we used a patch clamp amplifier (Axopatch 200B, Molecular Devices, Sunnyvale, CA) in voltage clamp mode with a gain of $\alpha = 0.5$, and with the built in, four- pole, analog low-pass Bessel filter set to a cutoff frequency of 100 kHz unless otherwise specified in the text. A low-noise digitizer (Digidata 1322, Molecular Devices) performed analog to digital data conversion with a sampling frequency f_s of 500 kHz and we stored the data on a computer using recording software (Clampex 9.2, Molecular Devices).

Data processing. We used the digital Gaussian low-pass filter provided with the Clampfit 9.2 software (Molecular Devices) with cut-off frequencies as specified in the text. This digital filter was always applied to the original current traces (not to previously digitally filtered traces). We calculated noise power spectra using Clampfit 9.2 software. In order to measure root-mean-square (RMS) values of the noise, we calculated the standard deviation of a current trace containing 50 ms of data (25,000

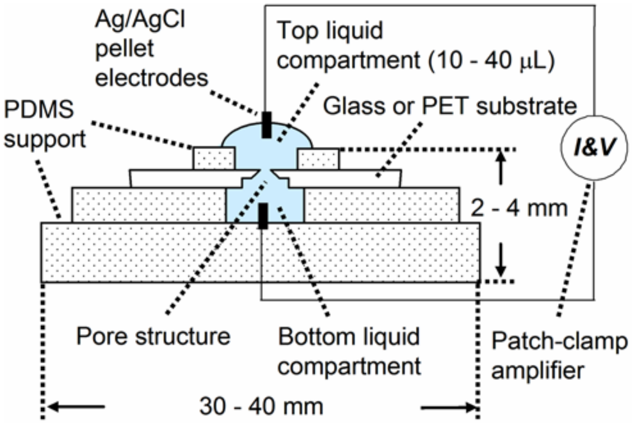

Figure 5.11. Sideview of the recording setup used for the experiments presented here (92,93).

samples). We analyzed the noise data and performed all fitting operations using Origin 7.5 software (OriginLab, Northampton, MA). Theoretical calculations of the noise were performed using custom Matlab programs (The Mathworks, Natick, MA).

Recording resistive-pulses from virus particles. We followed the procedure described previously (Chapter III) to monitor resistive-pulses from virus particles. Briefly, we diluted concentrated Paramecium Busaria Chlorella Virus (PBCV-1), kindly provided by J. L. Van Etten, University of Nebraska-Lincoln, Lincoln, NE, in the recording buffer for the virus experiments to a final concentration of ~$5 \cdot 10^8$ particles mL^{-1}. We then recorded resistive-pulses from virus particles passing through a glass pore with conical geometry and a diameter of ~ 650 nm under an applied potential of 0.2 V.

Measurement of the signal bandwidth of the recording electronics. In order to measure the signal bandwidth of the recording electronics (headstage, patch-clamp amplifier, analog low-pass filter, and digitizer), we used a high-quality function generator

(Agilent 33220A, Agilent Technologies, Santa Clara, CA) to create a 2 kHz triangle waveform with a transition time from positive to negative slope of less than 0.5 μs. We then brought the two terminals of the function generator (signal and ground) within a few centimeters of the headstage and the ground input (or to the Ag-AgCl electrodes that were connected to these pins when the device was loaded with a glass or PET pore). The air gap between these components acted as a capacitor, and the current I flowing through a capacitor with a capacitance C is the time derivative of the input waveform of the voltage V ($I = C \times \mathrm{d}V/\mathrm{d}t$). Thus the input pins (or the electrodes connected to these pins) sensed a square wave with the same frequency as the triangle wave.

With this setup, we were able to measure the 10-90% risetime $t_{10\text{-}90}$ of the recording electronics (*i.e.* the time it took for the recorded square wave to go from 10% of its final value to 90% of its final value). This $t_{10\text{-}90}$ risetime could be combined with Eq. 5.2 to calculate the signal bandwidth of the recording electronics (176,205). We used the same technique to determine the signal bandwidth of the recording electronics after "loading" the setup (*i.e.* after mounting a pore in the fluidic setup and immersing the electrodes in the two electrolyte compartments which were separated by a glass or PET substrate that contained a pore). We also used this capacitive coupling method to determine the signal bandwidth of the combination of the recording electronics with low-pass digital Gaussian filters by measuring the $t_{10\text{-}90}$ risetime of the square wave after it was digitally filtered.

5.8. Acknowledgements

This material is based upon work supported by a National Science Foundation CAREER Award (M.M., grant No. 0449088) and by a research grant from IMRA America and AISIN USA. The authors thank Alan J. Hunt and Zuzanna S. Siwy for providing synthetic membranes that contained a single submicrometer pore or nanopore. The authors also thank Toni Figl, Ken Healy, Ralph M. M. Smeets, Daniel J. Estes and Vincent Tabard-Cossa for valuable discussions.

CHAPTER 5 APPENDICES

5.A. Detailed Theoretical Analysis of the Thermal Current Noise of Cylindrical Pores and Conical Pores

As discussed in the main text, the thermal noise of the pore structures we used can be modeled, to a first approximation, using simple thermal noise equations (Eqs. 5.6 and 5.7); however, if the capacitance of the substrate is large (≥ 100 pF), or the resistance of the pore is large (≥ 100 MΩ), or the resistance leading to and from the pore is large (≥ 500 Ωs), Eqs. 5.6 and 5.7 may no longer describe the thermal noise of the pore. In this case, it may be more accurate to derive the theoretical thermal noise of the pore structures from an equivalent circuit of the pore structure (147). Since submicrometer pore and nanopore structures are usually fabricated in dielectric materials, the equivalent circuit of the pores is often a linear network of resistive and capacitive components. For the cylindrical PET pores and the conical glass pores we used here, the equivalent circuits are shown in Figure 5.2 of the main text and in Figure 5.A.1 here (these two figures are identical and we provide a copy here for convenience).

Once the equivalent circuit of the pore is known, it may be possible to calculate the total admittance Y of the circuit (admittance is the inverse of the impedance Z). Using the admittance, the power spectral density of the thermal current noise of a linear circuit $S_T^2(f)$ ($\mathrm{A^2\,Hz^{-1}}$) can be calculated with the following equation (147):

$$S_T^2(f) = |Y|^2 S_{TV}^2(f), \tag{5.A.1}$$

where $S_{TV}^2(f)$ is the power spectra density of the thermal voltage noise of the network. The power spectral density of the thermal voltage noise $S_{TV}^2(f)$ is given by the following equation (147):

$$S_{TV}^2(f) = 4kT\,\mathrm{Re}\{1/Y\}, \tag{5.A.2}$$

where k is Boltzmann's constant, $1.38\cdot10^{-23}$ m^2 kg s^{-2} K^{-1}, and T (K) is the temperature. Combining Eqs. 5.A.1 and 5.A.2, the power spectral density of the thermal current noise $S_T^2(f)$ can be written as:

$$S_T^2(f) = |Y|^2\,4kT\,\mathrm{Re}\{1/Y\} = 4kT\,\mathrm{Re}\{Y\}. \tag{5.A.3}$$

With Eq. 5.A.3, it is possible to calculate the thermal current noise $S_T^2(f)$ for the cylindrical and conical pores we used (shown in Figure 5.A.1).

Derivation of the thermal noise equation for a simple cylindrical pore:

We will begin by examining the cylindrical PET pores since the equivalent circuit for this geometry is simpler than the equivalent circuit for the conical glass pores. The admittance of the circuit can be written as:

$$\begin{aligned} Y_{Cyl} &= \frac{1}{Z_{Cyl}} = \frac{1}{R_a + \dfrac{R_p}{1 + j2\pi f C_s R_p}} \\ &= \frac{4\pi^2 f^2 C_s^2 R_p^2 R_a + (R_a + R_p)}{4\pi^2 f^2 C_s^2 R_p^2 R_a^2 + (R_a + R_p)^2} + j\frac{2\pi f C_s R_p^2}{4\pi^2 f^2 C_s^2 R_p^2 R_a^2 + (R_a + R_p)^2}, \end{aligned} \tag{5.A.4}$$

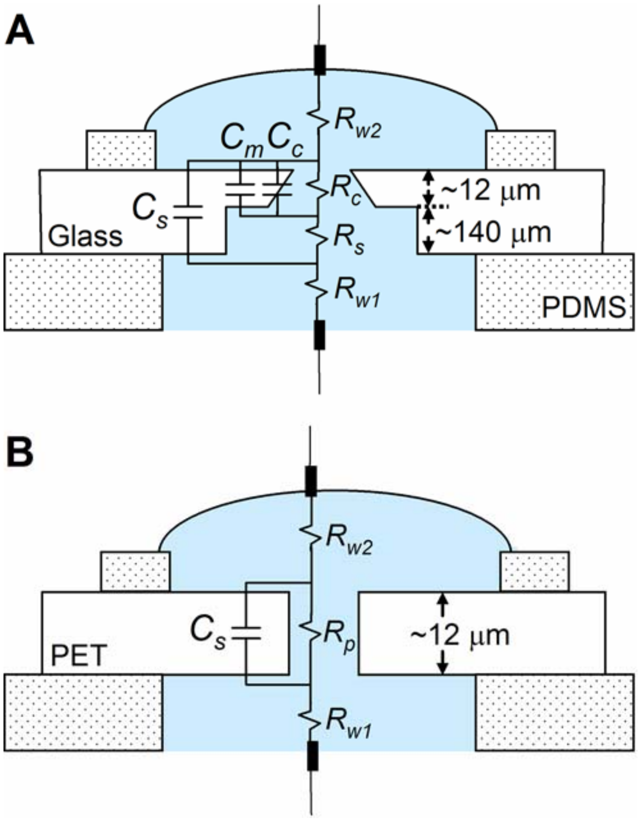

Figure 5.A.1. Model circuits of the pores used in this work. A) Model circuit of glass pores with conical geometry. R_{w1} and R_{w2} (Ω) are the resistance of the fluidic channels leading to the glass substrate, R_s (Ω) is the resistance of the 35 μm wide cylindrical shank, C_s (F) is the capacitance of the substrate supporting the glass membrane with the pore, R_c (Ω) is the total resistance of the conical part of the pore structure, C_c (F) is the total capacitance of the conical part of the pore structure, and C_m (F) is the capacitance of the glass membrane in which the pore is fabricated. B) Model circuit of PET pores with cylindrical geometry. R_p (Ω) is the resistance of the pore. The model circuits shown above do not include the resistance or capacitance of the electrodes since these parameters are not expected to affect significantly the thermal noise characteristics of the pore.

where $R_a = R_{w1} + R_{w2}$ (Ω) and all other parameters are as defined in Figure 5.A.1B.

Therefore, the PSD of the thermal current noise $S_{T-Cyl}^2(f)$ is

$$S_{T-Cyl}^2(f) = 4kT\left(\frac{4\pi^2 f^2 C_s^2 R_p^2 R_a + (R_a + R_p)}{4\pi^2 f^2 C_s^2 R_p^2 R_a^2 + (R_a + R_p)^2}\right), \tag{5.A.5}$$

and the RMS value of the thermal current noise $I_{T\text{-}Cyl}(f_c)$ (A RMS) is

$$I_{T-Cyl}(f_c)=\sqrt{4kT\left(\frac{c_1 f_c}{R_a}+\frac{\tan^{-1}\left(\frac{2\pi c_1 f_c C_s R_a R_p}{R_a+R_p}\right)}{2\pi C_S R_a^2}\right)}. \quad (5.A.6)$$

From Eq. 5.A.5, it is easy to see that in the limit $R_a \rightarrow 0$, $S_{T-Cyl}^2 = 4kT/R_p$ as expected.

We performed a detailed comparison of Eq. 5.7 and Eq. 5.A.6, and found that the two equations showed an increased divergence when either the resistance of the pores or the signal bandwidth increased (assuming that R_a and C_s remained constant) as shown in Figure 5.A.2. For the PET pore with the highest resistance we examined (R_p = 4 GΩ, R_a = 350 Ω, C_s = 30 pF) and a signal bandwidth of 40 kHz, Eq. 5.7 gave a value of 0.4 pA RMS while Eq. 5.A.6 gave a value of 2.1 pA RMS (in contrast, for a pore with R_p = 50 MΩ, Eq. 5.7 gave a value of 3.6 pA RMS and Eq. 5.A.6 gave a value of 4.2 pA RMS). Therefore the theoretical equation we used in the main text was off by at most a factor of approximately 5 for the PET pores.

While this is error is considerable, we decided to use Eq. 5.7 in the main text for the following four reasons. First, we believe that Eq. 5.7 will in yield a reasonable prediction of the thermal noise of many submicrometer pore and nanopore structures. Second, modeling the pore as a linear network of resistors and capacitors is itself an approximation and deriving the admittance of a given pore structure can be difficult. Third, for the recording system and PET pores considered here, Eq. 5.7 and Eq. 5.A.6 diverged only in the most extreme cases (pores with resistances of GΩ and signal

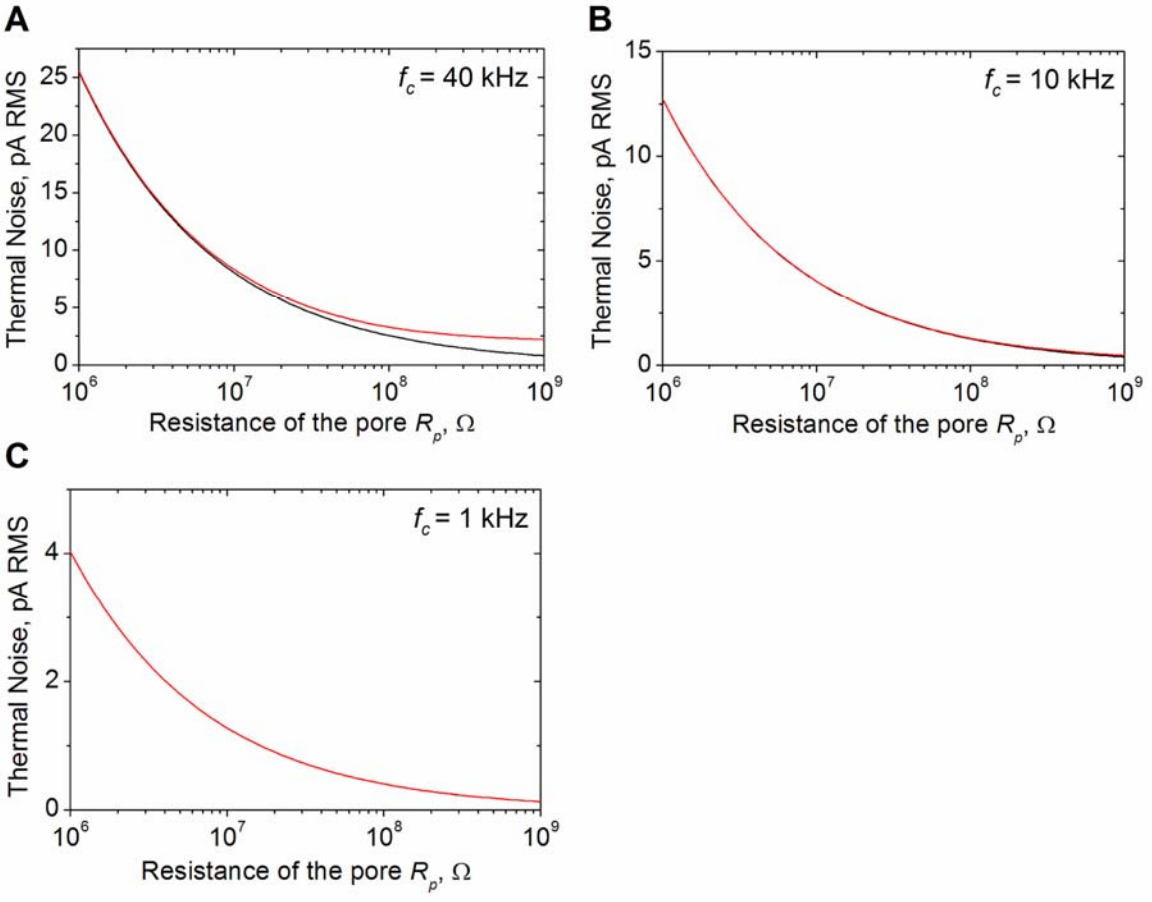

Figure 5.A.2. Comparison of the thermal noise predicted by Eq. 5.7 in the main text (black line) and Eq. 5.A.6 (red line) with a signal bandwidth of 40 kHz (graph A), 10 kHz (graph B) and 1 kHz (graph C). For these graphs, R_a was 350 Ω (*i.e.* the buffer was 1.00 M KCl with 0.01 M phosphate buffer pH 7.3 and 0.1% w/v Triton X-100) and C_s was 30 pF. We used $R = R_p + R_a$ for Eq. 5.7.

bandwidths greater than 10 kHz); many researchers do not operate in these extreme cases. Fourth, as shown below, the more accurate thermal noise equation that we derived for the conical glass pores also only displayed a significant divergence from Eq. 5.7 in extreme cases (none of the glass pores we examined in this report fell under the category of extreme cases). Hence for clarity and to make it easier for researchers to obtain a good estimate of the noise for most cases, we choose to use Eq. 5.7

Derivation of the thermal noise equation for the conical pores:

We now examine the theoretical thermal current noise for the conical glass pores $S_{T-Con}^{2}(f)$ shown in Figure 5.A.1A. Since the circuit is relatively complex and the equations lengthy, we do not provide here the derivation of the following power spectral density:

$$S_{T-Con}^{2}(f)= \tag{5.A.7}$$

$$4kT\frac{4\pi^2C_M^2f^2R_c^2\left(4\pi^2C_s^2f^2R_aR_s^2+R_a+R_s\right)+8\pi^2C_sC_Mf^2R_aR_c^2+4\pi^2C_s^2f^2R_a\left(R_c+R_s\right)^2+R_a+R_c+R_s}{4\pi^2C_M^2f^2R_c^2\left(4\pi^2C_s^2f^2R_a^2R_s^2+\left(R_a+R_s\right)^2\right)+8\pi^2C_sC_Mf^2R_a^2R_c^2+4\pi^2C_s^2f^2R_a^2\left(R_c+R_s\right)^2+\left(R_a+R_c+R_s\right)^2}$$

where $C_M=C_m+C_c$, $R_a=R_{w1}+R_{w2}$ and all other parameters are as defined in Figure 5.A.1A (this derivation ignores the distributed nature of the resistance of the cone R_c and the capacitance of the cone C_c). In order to calculate the RMS thermal current noise of the glass pores $I_{T\text{-}Con}(f_c)$, the above equation should be integrated from 0 to f_c (the signal bandwidth) with respect to f; however, the analytical expression that results from this integration is exceptionally long so we do not provide it here. Using this analytical expression also required long calculation times on the computers that were available, so we instead calculated RMS values by numerically integrating Eq. 5.A.7.

We performed a detailed comparison of the values given by numerical integration of Eq. 5.A.7 and the values given by Eq. 5.7, and we found that the two showed small differences that were dependent on the resistance of the cone R_c and on the signal bandwidth (assuming that R_a, R_s, C_s, and C_M remained constant) as shown in Figure 5.A.3. For the glass pore we examined in this report, the difference between the two equations was always smaller than 6%. Thus it was possible to use Eq. 5.7 as the thermal

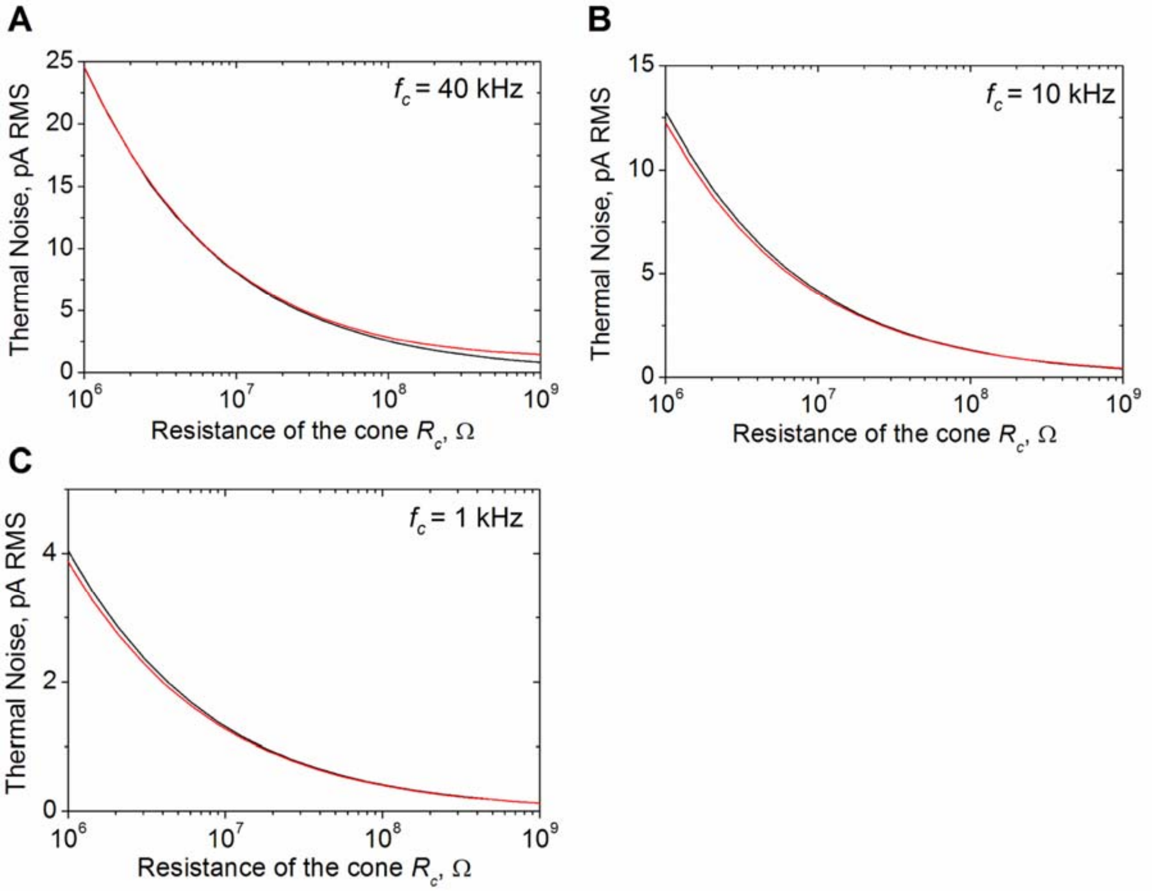

Figure 5.A.3. Comparison of the thermal noise predicted by Eq. 5.7 in the main text (black line) and the numerical integration of Eq. 5.A.7 (red line) with a signal bandwidth of 40 kHz (graph A), 10 kHz (graph B) and 1 kHz (graph C). For these graphs, R_a was 1200 Ω, R_s was 80,000 Ω (*i.e.* the buffer was 0.15 M KCl with 0.01 M phosphate buffer pH 7.3 and 0.1% w/v Triton X-100) C_s was 10 pF, and C_M was 7 fF. We used $R = R_c + R_s + R_a$ for Eq. 5.7.

noise equation in the theoretical calculations of the total noise of the glass pores without adding a significant error to the prediction of the total noise.

In summary, we believe that the simple thermal noise equations provided in the main text (Eqs. 5.6 and 5.7) will yield a good first approximation of the thermal noise of the pore structures that are used by many researchers. There are cases, however, when the simple thermal noise equations will provide values considerably different from the thermal noise equations derived from the model circuit of the pore structure. In general, if the capacitance of the substrate is large (≥ 100 pF), the resistance of the pore is large (≥ 100 MΩ), or the resistance leading to and from the pore is large (≥ 500 Ω), there may be a significant divergence between the simple equations provided in the main text and the equations derived here. For the scenarios we examined in the main text, the simple RMS noise equation and the derived RMS noise equation were in relatively good agreement in all cases except for PET pores with resistances greater than ~100 MΩ at signal bandwidths greater than ~40 kHz. Even for these exceptions, the overall difference in the predicted total RMS noise used in the main text was minimal since the thermal noise was not the dominant source of noise.

CHAPTER 6

SUMMARY AND SUGGESTIONS FOR FUTURE RESEARCH

Previous work has revealed that resistive-pulse sensing is a simple, yet powerful technique for the detection and characterization of discrete micro- or nano-scale objects. In this thesis, we described a new application for resistive-pulse sensing, namely *in situ* detection and characterization of the formation of biological nanoassemblies (immune complexes, antibody-virus complexes). Due to its central importance for resistive-pulse measurements, we also provided the first comprehensive discussion of the noise and signal bandwidth of the experimental setups.

6.1. Summary of Chapter 2

In Chapter 2, we used resistive-pulse sensing to detect and characterize the formation of biological nanoassemblies which consisted of antibodies and antigens (immune complexes). The assay was rapid, label-free, required no immobilization or modification of the antibody or antigen, and was performed in volumes ≤ 40 μL. To fabricate the submicrometer pores required for the experiments, we adopted a recently developed nanofabrication technique based on a femtosecond-pulsed laser; this technique made it possible to fabricate pores with conical geometry and with diameters as small as 575 nm. With these pores, we were able to sense immune complexes which consisted of

610 – 17,300 proteins, and we were able to detect purified proteins at concentrations as low as 30 nM. The resistive-pulse technique enabled the monitoring of the passage of individual immune complexes, which provided a true volume-distribution of the complexes and allowed for following the growth and polydispersity of these complexes. This method sensed immune complexes in solution, and we showed that the antibody or antigen could be present in complex media such as serum. This work was the first demonstration of a resistive-pulse based immunoassay that required no immobilization of the antibody or antigen; the simplicity of this assay (*i.e.* simply mixing of the antibody and antigen in solution is required) combined with the small footprint of the device makes it attractive for portable or high throughput immunoassays for diagnostics and biodefense.

6.2. Summary of Chapter 3

In Chapter 3, we used resistive-pulse sensing for detecting and characterizing the formation of biological nanoassemblies from antibodies and viruses. The assay was label-free, examined the non-pathogenic, icosahedrical Paramecium Busaria Chlorella Virus (PBCV-1) in its native, assembled state, and required no immobilization or modification of the virus or antibody. Before examining virus-antibody interactions, we characterized the size of PBCV-1 virions using resistive-pulse sensing; we measured a diameter of 203 ± 14 nm along the fivefold axes, which compared well with the average diameter of 190 nm measured with cryoelectron microscopy (149). Since resistive-pulse sensing provided a continuous measurement of the sample, we were able to monitor quantitatively the time-course of binding of an antibody in rabbit serum to PBCV-1. We found that the maximum number of antibodies that were able to bind to PBCV-1 was 4200 ± 450. This work constitutes the first demonstration of using resistive-pulse sensing to monitor antibody-virus interactions, and the method we described could be used to i) detect a specific virus or a virus-specific antibody in solution, ii) probe the ability of an antibody to immunoprecipitate the virus, iii) determine the number of antibodies bound to individual virus particles, and iv) monitor the assembly of nanoparticles onto templates (here antibodies onto viruses) *in situ*. Finally, due to the small footprint and the simple detection scheme, resistive-pulse sensing based detection of antibody-virus interactions may also provide a simple technique for portable or high throughput immunoassays with applications in clinical laboratories (*e.g.* vaccine development) or biodefense.

6.3. Summary of Chapter 4

In Chapter 4, we described a method for estimating the solid phase affinity constant of antibodies by using resistive-pulse data from spherical nanoparticles that expose antigens. We developed this technique by analyzing data published recently by Saleh *et al*. (90). These authors used resistive-pulse sensing to detect an increase in the diameter of streptavidin-functionalized colloids due to the binding of monoclonal anti-streptavidin antibodies. Based on further analysis of the data presented by Saleh *et al.*, we were able to determine the number of antibodies bound to the colloids at various antibody concentrations. This information made it possible to estimate the solid phase affinity constant of the interaction by fitting the data with a thermodynamic model that described the binding equilibrium between antibody and antigen binding. We calculated a value of $2.6 \cdot 10^8 \pm 0.8 \cdot 10^8$ M^{-1} for the solid phase affinity constant which is in agreement with the specifications of the supplier of the antibody. This chapter thus demonstrated that resistive-pulse sensing can be used to extract thermodynamic parameters of antibody-antigen interactions (61), and may therefore be useful for studying the thermodynamic parameters governing the interactions of synthetic objects such as nanoparticles attaching to templates (6) or viruses (12).

6.4. Summary of Chapter 5

In Chapter 5, we presented a detailed study on the noise and signal bandwidth of current recordings from glass and polyethylene terephthalate (PET) membranes that contained a single submicrometer pore or nanopore. We examined the theoretical signal bandwidth of two different pore geometries, and we measured the signal bandwidth of the electronics used to record the ionic current. We also investigated the theoretical noise generated by the substrate material, the pore, and the electronics used to record the current. Employing a combination of theory and experimental results, we were able to predict the noise in current traces recorded from glass and PET pores with no applied voltage with a maximum error of 12% in a range of signal bandwidths from 1 – 40 kHz. In many experiments, application of a voltage did not significantly increase the noise. In some cases, however, application of a voltage resulted in an additional source of noise. For these pores, predictions of the noise were typically still accurate within 35% error. The power spectra of this extra noise suggested a $1/f^{\alpha}$ origin with best fits to the power spectrum for $\alpha = 0.4 - 0.8$. Based on the detailed discussion of the noise and signal bandwidth characteristics of recordings from submicrometer pores and nanopores, we provided recommendations for reducing the noise generated by the various sources allowing recordings at high signal bandwidth (> 10 kHz), which increases the information content and accuracy of the current recordings.

6.5. Conclusions and Suggestions for Future Research

The material from Chapters 2 – 5 provides exciting new directions for original research in a wide range of fields such as biomedical engineering, chemical engineering, chemistry, virology, biology, and nanotechnology. Here, we describe these ideas, and summarize them at the end of this section in Table 6.1.

The first area of interest is the continuation of the work from Chapter 2 (detection of antibody-antigen complexes). While this research demonstrated that it was possible to detect purified proteins (antigens) at concentrations as low as 30 nM, we believe that this limit could be pushed to considerably lower concentrations, at least by an order of magnitude and perhaps more. There are two simple methods for reducing the detection limit: reducing the diameter of the pore or modifying the antibody-antigen ratio. Reducing the diameter of the pore will enable the detection of smaller immune complexes, which should enable detection of lower concentrations of protein. In the limit of a very small pore (tens of nanometers), it may be possible to detect individual antigens binding to individual antibodies. In this case, it may be better to use a monoclonal antibody as opposed to a polyclonal antibody since monoclonal antibodies possess a single affinity constant. On the other hand, it may be interesting to examine the binding of a polyclonal antibody to its antigen since polyclonal antibodies have a range of affinities.

The antibody-antigen ratio used in almost all of the experiments from chapter two was 1:1; this ratio is not always ideal for the formation of large immune complexes. The ideal ratio is determined by the number of accessible epitopes (sites to which the antibody can bind) on the antigen. That is, if there were ten (accessible) epitopes on the antigen, the ideal ratio of antibody to antigen would be 5:1 (in the case of IgG antibodies with two binding sites). By combining the two recommendations presented here, it should be straightforward to obtain an order of magnitude decrease in the antigen detection limit. Indeed, we believe it will possible to achieve antigen detection limits below 100 pM. Such a low detection limit would be excellent when compared to the 10 – 1000 nM detection limit of other label-free techniques that require no immobilization of the antigen such as affinity capillary electrophoresis (ACE), gel-based immunoprecipitation, and direct immunoaggregation assays based on light-scattering (142-144).

The work from Chapter 2 demonstrates that resistive-pulse sensing is able to detect and monitor the formation of immune complexes, which are nanoassemblies composed of hundreds or thousands of nano-sized objects (here protein particles). These experiments provide the inspiration for a number of new resistive-pulse sensing studies that examine the formation of other nanoassemblies, both biological and synthetic.

In the category of biological nanoassemblies, we propose this technique could be used for the rapid detection of cryoglobulins. Cryoglobulins (CGs) are “abnormal” blood proteins, which owe their name to the unusual property that they form aggregates when blood serum from affected patients is cooled below body temperature (232,233). Current clinical testing for CGs requires 5-10 mL of serum, typically takes 3-7 days, uses the unaided human eye for detection, and requires expertise to avoid loss or contamination of the CGs (234). Adapting the assay from Chapter 2 may lower the required volume of serum to below 100 μL, reduce the wait time to less than 6 hours, and enable the automated detection of cryoglobulins.

In the category of synthetic nanoassemblies, we propose pore-based sensing could be used for monitoring and characterizing the formation of nanoparticle assemblies (4-6,8,9,13,235). Currently, there is no technique available that can accomplish the information rich, *in-situ*, solution-based monitoring of the formation of nanoparticle assemblies. The closest technique is dynamic light scattering (DLS); however, DLS measures multiple interactions at once and is unable to provide a true histogram of the volume of the assemblies. Resistive-pulse sensing measures each assembly individually and is thus able to provide a true histogram of the volume of the assemblies (and thus potentially the number of objects in the assembly). In addition to this level of detail, resistive-pulse sensing is a rapid technique since it can measure a few hundred assemblies within one minute. Resistive-pulse sensing would therefore be an excellent technique for monitoring and characterizing the formation of nanoparticle assemblies. This technique may thus be able to address an urgent need in nanotechnology.

Chapter 3 of this thesis focused on examining antibody-virus interactions and the results of this work provide the foundation for two separate research directions. Both of these paths make use of the theoretical work presented in Chapter 4, so we discuss future work for that chapter here as well. First, resistive-pulse sensing could be used to characterize other antibody-virus combinations; future experiments may use antibodies that are known to not aggregate the virus (151,155,158,159,236-238) and could examine in detail the kinetics of the antibody-virus interaction. Combining this data with the theory presented in Chapter 4 may enable the calculation of the solid-phase affinity constant of an unlabeled, monoclonal antibody for its antigen as it is natively presented by a virus particle. Finally, we also think it should be possible to use this technique to determine how effectively an antibody aggregates a virus. The data obtained from resistive-pulse sensing experiments may therefore be useful for the development of vaccines or possibly antiviral drugs, both of which are growing areas of interest in this era of globalization. This technique may also be useful for development of antibody-based therapies such as immunotherapy against cancer.

The second research path suggested by Chapter 3 is the study of nanoparticle template interactions. There is a growing inteerest in forming nanoassemblies which consist of small particles (roughly 1 – 50 nm, synthetic or biological) binding to larger particles (roughly 20 – 500 nm, synthetic or biological) (1-4,6,12,239). Based on the research demonstrated in Chapters 3 and 4, it should be possible to monitor *in-situ* the formation of these nanoassemblies, determine the number of small particles binding to the larger particles, estimate an average affinity constant of the small particle-large particle interaction, and study the kinetics of the small particle-large particle interaction. We therefore believe that a combination of the technique presented in Chapter 3 with the theory of Chapter 4 is a promising way to study the formation of these nanoassemblies.

The final future research suggestions arise from the work discussed in Chapter 5. While the theoretical component of this study was exceptionally detailed, we only examined the signal bandwidth and noise of two substrate materials which had capacitances of 10-30 pF. Therefore a follow-up study that examined the signal bandwidth and noise of other substrate materials (such as silicon-based pores) with a wider range of capacitances (and perhaps series resistances) would be interesting and useful. This study could also examine how closely the pore structures match their equivalent circuit model; the electrochemical impedance spectra of the pores could be recorded using a lock-in amplifier (*e.g.* an SR 830, Stanford Research Systems, Sunnyvale, CA) and the equivalent circuit model could be fitted to this spectra.

Table 6.1. Summary of future research

Inspiration	Future research
Chapter 2	Use pore diameters below 300 nm and optimized antibody to antigen ratios to push the detection limit of purified antigens below 100 pM using purified antibodies. Determine the detection limit when the antigen, antibody, or both are present in serum.
Chapter 2	Study other biologically relevant forms of aggregation/assembly such as the formation of cryoglobulins (18,232,234,240) or the assembly of virus capsids.
Chapter 2	Monitor the aggregation/assembly of synthetic nanoparticles (*e.g.* semiconductor nanocrystals) (4-6,8,9,13,235)
Chapters 3 and 4	Examine the interaction of other virus particles with antibodies. Use antibodies which are known to not aggregate the virus (151,155,158,159,236-238) so that the pore never clogs with antibody-virus complexes. Attempt precise examination of the kinetics of antibody-virus interaction.
Chapters 3 and 4	Study the binding of nanoparticles (synthetic or biological) to templates (biological or synthetic) (1-4,6,12,239). For example, the binding of nanoparticles to viruses.
Chapter 5	Examine in detail the noise and bandwidth of current recordings from pores with a wide range of capacitances (approximately 10 pF – 1 nF) and series resistances (approximately 500 Ω - 1 MΩ). Use a lock-in amplifier to study the electrochemical impedance spectra of various pore structures and fit the equivalent circuit model of the pore to the spectra.

6.6. Concluding Remarks

While Wallace H. Coulter originally developed resistive-pulse sensing for counting cells, this technique has found numerous applications in a wide range of fields such as biology, biophysics, biomedical engineering, chemistry, and nanotechnology. The development of many of these new applications occurred in the last ten years. The rapid growth in the utilization of resistive-pulse sensing will likely continue due to its numerous advantages (Table 6.2) and since many of its disadvantages can be mitigated with appropriate measures or further research as discussed in Table 6.2. This author believes that in the future, the most powerful applications of resistive-pulse sensing will be the *in-situ* detection and characterization of biological, synthetic, or hybrid (assemblies formed from biological and synthetic components) nanoassemblies. For example, with integrated micro- or nanofluidics, resistive-pulse sensing could be used in highly-sensitive, disposable sensors for the detection of antigens or antibodies outside the laboratory. In the laboratory, resistive-pulse sensing could be used in the routine characterization of nanoassemblies thereby helping enable the development of the next generation of functional nanodevices. The experiments and results presented in this thesis provide some of the necessary background for developing these new resistive-pulse sensing based sensors.

Table 6.2. Advantages of restive-pulse sensing and challenges for increased utilization of this technique

Advantages	Challenges	Potential Solutions
Simple measurement (measuring a current under an applied voltage)	Need to measure picoamps or nanoamps of current	Use low-noise patch-clamp amplifier
Easily integrated with microfluidics and on-chip electronics	Limited range of sensitivity for a given pore (*i.e.* the geometry and diameter of a pore cannot be adjusted during an experiment)	Switch pores between experiments, develop a multiplexed assay that uses an array of pores with different diameters, or develop pores with tunable diameters
Able to provide results within minutes or hours	Pore may irreversibly clog during experiment	Filter solutions, build filters into integrated device, or coat pore in non-stick substance such as polyethylene glycol (PEG)
Able to provide simple detection and quantitative information of individual objects in solution	Can be difficult to obtain quantitative information on the sample of interest in the presence of other objects of similar volume	Remove other objects via filtration or use a label to identify the object of interest
Able to examine individual macromolecules or small molecules	Resistive-pulse sensing requires the use of conductive solutions so that a current can be measured	Ensure there are ions present in the solvent that can participate in redox chemistry compatible with the electrodes
Able to monitor *in-situ* the formation of nanoassemblies.	Measurement bandwidth limited by amplifier technology (current limit of ~50 kHz) therefore very fast changes in current cannot be resolved	Further research into development of high-bandwidth patch-clamp amplifiers with low-noise
Current fabrication techniques allow for pores with diameters ranging from 1 μm to 1 nm.	Can be difficult to mass-produce membranes with a single submicrometer pore or nanopore with well-defined geometry	Further research on fabrication techniques for membranes that contain a single submicrometer pore or nanopore

REFERENCES

1. Lee, J., A. O. Govorov, and N. A. Kotov. 2005. Nanoparticle assemblies with molecular springs: a nanoscale thermometer. *Angew. Chem. Int. Ed.* 44:7439-7442.

2. Lee, J., A. O. Govorov, and N. A. Kotov. 2005. Bioconjugated superstructures of CdTe nanowires and nanoparticles: multistep cascade Forster resonance energy transfer and energy channeling. *Nano Lett.* 5:2063-2069.

3. Lee, J., T. Javed, T. Skeini, A. O. Govorov, G. W. Bryant, and N. A. Kotov. 2006. Bioconjugated Ag nanoparticles and CdTe nanowires: metamaterials with field-enhanced light absorption. *Angew. Chem. Int. Ed.* 45:4819-4823.

4. Niemeyer, C. M. 2001. Nanoparticles, proteins, and nucleic acids: biotechnology meets materials science. *Angew. Chem. Int. Ed.* 40:4128-4158.

5. Hazarika, P., B. Ceyhan, and C. M. Niemeyer. 2004. Reversible switching of DNA-gold nanoparticle aggregation. *Angew. Chem. Int. Ed.* 43:6469-6471.

6. Tang, Z., and N. A. Kotov. 2005. One-dimensional assemblies of nanoparticles: preparation, properties, and promise. *Adv. Mater. (Weinheim, Fed. Repub. Ger.).* 17:951-962.

7. Tang, Z., Z. Zhang, Y. Wang, S. C. Glotzer, and N. A. Kotov. 2006. Self-assembly of CdTe nanocrystals into free-floating sheets. *Science.* 314:274-278.

8. Glotzer, S. C. 2004. Materials science. Some Assembly Required. *Science.* 306:419-420.

9. Glotzer, S. C., M. J. Solomon, and N. A. Kotov. 2004. Self-assembly: from nanoscale to microscale colloids. *AIChE J.* 50:2978-2985.

10. Horsch, M. A., Z. Zhang, and S. C. Glotzer. 2006. Self-assembly of laterally-tethered nanorods. *Nano Lett.* 6:2406-2413.

11. Wang, L., and W. Tan. 2006. Multicolor FRET silica nanoparticles by single wavelength excitation. *Nano Lett.* 6:84-88.

12. Radloff, C., and R. A. Vaia. 2005. Metal nanoshell assembly on a virus bioscaffold. *Nano Lett.* 5:1187-1191.

13. Maye, M. M., I. S. Lim, J. Luo, Z. Rab, D. Rabinovich, T. Liu, and C. Zhong. 2005. Mediator-template assembly of Nanoparticles. *J. Am. Chem. Soc.* 127:1519-1529.

14. Khlebtsov, B. N., G. L. Burygin, L. Y. Matora, S. Y. Shchygolev, and N. G. Khlebotsov. 2004. A method for studying insoluble immune complexes. *Biochim. Biophys. Acta.* 1670:199-207.

15. Murphy, R. M., R. A. Chamberlin, P. Schurtenberger, C. K. Colton, and M. L. Yarmush. 1990. Size and structure of antigen-antibody complexes: thermodynamic parameters. *Biochemistry.* 29:10889-10899.

16. Murphy, R. M., H. Slayter, P. Schurtenberger, R. A. Chamberlin, C. K. Colton, and M. L. Yarmush. 1988. Size and structure of antigen-antibody complexes: electron microscopy and light scattering studies. *Biophys. J.* 54:45-56.

17. Gorgani, N. N., S. B. Easterbrook-Smith, and J. G. Altin. 1996. The formation of insoluble immune complexes between ovalbumin and anti-ovalbumin IgG occurs in at least two distinct phases dependent on reactant concentration and ionic strength. *Biochim. Biophys. Acta.* 1317:45-54.

18. Di Stasio, E., P. Bizzarri, M. Bove, M. Casato, B. Giardina, M. Fiorilli, A. Galtieri, and L. P. Pucillo. 2003. Analysis of the dynamics of cryoaggregation by light-scattering spectrometry. *Clin. Chem. Lab. Med.* 41:152-158.

19. http://www.merckmedicus.com/pp/us/hcp/diseasemodules/hpvd/default.jsp

20. Coulter, W. H. High speed automatic blood cell counter and cell size analyzer; 1956; Chicago, IL. p 1034-1040.

21. http://www.whcf.org/WHCF_WallaceHCoulter.htm

22. Kubitschek, H. E. 1958. Electronic counting and sizing of bacteria. *Nature.* 182:234-235.

23. Gregg, E. C., and K. D. Steidley. 1965. Electrical counting and sizing of mammalian cells in suspension. *Biophys. J.* 5:393-405.

24. DeBlois, R. W., and C. P. Bean. 1970. Counting and sizing of submicron particles by the resistive pulse technique. *Rev. Sci. Instrum.* 41:909-916.

25. Anderson, J. L., and J. A. Quinn. 1971. The relationship between particle size and signal in Coulter-type counters. *Rev. Sci. Instrum.* 42:1257-1258.

26. DeBlois, R. W., C. P. Bean, and R. K. A. Wesley. 1977. Electrokinetic measurements with submicron particles and pores by the resistive pulse technique. *J. Colloid Interface Sci.* 61:323-335.

27. Ito, T., L. Sun, and R. M. Crooks. 2003. Simultaneous determination of the size and surface charge of individual nanoparticles using a carbon nanotube-based coulter counter. *Anal. Chem.* 75:2399-2406.

28. Saleh, O. A., and L. L. Sohn. 2001. Quantitative sensing of nanoscale colloids using a microchip Coulter counter. *Rev. Sci. Instrum.* 72:4449-4451.

29. DeBlois, R. W., and R. K. A. Wesley. 1977. Sizes and concentrations of several type C oncornaviruses and bacteriophage T2 by the resistive-pulse technique. *J. Virol.* 23:227-233.

30. DeBlois, R. W., E. E. Uzgiris, D. H. Cluxton, and H. M. Mazzone. 1978. Comparative measurements of size and polydispersity of several insect viruses. *Anal. Biochem.* 90:273-288.

31. Feuer, B. I., E. E. Uzgiris, R. W. Deblois, D. H. Cluxton, and J. Lenard. 1978. Length of glycoprotein spikes of vesicular stomatitis virus and sindbis virus, measured *in situ* using quasi elastic light scattering and a resisitve-pulse technique. *Virology.* 90:156-161.

32. von Schulthess, G. K., G. B. Benedek, and R. W. DeBlois. 1980. Measurement of the cluster size distributions for high functionality antigens cross-linked by antibody. *Macromolecules.* 13:939-945.

33. von Schulthess, G. K., G. B. Benedek, and R. W. DeBlois. 1983. Experimental measurements of the temporal evolution of cluster size distributions for high-functionality antigens cross-linked by antibody. *Macromolecules.* 16:434-440.

34. Pefferkorn, E., and R. Varoqui. 1989. Dynamics of latex aggregation - modes of cluster growth. *J. Chem. Phys.* 91:5679-5686.

35. Ouali, L., S. Stoll, E. Pefferkorn, A. Elaissari, V. Lanet, C. Pichot, and B. Mandrand. 1995. Coagulation of antibody-sensitized latexes in the presence of antigen. *Poly. Adv. Technol.* 6:541-546.

36. Bezrukov, S. M., and J. J. Kasianowicz. 2002. Dynamic partitioning of neutral polymers into a single ion channel. *In* Structure and Dynamics of Confined Polymers. J. J. Kasianowicz, M. S. Z. Kellermayer, and D. W. Deamer, editors. Kluwer Academic Publishers, Norwell, MA. 117-130.

37. Bezrukov, S. M., I. Vodyanoy, and V. A. Parsegian. 1994. Counting polymers moving through a single ion channel. *Nature.* 370:279-281.

38. Kasianowicz, J. J., E. Brandin, D. Branton, and D. W. Deamer. 1996. Characterization of individual polynucleotide molecules using a membrane channel. *Proc. Natl. Acad. Sci. U. S. A.* 93:13770-13773.

39. Deamer, D. W., and D. Branton. 2002. Characterization of nucleic acids by nanopore analysis. *Acc. Chem. Res.* 35:817-825.

40. Akeson, M., D. Branton, J. J. Kasianowicz, E. Brandin, and D. W. Deamer. 1999. Microsecond time-scale discrimination among polycytidylic acid, polyadenylic acid, and polyuridylic acid as homopolymers or as segments within single RNA molecules. *Biophys. J.* 77:3227-3233.

41. Bayley, H., and C. R. Martin. 2000. Resistive-pulse sensing - from microbes to molecules. *Chem. Rev.* 100:2575-2594.

42. Meller, A., L. Nivon, E. Brandin, J. Golovchenko, and D. Branton. 2000. Rapid nanopore discrimination between single polynucleotide molecules. *Proc. Natl. Acad. Sci. U. S. A.* 97:1079-1084.

43. Bayley, H., and P. S. Cremer. 2001. Stochastic sensors inspired by biology. *Nature (London).* 413:226-230.

44. Howorka, S., S. Cheley, and H. Bayley. 2001. Sequence-specific detection of individual DNA strands using engineered nanopores. *Nat. Biotechnol.* 19:636-639.

45. Howorka, S., L. Movileanu, O. Braha, and H. Bayley. 2001. Kinetics of duplex formation for individual DNA strands within a single protein nanopore. *Proc. Natl. Acad. Sci. U. S. A.* 98:12996-13001.

46. Meller, A., L. Nivon, and D. Branton. 2001. Voltage-driven DNA translocations through a nanopore. *Phys. Rev. Lett.* 86:3435-3438.

47. Vercoutere, W., S. Winters-Hilt, H. Olsen, D. Deamer, D. Haussler, and M. Akeson. 2001. Rapid discrimination among individual DNA hairpin molecules at single-nucleotide resolution using an ion channel. *Nat. Biotechnol.* 19:248-252.

48. Wang, H., and D. Branton. 2001. Nanopores with a spark for single-molecule detection. *Nat. Biotechnol.* 19:622-623.

49. Meller, A., and D. Branton. 2002. Single molecule measurements of DNA transport through a nanopore. *Electrophoresis.* 23:2583-2591.

50. Bates, M., M. Burns, and A. Meller. 2003. Dynamics of DNA molecules in a membrane channel probed by active control techniques. *Biophys. J.* 84:2366-2372.

51. Sauer-Budge, A. F., J. A. Nyamwanda, D. K. Lubensky, and D. Branton. 2003. Unzipping kinetics of double-stranded DNA in a nanopore. *Phys. Rev. Lett.* 90:238101.

52. Winters-Hilt, S., W. Vercoutere, V. S. DeGuzman, D. Deamer, M. Akeson, and D. Haussler. 2003. Highly accurate classification of Watson-Crick basepairs on termini of single DNA molecules. *Biophys. J.* 84:967-976.

53. Sánchez-Quesada, J., A. Saghatelian, S. Cheley, H. Bayley, and M. R. Ghadiri. 2004. Single DNA rotaxanes of a transmembrane protein. *Angew. Chem. Int. Ed.* 43:3063-3067.

54. Wang, H., J. E. Dunning, A. P.-H. Huang, J. A. Nyamwanda, and D. Branton. 2004. DNA heterogenity and phosporylation unveiled by single-molecule electrophoresis. *Proceedings of the National Academy of Sciences.* 101:13472-13477.

55. Xie, H., O. Braha, L. Gu, S. Cheley, and H. Bayley. 2005. Single-molecule observation of the catalytic subunit of cAMP-dependent protien kinase binding to an inhibitor peptide. *Chemistry & Biology.* 12:109-120.

56. Butler, T. Z., J. H. Gundlach, and M. A. Troll. 2006. Determination of RNA orientation during translocation through a biological nanopore. *Biophys. J.* 90:190-199.

57. Danelon, C., E. M. Nestorovich, M. Winterhalter, M. Ceccarelli, and S. M. Bezrukov. 2006. Interaction of zwitterionic penicillins with the OmpF channel facilitates their translocation. *Biophys. J.* 90:1617-1627.

58. Kullman, L., M. Winterhalter, and S. M. Bezrukov. 2002. Transport of maltodextrins through maltoporin: a single-channel study. *Biophys. J.* 82:803-812.

59. Berkane, E., F. Orlik, A. Charbit, C. Danelon, D. Fournier, R. Benz, and M. Winterhalter. 2005. Nanopores: maltoporin channel as a sensor for maltodextrin and lamda-phage. *J. Nanobiotechnology.* 3:3.

60. Gu, L., O. Braha, S. Conlan, S. Cheley, and H. Bayley. 1999. Stochastic sensing of organic analytes by a pore-forming protein containing a molecular adapter. *Nature.* 398:686-690.

61. Howorka, S., J. Nam, H. Bayley, and D. Kahne. 2004. Stochastic detection of monovalent and bivalent protein-ligand interactions. *Angew. Chem. Int. Ed.* 43:842-846.

62. Shin, S. H., T. Luchian, S. Cheley, O. Braha, and H. Bayley. 2002. Kinetics of a reversible covalent-bond-forming reaction observed at the single-molecule level. *Angew. Chem. Int. Ed.* 41:3707-3709.

63. Luchian, T., S. H. Shin, and H. Bayley. 2003. Single-molecule covalent chemistry with spatially separated reactants. *Angew. Chem. Int. Ed.* 42:3766-3771.

64. Luchian, T., S. H. Shin, and H. Bayley. 2003. Kinetics of a three-step reaction observed at the single-molecule level. *Angew. Chem. Int. Ed.* 42:1926-1929.

65. Shin, S. H., and H. Bayley. 2005. Stepwise growth of a single polymer chain. *J. Am. Chem. Soc.* 127:10462-10463.

66. Oukhaled, G., J. Mathe, A. L. Biance, L. Bacri, J. M. Betton, D. Lairez, J. Pelta, and L. Auvray. 2007. Unfolding of proteins and long transient conformations detected by single nanopore recording. *Phys. Rev. Lett.* 98:158101.

67. Apel, P. Y., Y. E. Korchev, Z. Siwy, R. Spohr, and M. Yoshida. 2001. Diode-like single-ion track membrane prepared by electro-stopping. *Nucl. Instrum. Methods Phys. Res., Sect. B.* 184:337-346.

68. Siwy, Z., and A. Fulinski. 2002. Fabrication of a synthetic nanopore ion-pump. *Phys. Rev. Lett.* 89:198103.

69. Siwy, Z., P. Apel, D. Baur, D. D. Dobrev, Y. E. Korchev, R. Neumann, R. Spohr, C. Trautmann, and K. Voss. 2003. Preparation of synthetic nanopores with transport properties analogous to biological channels. *Surf. Sci.* 532-535:1061-1066.

70. Harrell, C. C., S. B. Lee, and C. R. Martin. 2003. Synthetic single-nanopore and nanotube membranes. *Anal. Chem.* 75:6861-6867.

71. Harrell, C. C., Z. S. Siwy, and C. R. Martin. 2006. Conical nanopore membranes: controlling the nanopore shape. *Small.* 2:194-198.

72. Choi, Y., L. A. Baker, H. Hillebrenner, and C. R. Martin. 2006. Biosensing with conically shaped nanopores and nanotubes. *Phys. Chem. Chem. Phys.* 8:4976-4988.

73. Sun, L., and R. M. Crooks. 2000. Single carbon nanotube membranes: a well-defined model for studying mass transport through nanoporous materials. *J. Am. Chem. Soc.* 122:12340-12345.

74. Benndorf, K. 1994. Properties of single cardiac Na channels at 35 degrees C. *J. Gen. Physiol.* 104:801-820.

75. Karhanek, M., J. T. Kemp, N. Pourmand, R. W. Davis, and C. D. Webb. 2005. Single DNA molecule detection using nanopipettes and nanoparticles. *Nano Lett.* 5:403-407.

76. Wei, C., A. J. Bard, and S. W. Feldberg. 1997. Current rectification at quartz nanopipet electrodes. *Anal. Chem.* 69:4627-4633.

77. Park, S. R., H. Peng, and X. S. Ling. 2007. Fabrication of nanopores in silicon chips using feedback chemical etching. *Small.* 3:116-119.

78. Fan, R., R. Karnik, M. Yue, D. Li, A. Majumdar, and P. Yang. 2005. DNA translocation in inorganic nanotubes. *Nano Lett.* 5:1633-1637.

79. Li, J., D. Stein, C. McMullan, D. Branton, M. J. Aziz, and J. A. Golovchenko. 2001. Ion-beam sculpting at nanometre length scales. *Nature.* 412:166-169.

80. Cai, Q., B. Ledden, E. Krueger, J. A. Golovchenko, and J. Li. 2006. Nanopore Sculpting with noble gas ions. *J. Appl. Phys.* 100:024914.

81. Nilsson, J., J. R. I. Lee, T. V. Ratto, and S. E. Létant. 2006. Localized functionalization of single nanopores. *Adv. Mater. (Weinheim, Fed. Repub. Ger.).* 18:427-431.

82. Storm, A. J., J. H. Chen, X. S. Ling, H. W. Zandbergen, and C. Dekker. 2003. Fabrication of solid-state nanopores with single-nanometre precision. *Nat. Mater.* 2:537-540.

83. Chang, H., F. Kosari, G. Andreadakis, M. A. Alam, G. Vasmatzis, and R. Bashir. 2004. DNA-mediated fluctuations in ionic current through silicon oxide nanopore channels. *Nano Lett.* 4:1551-1556.

84. Heng, J. B., C. Ho., T. Kim, R. Timp, A. Aksimentiev, Y. V. Grinkova, S. Sligar, K. Schulten, and G. Timp. 2004. Sizing DNA using a nanometer-diameter pore. *Biophys. J.* 87:2905-2911.

85. Chen, P., T. Mitsui, D. B. Farmer, J. Golovchenko, R. G. Gordon, and D. Branton. 2004. Atomic layer deposition to fine-tune the surface properties and diameters of fabricated nanopores. *Nano Lett.* 4:1333-1337.

86. Wu, M. Y., D. Krapf, M. Zandbergen, H. W. Zandbergen, and P. E. Batson. 2005. Formation of nanopores in SiN/SiO2 membrane with an electron beam. *Appl. Phys. Lett.* 87:113106.

87. Kim, M. J., M. Wanunu, D. C. Bell, and A. Meller. 2006. Rapid fabrication of uniformly sized nanopores and nanopore arrays for parallel DNA analysis. *Adv. Mater.* 18:3149-3153.

88. Chang, H., S. M. Iqbal, E. A. Stach, A. H. King, N. J. Zaluzec, and R. Bashir. 2006. Fabrication and characterization of solid-state nanopores using a field emission scanning electron microscope. *Appl. Phys. Lett.* 88:103109.

89. Danelon, C., C. Santschi, J. Brugger, and H. Vogel. 2006. Fabrication and functionalization of nanochannels by electron-beam-induced silicon oxide deposition. *Langmuir.* 22:10711-10715.

90. Saleh, O. A., and L. L. Sohn. 2003. Direct detection of antibody-antigen binding using an on-chip artificial pore. *Proc. Natl. Acad. Sci. U. S. A.* 100:820-824.

91. Saleh, O. A., and L. L. Sohn. 2003. An artificial nanopore for molecular sensing. *Nano Lett.* 3:37-38.

92. Uram, J. D., K. Ke, A. J. Hunt, and M. Mayer. 2006. Label-free affinity assays by rapid detection of immune complexes in submicrometer pores. *Angew. Chem. Int. Ed.* 45:2281-2285.

93. Uram, J. D., K. Ke, A. J. Hunt, and M. Mayer. 2006. Submicrometer pore-based characterization and quantification of antibody-virus interactions. *Small.* 2:967-972.

94. Wu, S., S. R. Park, and X. S. Ling. 2006. Lithography-free formation of nanopores in plastic membranes using laser heating. *Nano Lett.* 6:2571-2576.

95. Li, J., M. Gershow, D. Stein, E. Brandin, and J. A. Golovchenko. 2003. DNA molecules and configurations in a solid state nanopore microscope. *Nat. Mater.* 2:611-615.

96. Chen, P., J. Gu, E. Brandin, Y. Kim, Q. Wang, and D. Branton. 2004. Probing single DNA molecule transport using fabricated nanopores. *Nano Lett.* 4:2293-2298.

97. Mara, A., Z. Siwy, C. Trautmann, J. Wan, and F. Kamme. 2004. An asymmetric polymer nanopore for single molecule detection. *Nano Lett.* 4:497-501.

98. Fologea, D., M. Gershow, B. Ledden, D. S. McNabb, J. A. Golovchenko, and J. Li. 2005. Detecting single stranded DNA with a solid state nanopore. *Nano Lett.* 5:1905-1909.

99. Fologea, D., J. Uplinger, B. Thomas, D. S. McNabb, and J. Li. 2005. Slowing DNA translocation in a solid-state nanopore. *Nano Lett.* 5:1734-1737.

100. Heng, J. B., A. Aksimentiev, C. Ho, P. Marks, Y. V. Grinkova, S. Sligar, K. Schulten, and G. Timp. 2005. Stretching DNA using the electric field in a synthetic nanopore. *Nano Lett.* 5:1883-1888.

101. Storm, A. J., J. H. Chen, H. W. Zandbergen, and C. Dekker. 2005. Translocation of double-strand DNA through a silicon oxide nanopore. *Phys. Rev. E.* 71:051903.

102. Storm, A. J., C. Storm, J. Chen, H. Xandbergen, J. Joanny, and C. Dekker. 2005. Fast DNA translocation through a solid-state nanopore. *Nano Lett.* 5:1193-1197.

103. Chang, H., V. B.M., S. M. Iqbal, G. Andreadakis, F. Kosari, G. Vasmatzis, P. D., and R. Bashir. 2006. DNA counterion current and saturation examined by a MEMS-based solid state nanopore sensor. *Biomed. Microdevices.* 8:263-269.

104. Harrell, C. C., Y. Choi, L. P. Horne, L. A. Baker, Z. S. Siwy, and C. R. Martin. 2006. Resistive-pulse DNA detection with a conical nanopore sensor. *Langmuir.* 22:10837-10843.

105. Heng, J. B., A. Aksimentiev, C. Ho, P. Marks, Y. V. Grinkova, S. Sligar, K. Schulten, and G. Timp. 2006. The electromechanics of DNA in a synthetic nanopore. *Biophys. J.* 90:1098-1106.

106. Smeets, R. M. M., U. F. Keyser, D. Krapf, M. Wu, N. H. Dekker, and C. Dekker. 2006. Salt dependence of ion transport and DNA translocation through solid-state nanopores. *Nano Lett.* 6:89-95.

107. Saleh, O. A., and L. L. Sohn. 2002. Correcting off-axis effects in an on-chip resistive-pulse analyzer. *Rev. Sci. Instrum.* 73:4396-4398.

108. Henriquez, R. R., T. Ito, L. Sun, and R. M. Crooks. 2004. The resurgence of Coulter counting for analyzing nanoscale objects. *Analyst.* 129:478-482.

109. Ito, T., L. Sun, M. A. Bevan, and R. M. Crooks. 2004. Comparison of nanoparticle size and electrophoretic mobility measurements using a carbon-nanotube-based Coulter counter, dynamic light scattering, transmission electron microscopy, and phase analysis light scattering. *Langmuir.* 20:6940-6945.

110. Ito, T., L. Sun, R. R. Henriquez, and R. M. Crooks. 2004. A carbon nanotube-based coulter nanoparticle counter. *Acc. Chem. Res.* 37:937-945.

111. Carbonaro, A., and L. L. Sohn. 2005. A resistive-pulse sensor chip for multianalyte immunoassays. *Lab Chip.* 5:1155-1160.

112. Lee, S., Y. Zhang, H. S. White, C. C. Harrell, and C. R. Martin. 2004. Electrophoretic capture and detection of nanoparticles at the opening of a membrane pore using scanning electrochemical microscopy. *Anal. Chem.* 76:6108-6115.

113. Heins, E. A., Z. S. Siwy, L. A. Baker, and C. R. Martin. 2005. Detecting single porphyrin molecules in a conically shaped synthetic nanopore. *Nano Lett.* 5:1824-1829.

114. Siwy, Z., L. Trofin, P. Kohli, L. A. Baker, C. Trautmann, and C. R. Martin. 2005. Protein biosensors based on biofunctionalized conical gold nanotubes. *J. Am. Chem. Soc.* 127:5000-5001.

115. Keyser, U. F., B. N. Koeleman, S. Van Dorp, D. Krapf, R. M. M. Smeets, S. G. Lemay, N. H. Dekker, and C. Dekker. 2006. Direct force measurements on DNA in a solid-state nanopore. *Nat. Phys.* 2:473-477.

116. Keyser, U. F., J. van der Does, C. Dekker, and N. H. Dekker. 2006. Optical tweezers for force measurements on DNA in nanopores. *Rev. Sci. Instrum.* 77:105105.

117. Siwy, Z. S. 2006. Ion-current rectification in nanopores and nanotubes with broken symmetry. *Adv. Funct. Mater.* 16:735-746.

118. Siwy, Z. S., E. Heins, C. C. Harrell, P. Kohli, and C. R. Martin. 2004. Conical-nanotube ion-current rectifiers: the role of surface charge. *J. Am. Chem. Soc.* 126:10850-10851.

119. Siwy, Z. S., M. R. Powell, E. Kalman, R. D. Astumian, and R. S. Eisenberg. 2006. Negative incremental resistance induced by calcium in asymmetric nanopores. *Nano Lett.* 6:473-477.

120. Siwy, Z. S., M. R. Powell, A. Petrov, E. Kalman, C. Trautmann, and R. S. Eisenberg. 2006. Calcium-induced voltage gating in single conical nanopores. *Nano Lett.* 6:1729-1734.

121. Karnik, R., C. Duan, K. Castelino, H. Daiguji, and A. Majumdar. 2007. Rectification of ionic current in a nanofluidic diode. *Nano Lett.* 7:547-551.

122. Vlassiouk, I., and Z. S. Siwy. 2007. Nanofluidic diode. *Nano Lett.* 7:552-556.

123. Harrell, C. C., P. Kohli, Z. Siwy, and C. R. Martin. 2004. DNA-nanotude artificial ion channels. *J. Am. Chem. Soc.* 126:15646-15647.

124. Keyser, U. F., D. Krapf, B. N. Koeleman, R. M. M. Smeets, N. H. Dekker, and C. Dekker. 2005. Nanopore tomography of a laser focus. *Nano Lett.* 5:2253-2256.

125. Smeets, R. M. M., U. F. Keyser, M. Y. Wu, N. H. Dekker, and C. Dekker. 2006. Nanobubbles in solid-state nanopores. *Phys. Rev. Lett.* 97:088101.

126. Siwy, Z. S., and A. Fulinski. 2003. 1/f noise in ion transport through nanopores: origins and mechanism. *AIP Conf. Proc.* 665:273-282.

127. Fertig, N., A. Tilke, R. H. Blick, J. P. Kotthaus, J. C. Behrends, and G. ten Bruggencate. 2000. Stable integration of isolated cell membrane patches in a nanomachined aperture. *Appl. Phys. Lett.* 77:1218-1220.

128. Schmidt, C., M. Mayer, and H. Vogel. 2000. A chip-based biosensor for the functional analysis of single ion channels. *Angew. Chem. Int. Ed.* 39:3137-3140.

129. Schaffer, C. B., A. Brodeur, J. F. García, and E. Mazur. 2001. Micromachining bulk glass by use of femtosecond laser pulses with nanojoule energy. *Opt. Lett.* 26:93-95.

130. Joglekar, A. P., H. Liu, G. J. Spooner, E. Meyhöfer, G. Mourou, and A. J. Hunt. 2003. A study of the deterministic character of optical damage by femtosecond laser pulses and applications to nanomachining. *Appl. Phys. B: Lasers Opt.* 77:25-30.

131. Joglekar, A. P., H. Liu, E. Meyhöfer, G. Mourou, and A. J. Hunt. 2004. Optics at critical intensity: Applications to nanomorphing. *Proc. Natl. Acad. Sci. U. S. A.* 101:5856-5861.

132. Rae, J. L., and R. A. Levis. 1992. Glass technology for patch clamp electrodes. *Methods Enzymol.* 207:66-92.

133. Ke, K., E. Hasselbrink, and A. J. Hunt. 2005. Nanofabrication with ultrafast lasers at critical intensity. *Proc. SPIE-Int. Soc. Opt. Eng.* 5714:53-62.

134. Mayer, M., J. K. Kriebel, M. T. Tosteson, and G. M. Whitesides. 2003. Microfabricated teflon membranes for low-noise recordings of ion channels in planar lipid bilayers. *Biophys. J.* 85:2684-2695.

135. Levis, R. A., and J. L. Rae. 1998. Low-noise patch-clamp techniques. *Methods Enzymol.* 293:218-266.

136. Eckhoff, R. K. 1967. Experimental indication of the volume proportional response of the Coulter counter for irregularly shaped particles. *J. Sci. Instrum.* 44:648-649.

137. http://www.niaid.nih.gov/dmid/eid/erd.htm

138. Bootz, A., V. Vogel, D. Schubert, and J. Kreuter. 2004. Comparison of scanning electron microscopy, dynamic light scattering and analytical ultracentrifugation for the sizing of poly(butylcynaoacrylate) nanoparticles. *Eur. J. Pharm. Biopharm.* 57:369-375.

139. Liu, J., P. Lester, S. Builder, and S. J. Shire. 1995. Characterization of complex formation by humanized anti-IgE monoclonal antibody and monoclonal human IgE. *Biochemistry.* 34:10474-10482.

140. Santora, L. C., Z. Kaymakcalan, P. Sakorafas, I. S. Krull, and K. Grant. 2001. Characterization of noncovalent complexes of recombinant human monoclonal

antibody and antigen using cation exchange, size exclusion chromatography and BIAcore. *Anal. Biochem.* 299:119-129.

141. Schneider, S. W., J. Lärmer, R. M. Henderson, and H. Oberleithner. 1998. Molecular weights of individual proteins correlate with molecular volumes measured by atomic force microscopy. *Pflügers Arch.* 435:362-367.

142. Guijt-van Duijn, R. M., J. Frank, G. W. K. van Dedem, and E. Baltussen. 2000. Recent advances in affinity capillary electrophoresis. *Electrophoresis (Weinheim, Fed. Repub. Ger.).* 21:3905-3918.

143. Roitt, I., J. Brostoff, and D. Male. 2001. Immunology. Mosby, Edinburgh, UK.

144. Price, C. P., and D. J. Newman, editors. 1997. Principles and Practice of Immunoassay. 2nd ed. New York, NY: Stockton Press.

145. Yang, J., M. Mayer, J. K. Kriebel, P. Garstecki, and G. M. Whitesides. 2004. Self-assembled aggregates of IgGs as templates for the growth of clusters of gold nanoparticles. *Angew. Chem. Int. Ed.* 43:1555-1558.

146. Fertig, N., C. Meyer, R. H. Blick, C. Trautmann, and J. C. Behrends. 2001. Microstructured glass chip for ion-channel electrophysiology. *Phys. Rev. E.* 64:040901.

147. Benndorf, K. 1995. Low-noise recording. *In* Single-Channel Recording. B. Sakmann and E. Neher, editors. 2nd edition, Plenum Press, New York, NY. 129-153.

148. Molleman, A. 2003. Patch Clamping: An Introductory Guide to Patch Clamp Electrophysiology. John Wiley & Sons Ltd, West Sussex, England.

149. Van Etten, J. L., and R. H. Meints. 1999. Giant viruses infecting algae. *Annu. Rev. Microbiol.* 53:447-494.

150. Parren, P. W. H. I., and D. R. Burton. 2001. The antiviral activity of antibodies *in Vitro* and *in Vivo*. *Adv. Immunol.* 77:195-262.

151. Klasse, P. J., and Q. J. Sattentau. 2002. Occupancy and mechanism in antibody-mediated neutralization of animal viruses. *J. Gen. Virol.* 83:2091-2108.

152. Van Regenmortel, M. H. V. 1988. Which value of antigenic valency should be used in antibody avidity calculations with multivalent antigens. *Mol. Immunol.* 25:565-567.

153. Pellequer, J. L., and M. H. V. Van Regenmortel. 1993. Affinity of monoclonal antibodies to large multivalent antigens: influence of steric hindrance on antibody affinity constants calculated from scatchard plots. *Mol. Immunol.* 30:955-958.

154. Dimmock, N. J., and S. A. Hardy. 2004. Valency of antibody binding to virions and its determination by surface plasmon resonance. *Rev. Med. Virol.* 14:123-135.

155. Che, Z., N. H. Olson, D. Leippe, W. Lee, A. G. Mosser, R. R. Rueckert, T. S. Baker, and T. J. Smith. 1998. Antibody-mediated neutralization of human rhinovirus 14 explored by means of cryoelectron microscopy and x-ray crystallography of Virus-Fab complexes. *J. Virol.* 72:4610-4622.

156. Stamou, D., C. Duschl, E. Delamarche, and H. Vogel. 2003. Self-assembled microarrays of attoliter molecular vessels. *Angew. Chem. Int. Ed.* 115:5738-5741.

157. Hazarika, P., B. Ceyhan, and C. M. Niemeyer. 2005. Sensitive detection of proteins using difunctional DNA-gold nanoparticles. *Small.* 1:844-848.

158. Thomas, A. A. M., T. R. Vrijsen, and A. Boeyé. 1986. Relationship between poliovirus neutralization and aggregation. *J. Virol.* 59:479-485.

159. Taylor, H. P., S. J. Armstrong, and N. J. Dimmock. 1987. Quantitative relationships between an influenza virus and neutralizing antibody. *Virology.* 159:288-298.

160. Wohlfart, C. 1988. Neutralization of adenoviruses: kinetics, stoichiometry and mechanisms. *J. Virol.* 62:2321-2328.

161. Icenogle, J., H. Shiwen, G. Duke, S. Gilbert, R. Rueckert, and J. Anderegg. 1983. Neutrilization of poliovirus by a monoclonal antibody: kinetics and stoichiometry. *Virology.* 127:412-425.

162. Taylor, H. P., and N. J. Dimmock. 1994. Competitive binding of neutalizing monoclonal and polyclonal IgG to the HA of influenza A virions in solution: only one IgG molecule is boudn per HA trimer regardles of the specificity of the competitor. *Virology.* 205:360-363.

163. Smith, T. J., N. H. Olson, R. H. Cheng, H. Liu, E. S. Chase, W. M. Lee, D. M. Leippe, A. G. Mosser, R. R. Rueckert, and T. S. Baker. 1993. Structure of human rhinovirus complexed with fab fragments from a neutralizing antibody. *J. Virol.* 67:1148-1158.

164. Flamand, A., H. Raux, Y. Gaudin, and R. W. H. Ruigrok. 1993. Mechanisms of rabies virus neutralization. *Virology.* 194:302-313.

165. Okun, V. M., R. Moser, D. Blaas, and E. Kenndler. 2001. Complexes between monoclonal antibodies and receptor fragments with a common cold virus: determination of stoichiometry by capillary electrophoresis. *Anal. Chem.* 73:3900-3906.

166. Azimzadeh, A., and M. H. V. Van Regenmortel. 1991. Measurement of affinity of viral monoclonal antibodies by ELISA titration of free antibody equilibrium mixtures. *J. Immunol. Methods.* 141:199-208.

167. Ke, K., E. F. Hasselbrink, and A. J. Hunt. 2005. Rapidly prototyped three-dimensional nanofludic channel networks in glass substrates. *Anal. Chem.* 77:5083-5088.

168. Aksimentiev, A., J. B. Heng, G. Timp, and K. Schulten. 2004. Microscopic kinetics of DNA translocations through synthetic nanopores. *Biophys. J.* 87:2086-2097.

169. Yan, H., and B. Xu. 2006. Towards rapid DNA sequencing: detecting single-stranded DNA with a solid-state nanopore. *Small.* 2:310-312.

170. Weisstein, E. W. Icosahedron. *From MathWorld--A Wolfram Web Resource. http://mathworld.wolfram.com/Icosahedron.html*.

171. Chiu, W. 1986. Electron microscopy of frozen, hydrated biological specimens. *Ann. Rev. Biophys. Biophys. Chem.* 15:237-257.

172. Baker, T. S., N. H. Olson, and S. D. Fuller. 1999. Adding the third dimension to virus life cycles: three-dimensional reconstruction of icosahedral viruses from cryo-electron micrographs. *Microbiol. Mol. Biol. Rev.* 63:862-922.

173. Wang, I., Y. Li, Q. Que, M. Bhattacharya, L. C. Lane, W. G. Chaney, and J. L. Van Etten. 1993. Evidence for virus-encoded glycosylation specificity. *Proc. Natl. Acad. Sci. U. S. A.* 90:3840-3844.

174. Nandhagopal, N., A. A. Simpson, J. R. Gurnon, X. Yan, T. S. Baker, M. V. Graves, J. L. Van Etten, and M. G. Rossmann. 2002. The structure and evolution of the major capsid protein of a large, lipid-containing DNA virus. *Proc. Natl. Acad. Sci. U. S. A.* 99:14758-11473.

175. Bashir, R. 2004. BioMEMS: state-of-the-art in detection, oppurtunities and prospects. *Adv. Drug Delivery Rev.* 56:1565-1586.

176. Sherman-Gold, R., editor. 1993. The Axon Guide: Axon Instruments, Inc.

177. Hooge, F. N. 1972. Discussion of recent experiments on 1/*f* noise. *Physica.* 60:130-144.

178. Verveen, A. A., and L. J. DeFelice. 1974. Membrane noise. *Prog. Biophys. Mol. Biol.* 28:189-265.

179. Stephens, D. B., R. E. Thomas, J. F. Stanton, and B. L. Iverson. 1998. Polyclonal antibody catalytic variability. *Biochem. J.* 332:127-134.

180. Blankenstein, G., and U. D. Larsen. 1998. Modular concept of a laboratory on a chip for chemical and biochemical analysis. *Biosens. Bioelectron.* 13:427-438.

181. Danelon, C., M. Lindemann, C. Borin, D. Fournier, and M. Winterhalter. 2004. Channel-forming membrane proteins as molecular sensors. *IEEE Trans. Nanobioscience.* 3:46-48.

182. Blake, S., T. Mayer, M. Mayer, and J. Yang. 2006. Monitoring chemical reactions by using ion channel-forming peptides. *ChemBioChem.* 7:433-435.

183. Underwood, P. A. 1993. Problems and pitfalls with measurement of antibody affinity using solid phase binding in the ELISA. *J. Immunol. Methods.* 164:119-130.

184. Saleh, O. A. 2003. A novel resistive pulse sensor for biological measurements. Princeton, NJ: Princeton University. 110 p.

185. Lauffenburger, D. A., and J. J. Linderman. 1993. Cell Surface Receptor/Ligand Binding Fundamentals. *In* Receptors. Oxford University Press, New York, NY. 9-72.

186. Hammes, G. G. 2000. Ligand binding to macromolecules. *In* Thermodynamics and kinetics for the biological sciences. John Wiley & Sons, Inc., New York, NY. 124-153.

187. Junghans, R. P. 1999. Cruel antibody fictions! Cellular antigen enumeration by 'saturation' binding. *Immunol. Today.* 20:401-406.

188. Mattes, M. J. 2005. Binding parameters of antibodies: pseudo-affinity and other misconceptions. *Cancer Immunol. Immunother.* 54:513-516.

189. Seidel, R., and C. Dekker. 2007. Single-molecule studies of nucleic acid motors. *Curr. Opin. Struct. Biol.* 17:80-86.

190. Bayley, H. 2006. Sequencing single molecules of DNA. *Curr. Opin. Chem. Biol.* 10:628-637.

191. Quist, A. P., A. Chand, S. Ramachandran, C. Daraio, S. Jin, and R. Lal. 2007. Atomic force microscopy imaging and electrical recording of lipid bilayers supported over microfabricated silicon chip nanopores: lab-on-a-chip system for lipid membranes and ion channels. *Langmuir.* 23:1375-1380.

192. Mitsui, T., D. Stein, Y. R. Kim, D. Hoogerheide, and J. A. Golovchenko. 2006. Nanoscale volcanoes: accretion of matter at ion-sculpted nanopores. *Phys. Rev. Lett.* 96:036102.

193. Kovarik, M. L., and S. C. Jacobson. 2007. Attoliter-scale dispensing in nanofluidic channels. *Anal. Chem.* 79:1655-1660.

194. Uram, J. D., and M. Mayer. 2007. Estimation of solid phase affinity constants using resistive-pulses from functionalized nanoparticles. *Biosens. Bioelectron.* 22:1556-1560.

195. Mathe, J., H. Visram, V. Viasnoff, Y. Rabin, and A. Meller. 2004. Nanopore unzipping of individual DNA hairpin molecules. *Biophys. J.* 87:3205-3212.

196. Meller, A. 2003. Dynamics of polynucleotide transport through nanometre-scale pores. *J. Phys.: Condens. Matter.* 15:R581-R607.

197. Hornblower, B., A. Coombs, R. D. Whitaker, A. Kolomeisky, S. J. Picone, A. Meller, and M. Akeson. 2007. Single-molecule analysis of DNA-protein complexes using nanopores. *Nat. Methods.* 4:315-317.

198. Kubitschek, H. E. 1960. *Research (London).* 13:128.

199. Sutherland, T. C., Y. T. Long, R. I. Stefureac, I. Bediako-Amoa, H. B. Kraatz, and J. S. Lee. 2004. Structure of peptides investigated by nanopore analysis. *Nano Lett.* 4:1273-1277.

200. Movileanu, L., S. Howorka, O. Braha, and H. Bayley. 2000. Detecting protein analytes that modulate transmembrane movement of a polymer chain within a single protein pore. *Nat. Biotechnol.* 18:1091-1095.

201. Iqbal, S. M., D. Akin, and R. Bashir. 2007. Solid-stage nanopore channels with DNA selectivity. *Nat. Nanotechnol.* 2:243-248.

202. Colquhoun, D., and F. J. Sigworth. 1995. Fitting and statistical analysis of single-channel records. *In* Single-Channel Recording. B. Sakmann and E. Neher, editors. 2nd edition, Plenum Press, New York, NY. 483-587.

203. Liu, H., S. Qian, and H. H. Bau. 2007. The effect of translocating cylindrical particles on the ionic current through a nanopore. *Biophys. J.* 92:1164-1177.

204. Levis, R. A., and J. L. Rae. 1992. Constructing a patch clamp setup. *Methods Enzymol.* 207:14-66.

205. Sigworth, F. J. 1995. Electronic design of the patch clamp. *In* Single-Channel Recording. B. Sakmann and E. Neher, editors. 2nd edition, Plenum Press, New York, NY. 95-127.

206. Benndorf, K. 1993. Multiple levels of native cardiac Na+ channels at elevated temperature measured with high-bandwidth/low-noise patch clamp. *Pflügers Arch.* 422:506-515.

207. Sigworth, F. J. 1985. Open channel noise. I. Noise in acetylcholine receptor currents suggests conformational fluctuations. *Biophys. J.* 47:709-720.

208. Wonderlin, W. F., A. Finkel, and R. J. French. 1990. Optimizing planar lipid bilayer single-channel recordings for high resolution with rapid voltage steps. *Biophys. J.* 58:289-297.

209. Burdett, R. 2005. Signals in the presence of noise. *In* Handbook of Measuring System Design. P. H. Sydenham and R. Thorn, editors. John Wiley & Sons Ltd, West Sussex, England. 827-830.

210. Hille, B. 2001. Elementary properties of pores. *In* Ion Channels of Excitable Membranes. 3rd edition, Sinauer Associates Inc, Sunderland, MA. 347-375.

211. It is possible that the *distributed* resistance of the glass pores with conical geometry, represented in the Figure 5.2A by the total resistance of the cone R_c, in series with the *distributed* capacitance of the pores, represented in Figure 5.2A as the total capacitance of the cone C_c, could limit the bandwidth of this structure below the values estimated here. We do not think, however, that the bandwidth limitation of the pore would be significant compared to the bandwidth limitation of the recording electronics (headstage, amplifier, analog low-pass filter, and digitizer) of ~ 52 kHz as discussed in the text.

212. While this relationship was derived for Gaussian filters (202), it can also be used to approximate the signal bandwidth of measurements that employ low-pass Bessel filters since a low-pass Bessel filter with a large number of poles approximates the response of a low-pass Gaussian filter (202).

213. Shapovalov, G., and H. A. Lester. 2004. Gating transitions in bacterial ion channels measured at 3 μs resolution. *J. Gen. Physiol.* 124:151-161.

214. A more complicated situation would arise if the pore had a signal bandwidth of approximately 20 – 150 kHz (i.e., a signal bandwidth that would be close to that of the HAFD). In this instance, the overall signal bandwidth of the recording would be set by the filter combination of the HAFD with the pore; a theoretical calculation of the overall signal bandwidth would be difficult to obtain. If the signal bandwidth of the pore would be less than approximately 20 kHz, then its signal bandwidth would then determine (*i.e.* limit) the overall signal bandwidth of the current recordings (assuming the signal bandwidth of the HALD would be ~52 kHz).

215. If the pore had signal bandwidth that was comparable to the signal bandwidth of the HAFD combination or the digital filter, then the exact overall signal bandwidth of the current recordings after digital filtering would be difficult to predict theoretically. In this case, the overall signal bandwidth would be smaller than the lowest signal bandwidth of the individual elements (pore, HAFD, digital filter); if

a single element would have a signal bandwidth significantly lower than the other elements (by a factor of ~3), it would determine the overall signal bandwidth of the current recordings.

216. These filters are widely used for resistive-pulse recordings since they exhibit minimal overshoot and ringing which makes them suitable for time domain analysis (176).

217. MacAvoy, T. C., and S. A. Halaby. 1964. Substrates for thin-film circuitry. *IEEE Trans. Component Parts.* 11:15-22.

218. http://www.goodfellow.com/csp/active/STATIC/A/Polyethylene_terephthalate.html

219. We point out that the noise bandwidth of the headstage and amplifier, the dielectric noise of the substrate, and the thermal noise of the pore should even be calculated by using the signal bandwidth of the HAFD combination (or the HAFD-digital filter combination) if the pore has a signal bandwidth that is comparable to or less than the signal bandwidth of the HAFD combination. We make this recommendation because the ability of the pore to limit the signal bandwidth is due to the design of patch-clamp amplifiers and not due to the pore acting like a low-pass filter (205). Since the pore does not act like a low-pass filter, additional noise but not information is included in current traces when the signal bandwidth of the amplifier is greater than the signal bandwidth of the pore (176).

220. The overall signal bandwidth of the HAFD-digital filter combination was calculated by measuring the t_{10-90} risetime of a digitally filtered square wave that was coupled in capacitively. In order to compare theory with experimental results, we subtracted the experimentally measured quantization noise from the data (since the experimental quantization noise was a factor of 16 larger than the theoretical prediction).

221. In order to demonstrate RMS noise values at highest achievable signal bandwidths (~ 52 kHz), we also included data points that were filtered only with the analog low-pass filter of the amplifier (i.e. no digital filter was used); these data points are marked with an asterisk in Fig 5.6B. We are uncertain what is causing the large amount of noise in the traces that were not filtered digitally. The "obvious" reason would be that the actual signal bandwidth was higher than what we expected; however, we determined all bandwidths in this graph experimentally from the t_{10-90} risetime. Another possibility is that the coefficients we used to calculate the noise bandwidth did not perfectly describe the filtering characteristics of the headstage-analog filter combination.

222. Although the headstage was properly shielded and grounded, we recorded a significant amount of noise in the capacitively generated square wave traces. This noise led to standard deviations (STD) of ~ 4% for the measured average 40 kHz signal bandwidth for pores fabricated in both glass and PET (individual

measurements had a STD of up to 10%). Equations 5.4 and 5.8 show that the predicted value of the noise is strongly dependent on the signal bandwidth (a large source of noise in the power spectral density of the headstage and amplifier is proportional to f^2 and the power spectral density of the dielectric noise is proportional to f). Thus small inaccuracies in determining the signal bandwidth can have a noticeable effect on the predicted values of the current noise (especially at high signal-bandwidths).

223. Horowitz, P., and W. Hill. 1989. Precision circuits and low-noise techniques. *In* The Art of Electronics. 2nd edition, Cambridge University Press, New York, NY. 391-470.

224. Sigworth, F. J., D. W. Urry, and K. U. Prasad. 1987. Open channel noise. III. High-resolution recordings show rapid current fluctuations in gramicidin A and four chemical analogues. *Biophys. J.* 52:1055-1064.

225. Heinemann, S. H., and F. J. Sigworth. 1990. Open channel noise. V. Fluctuating barriers to ion entry in gramicidin A channels. *Biophys. J.* 57:499-514.

226. Lauger, P. 1975. Shot noise in ion channels. *Biochim. Biophys. Acta.* 413:1-10.

227. Mak, D. O., and W. W. Webb. 1995. Molecular dynamics of alamethicin transmembrane channels from open-channel current noise analysis. *Biophys. J.* 69:2337-2349.

228. Robinson, F. N. H. 1974. Noise and Fluctuations in Electronic Devices and Circuits. Oxford University Press, London, England.

229. The fundamental cause of shot noise is statistical fluctuations in the current caused by the discrete and independent nature of the individual ions that make up the current (223). If the charge carriers do not act independently (i.e. if there are long-range correlations between charge carriers), then the amount of produced shot noise is far less than that predicted by the shot noise formula $I_S(f)=\sqrt{2qIf_c}$ where q is the charge of an electron and I is the DC current (223). We believe that the charge carriers in submicrometer pore and nanopore structures will not act independently when the devices do not contain a potential barrier (like the devices we examined in this report). Therefore the amount shot noise will be significantly less than predicted by the equation for $I_S(f)=\sqrt{2qIf_c}$. Since we do not currently have a model for describing this reduced amount shot noise and the majority of the extra noise appears to be of a 1/f origin as described in the text, shot noise is excluded from the extra noise discussion.

230. A majority of the power spectra examined showed trends similar to Figure 5.9, occasionally the noise initially increased linearly with decreasing frequency and then reached a plateau.

231. Hooge, F. N., and J. L. M. Gaal. 1971. Fluctuations with a 1/f spectrum in the conductance of ionic solutions and in the voltage of concentration cells. *Philips Res. Repts.* 26:77-90.

232. Shihabi, Z. K. 2006. Cryoglobulins: an important but neglected clinical test. *Ann. Clin. Lab. Sci.* 36:395-408.

233. Wintrobe, M., and M. Buell. 1933. Hyperproteinemia associated with multiple myeloma - With report of a case in which an extraordinary hyperproteinemia was associated with thrombosis of the retinal veins and symptoms suggesting Raynaud's disease. *Bulletin of the Johns Hopkins Hospital.* 52:156-165.

234. Kallemuchikkal, U., and P. D. Gorevic. 1999. Evaluation of cryoglobulins. *Arch. Pathol. Lab. Med.* 123:119-125.

235. Tang, Z., Y. Wang, K. Sun, and N. A. Kotov. 2005. Spontaneous transformation of stabilizer-depleted binary semiconductor nanoparticles into selenium and tellurium nanowires. *Adv. Mater. (Weinheim, Fed. Repub. Ger.).* 17:358-363.

236. Okun, V. M., B. Ronacher, D. Blaas, and E. Kenndler. 2000. Affinity capillary electrophoresis for the assessment of complex formation between viruses and monoclonal antibodies. *Anal. Chem.* 72:4634-4639.

237. Verdaguer, N., I. Fita, E. Domingo, and M. G. Mateu. 1997. Efficient neutralization of foot-and-mouth disease virus by monovalent antibody binding. *J. Virol.* 71:9813-9816.

238. Hewat, E. A., T. C. Marlovits, and D. Blaas. 1998. Structure of a neutralizing antibody bound monovalently to human rhinovirus 2. *J. Virol.* 72:4396-4402.

239. Lee, J., P. Hernandez, J. Lee, A. O. Govorov, and N. A. Kotov. 2007. Exciton-plasmon interactions in molecular spring assemblies of nanowires and wavelength-based protein detection. *Nat. Mater.* 6:291-295.

240. Dammacco, F., D. Sansonno, C. Piccoli, F. A. Tucci, and V. Racanelli. 2001. The cryoglobulins: an overview. *Eur. J. Clin. Invest.* 31:628-638.